



LUND UNIVERSITY

LES of Jets and Sprays Injected into Crossflow

Salewski, Mirko

2006

[Link to publication](#)

Citation for published version (APA):

Salewski, M. (2006). *LES of Jets and Sprays Injected into Crossflow*. [Doctoral Thesis (compilation), Fluid Mechanics]. Lund Institute of Technology.

Total number of authors:

1

General rights

Unless other specific re-use rights are stated the following general rights apply:

Copyright and moral rights for the publications made accessible in the public portal are retained by the authors and/or other copyright owners and it is a condition of accessing publications that users recognise and abide by the legal requirements associated with these rights.

- Users may download and print one copy of any publication from the public portal for the purpose of private study or research.
- You may not further distribute the material or use it for any profit-making activity or commercial gain
- You may freely distribute the URL identifying the publication in the public portal

Read more about Creative commons licenses: <https://creativecommons.org/licenses/>

Take down policy

If you believe that this document breaches copyright please contact us providing details, and we will remove access to the work immediately and investigate your claim.

LUND UNIVERSITY

PO Box 117
221 00 Lund
+46 46-222 00 00

LES of Jets and Sprays Injected into Crossflow

Mirko Salewski

November, 2006

Thesis for the degree of Doctor of Philosophy
ISBN-13 978-91-628-6967-0
ISBN-10 91-628-6967-1
ISSN 0282-1990
ISRN LUTMDN/TMHP-06/1046-SE

©Mirko Salewski, November 2006
Division of Fluid Mechanics
Department of Energy Sciences
Lund Institute of Technology
Box 118
S-221 00 LUND
Sweden

Typeset in L^AT_EX
Printed by Media-Tryck, Lund, November 2006

Abstract

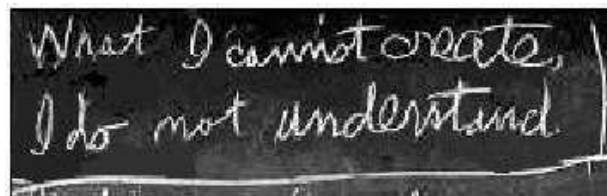
The objective of this thesis is to numerically simulate a fluid jet injected into a crossflow of the same or another fluid, respectively. Such flows are encountered in many engineering applications in which cooling or mixing plays an important role, e.g. gas turbine combustors. The jet in crossflow (JICF) is used both for cooling and for injecting liquid fuel into the air stream prior to combustion. The numerical simulations regard three space dimensions and track also the flow dynamics by integrating the governing equations in time. The spatial and the temporal resolution are such that the large-scale flow structures are resolved. Such an approach is referred to as large eddy simulations (LES). The motion of the fuel droplets is treated by Lagrangian particle tracking (LPT) with the stochastic parcel method, along with submodels for evaporation, collision, breakup, and a novel submodel for aerodynamic four-way coupling: The particle drag is corrected depending on relative positions of the particles. Mixture fraction and temperature transport equations are solved to enable the modeling of droplet evaporation and the mixing of the gaseous fuel with ambient air.

In the simulations of multiphase JICF, several computed results are shown to be inconsistent with the underlying assumptions of the LPT approach: The magnitude of the Weber numbers indicates that droplets are not spherical in large portions of the flow field in wide ranges of parameters which are relevant for gas turbine operation. The magnitude of the droplet spacing suggests that aerodynamic interaction (indirect four-way coupling) among droplets may be important. The LES with aerodynamic four-way coupling reveals significant effects compared to two-way coupling for monodisperse particles in a dense multiphase flow.

For single-phase JICF, the impact of nozzle shape on the large-scale coherent structures and the mixing is studied. Effects of circular, square, and elliptic nozzles and their orientation are considered. It is demonstrated that square and elliptic nozzles with blunt orientation raise turbulence levels significantly. The scalar distribution in a cross-sectional plane is found to be single-peaked for these nozzles whereas circular and the nozzles with pointed

orientation show double-peaked scalar distribution. It is the nozzles with a single-peaked distribution which are the better mixers.

The differences and similarities of single- and multiphase JICF are compared, and it is demonstrated that the flow field solution for multiphase flow approaches the flow field solution of single-phase flow in the limit of small Stokes numbers.



R.P. Feynman's blackboard at the time of his death (Caltech archives)

Acknowledgments

This work was carried out at the Division of Fluid Mechanics, Lund University/Lund Institute of Technology, Sweden. The work was financially supported by the Swedish Energy Agency (STEM), the Swedish Research Council (VR), and the Centre for Combustion Science and Technology (CE-COST). Computational resources were provided by the Center for Scientific and Technical Computing at Lund University (LUNARC) and by HPC2N facilities.

I would like to thank my supervisor Laszlo Fuchs for being an inexhaustible source of many more interesting ideas than I could possibly evaluate and my co-supervisor Xue-Song Bai for his clarity and patience in our countless discussions. I thank Christophe Duwig for his many valuable suggestions in any field of my thesis, Dragan Stankovic for his help as co-author of several papers, Robert-Zoltan Szasz for never failing to pep talk my computer, Johan Revstedt for the training in our basic kung fu during the teaching assignments, and Karl-Johan Nogenmyr and Lisa Prahl for cross-reading the manuscript.

Contents

Nomenclature	xiii
1 Introduction	1
1.1 Context and Motivation	1
1.2 Research Objectives and Contents	4
1.3 Main Contributions	5
1.3.1 Multiphase Jets in Crossflow	5
1.3.2 Single-Phase Jets in Crossflow	6
2 Turbulence and Its Modeling	7
2.1 Characteristics of Turbulence	7
2.2 Statistical Tools Relevant to Turbulence	8
2.2.1 Averages	8
2.2.2 Reynolds and Favre Decomposition	10
2.2.3 Root Mean Square	11
2.2.4 Probability Density Function	11
2.2.5 Fourier Decomposition	12
2.2.6 Proper Orthogonal Decomposition	13
2.3 Turbulence Scales	16
2.4 Turbulence Modeling	19
2.4.1 Direct Numerical Simulation	20
2.4.2 Reynolds-Averaged Navier-Stokes Equations	20
2.4.3 Large Eddy Simulation	22
3 Jets in Crossflow	25
3.1 Characteristic Parameters	27
3.2 Jet Deflection Mechanisms	28
3.3 Coherent Structures	29
3.3.1 Counter-Rotating Vortex Pair	29
3.3.2 Horseshoe Vortices	31
3.3.3 Jet Shear Layer Vortices	32

3.3.4	Wake Vortices	32
3.4	Non-Circular Jets in Crossflow	33
3.5	Spray Jets in Crossflow	34
3.5.1	Breakup of Liquid Jets	36
3.5.2	Breakup of Liquid Jets in Crossflow	39
4	Multiphase Flows with a Dispersed Phase	41
4.1	Governing Equations for Two-phase Flows	43
4.1.1	Euler/Euler	44
4.1.2	Euler/Lagrange	44
4.2	Lagrangian Particle Tracking	48
4.2.1	Stochastic Parcel Method	48
4.2.2	Particle Trajectories	48
4.2.3	Forces on a Particle	50
4.2.4	Droplet Evaporation	53
4.2.5	Droplet Breakup	54
4.2.6	Droplet Collision	58
4.3	Parameter Sensitivity Regarding JICF	59
4.3.1	Initial Droplet Size and Its Distribution	60
4.3.2	Injection Droplet Velocity Fluctuation	64
4.3.3	Flow Reynolds Number	64
4.3.4	Number of Parcels	64
5	Numerical Methods	67
5.1	Computational Fluid Dynamics	67
5.2	Discretization	68
5.2.1	Upwind Schemes	68
5.2.2	Weighted Essentially Non-Oscillatory Schemes	69
5.2.3	Compact and Optimized Schemes	72
5.2.4	Comparison of the Schemes	74
5.2.5	Boundary Scheme	85
5.3	Flow Solver	85
6	Summary of Publications	87
7	Summary and Perspectives	91

List of Figures

1.1	Current and projected worldwide energy sources, thick line: Total energy in gigatons of oil equivalent (GTOE), thin lines: fractions	2
2.1	Variable in a turbulent flow field	9
2.2	Energy spectrum in a turbulent flow	17
2.3	Autocorrelation coefficient over the distance	17
3.1	Coherent Structures JICF flow fields (adapted from Fric and Roshko (1994))	26
3.2	Breakup regimes of a liquid jet in quiescent atmosphere	36
3.3	Liquid column breakup of a spray JICF (after Wu et al. (1997))	39
4.1	Particle spacing	42
4.2	Droplet breakup regimes (after Tanner (2004))	55
4.3	Droplet distortion (after Bergström (1999))	57
4.4	Droplet collision regimes (after Bergström (1999))	59
4.5	Channel geometry	60
4.6	Spray and gas parameters	60
4.7	v and w velocity and liquid volume fraction profiles for various droplet injection diameters and solid particle diameters 100 diameters downstream	62
4.8	Droplet size distributions at various heights 25 diameters down- stream for various injection Sauter mean diameters	63
4.9	Droplet size distributions at various heights 25 diameters down- stream for various droplet injection velocity fluctuations	65
4.10	Average profiles along vertical centerline for various flow Rey- nolds numbers (5000-50000) 25 diameters downstream	65
4.11	Volume fraction profiles for various average parcel numbers at $z/D = 25$ in the centerplane	66

4.12	Droplet size distributions for various average parcel numbers at $z/D = 25$ in the centerplane	66
5.1	Computational cell in a 3D staggered grid	69
5.2	Propagation of a step	75
5.3	Propagation of a sine^2 wave with upwind schemes	76
5.4	Propagation of a sine^2 wave with central schemes	77
5.5	Dispersion error	78
5.6	Dissipation error	79
5.7	Comparison of accuracy for momentum equations for high- order schemes	80
5.8	Comparison of accuracy for momentum equations for central schemes, upwinded central schemes, and central schemes with explicit filtering	81
5.9	Required time per time step in seconds for various discretiza- tion schemes on three grids	82
5.10	Average and rms of vertical velocity profiles along vertical cen- terline 100 diameters downstream	83
5.11	Profiles for vertical and streamwise velocities	85

Nomenclature

Latin Characters

a	acceleration, [m/s^2]
a	speed of sound, [m/s]
C_d	drag coefficient, [-]
D	molecular diffusivity, [m^2/s]
D	droplet/particle diameter, [m]
E	turbulent kinetic energy per unit wavenumber and mass, [m^3/s^2]
F	filter function, [-]
F	cumulative distribution function [-]
F	force, [N]
f	probability density function
f	particle number, [-]
g	acceleration due to gravity, [m/s^2]
h	specific enthalpy, [m^2/s^2]
h	cell size, [m]
k	turbulent kinetic energy per unit mass, [m^2/s^2]
k	wavenumber, [$1/m$]
L	length scale, [m]
l_0	integral length scale, [m]
M	molar mass, [$kg/kmol$]
m	mass, [kg]
N	number of samples, [-]
P	production of turbulent kinetic energy per unit mass, [m^2/s^3]
p	pressure, [N/m^2]
Q	heat flux, [$J/(sm^2)$]
R	vortex spacing, [m]
R_{uu}	autocorrelation coefficient, [-]
R	autocorrelation tensor
r	radius, [m]
T	temperature, [K]
T	averaging time, [s]
t	time, [s]

t_0	integral time scale, [s]
t_λ	Taylor time scale, [s]
t_η	Kolmogorov time scale, [s]
U	velocity scale, [m/s]
U	random variable
u	flow velocity, [m/s]
u'_0	integral velocity scale, [m/s]
V	sample-space variable
v	particle velocity, [m/s]
x	space coordinate, [m]
Y	mass fraction, [-]
y	distortion parameter, [m]
y	jet penetration, [m]
Z	mixture fraction, [-]

Greek Characters

α	heat diffusivity, [m ² /s]
β	smoothness indicator, [-]
γ	linear weight, [-]
δ	Kronecker delta, [-]
δ	scalar, [-]
ϵ	dissipation rate of turbulent kinetic energy per unit mass, [m ² /s ³]
η	Kolmogorov length scale, [m]
θ	volume fraction, [-]
λ	Taylor length scale, [m]
λ	POD eigenvalue
μ	dynamic viscosity, [kg/(m·s)]
μ_n	n^{th} central moment of the PDF
ν	kinematic viscosity, [m ² /s]
ν_t	eddy viscosity, [m ² /s]
ϕ	arbitrary variable, [-]
ϕ	POD eigenmode, [-]
ψ	arbitrary basis function, [-]
ρ	density, [kg/m ³]
σ	surface tension, [N/m]
τ	time scale, [s]
τ_{ij}	turbulent stress tensor, [m ² /s ²]
ω	vorticity, [1/s]
ω	nonlinear weight, [-]
ω	arbitrary function, [-]

Non-dimensional Numbers

$$B_d = \frac{Y_F^s - Y_F^\infty}{1 - Y_F^s} \quad \text{Mass transfer number}$$

$$C = \frac{U\Delta t}{h} \quad \text{Courant number}$$

$$Fr = \frac{U^2}{gD} \quad \text{Froude number}$$

$$J = \frac{\rho_{jet} U_{jet}^2}{\rho_\infty U_\infty^2} \quad \text{Momentum flux ratio}$$

$$Ma = \frac{u}{a} \quad \text{Mach number}$$

$$Nu = -\frac{D}{T_s - T_\infty} \left(\frac{dT}{dr} \right)_s \quad \text{Nusselt number}$$

$$Oh = \frac{\mu}{(\rho\sigma D)^{1/2}} \quad \text{Ohnesorge number}$$

$$Pr = \frac{\nu}{\alpha} \quad \text{Prandtl number}$$

$$Pe = \frac{uh}{\nu} \quad \text{Péclet number}$$

$$R = \frac{U_{jet}}{U_\infty} \quad \text{Velocity ratio}$$

$$R_e = \sqrt{\frac{\rho_{jet} U_{jet}^2}{\rho_\infty U_\infty^2}} \quad \text{Effective velocity ratio}$$

$$Re = \frac{UL}{\nu} \quad \text{Reynolds number}$$

$$S = \frac{U_{tangential}}{U_{axial}} \quad \text{Swirl number}$$

$$Sc = \frac{\nu}{D} \quad \text{Schmidt number}$$

$$Sh = -\frac{D}{Y_F^s - Y_F^\infty} \left(\frac{dY_F}{dr} \right)_s \quad \text{Sherwood number}$$

$$St = \frac{\tau_v}{\tau_f} \quad \text{Stokes number}$$

$$St = \frac{fD}{U} \quad \text{Strouhal number}$$

$$We = \frac{\rho DU^2}{\sigma} \quad \text{Weber number}$$

Abbreviations

<i>BBO</i>	Basset-Boussinesq-Oseen
<i>CDF</i>	Cumulative Distribution Function
<i>CFD</i>	Computational Fluid Dynamics
<i>CVP</i>	Counter-rotating Vortex Pair
<i>DNS</i>	Direct Numerical Simulation
<i>ENO</i>	Essentially Non-Oscillatory
<i>FDE</i>	Finite Difference Equation
<i>GTOE</i>	Giga Tons of Oil Equivalent
<i>JICF</i>	Jet In Crossflow
<i>LES</i>	Large Eddy Simulation
<i>LIF</i>	Laser-Induced Fluorescence
<i>LP</i>	Lean Premixed
<i>LPP</i>	Lean Premixed Prevaporized
<i>PDA</i>	Phase-Doppler Anemometry
<i>PDE</i>	Partial Differential Equation
<i>PDF</i>	Probability Density Function
<i>PIV</i>	Particle Image Velocimetry
<i>POD</i>	Proper Orthogonal Decomposition
<i>RANS</i>	Reynolds-Averaged Navier-Stokes
<i>RSM</i>	Reynolds Stress Model
<i>RMS</i>	Root Mean Square
<i>RQL</i>	Rich-burn, Quick-quench, Lean-burn
<i>SGS</i>	Subgrid Scale
<i>SMD</i>	Sauter Mean Diameter
<i>SMR</i>	Sauter Mean Radius
<i>TAB</i>	Taylor Analogy Breakup
<i>TVD</i>	Total Variation Diminishing
<i>URANS</i>	Unsteady Reynolds-Averaged Navier-Stokes
<i>WENO</i>	Weighted Essentially Non-Oscillatory
<i>ppm</i>	parts per million

Chapter 1

Introduction

1.1 Context and Motivation

It is estimated that the worldwide demand for total primary energy supply will be satisfied with an energy cocktail containing a large share of combustible fuels in the next many years to come. The percentage of combustible fuels is projected to lie well beyond 80% in the next 25 years. Fig.1.1 shows a forecast of primary energy sources and a comparison to present and past records (IEA, 2004). It is predicted that the worldwide energy demand will increase in the future (thick line). The thin lines divide the total energy into the contributions of various primary energy sources, such that the area of each region is proportional to the fraction. Oil is estimated to account for roughly one third of the energy sources in the future, coal and natural gas for one quarter to one fifth each, combustible renewable sources for one tenth or less. Non-combustible renewable energy sources as wind energy, water energy, or solar energy are not likely to make significant contributions to the worldwide energy budget and are lumped with combustible renewables in Fig.1.1. Despite a tendency to turn to natural gas, the energy mix is judged not to change substantially during this period. Presently, exploitation of nuclear fission is unpopular, but has the potential to be a leading energy source. Nuclear fusion has not been demonstrated yet to be controllable to maintain a positive energy balance under power plant conditions. Even though a demonstration plant has recently been planned to be built, nuclear fusion surely cannot be regarded as major energy source within this time frame.

A major energy conversion system for combustible fuel sources are gas turbines. These are applied in stationary power plants and in airborne systems. The design of gas turbines is governed by the goal to obtain as much

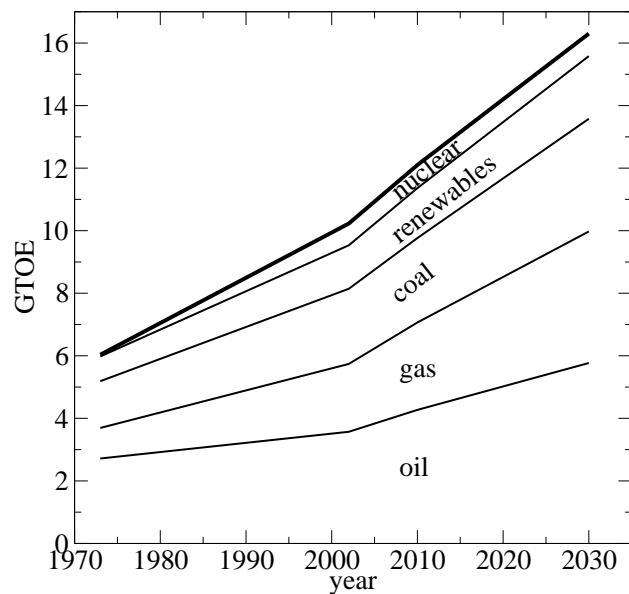


Figure 1.1: Current and projected worldwide energy sources, thick line: Total energy in gigatons of oil equivalent (GTOE), thin lines: fractions

power per unit fuel consumption rate as possible, i.e. a high thermodynamic efficiency, especially in view of the declining fuel reservoirs and potentially climbing prices. High efficiency is not only important from economic viewpoint but also from ecological point of view as the total mass of exhaust products is inversely proportional to the cycle efficiency. Carbon dioxide and water vapor, the most abundant combustion products, are thought to contribute to global warming by the greenhouse effect, the trapping of infrared radiation. It has been estimated that the presence of these two gases ($\sim 1\%$ in air) raises the temperature of the earth by 33°C (Atkins and Jones, 2005), i.e. were they not there, it would be colder. Water vapor levels do not change dramatically due to the presence of oceans, but raising carbon dioxide levels will increase the temperature of the earth. Paradoxically, they are the desired emission products from the standpoint of combustion efficiency.

The cycle efficiency of gas turbines can be increased by elevating the combustor inlet pressures and temperatures. Unfortunately, the formation rates of NO_x accelerate strongly with pressure and especially temperature due to the thermal NO_x formation mechanism. Reducing NO_x is a pivotal issue during the design of new gas turbines, as NO_x is toxic, leads to photochemical smog, acid rain, and depletion of the ozone layer (Atkins and Jones, 2005). The key for reducing NO_x lies in the combustion mode: Premixed flames are preferable to diffusion flames as they offer the opportunity

to choose the equivalence ratio in reaction zones well below or above stoichiometric conditions and thereby reduce local temperatures and NO_x formation rates. A combustor operating in rich premixed combustion mode alone, however, is easy to reject: Fuel has to be purchased whereas air is cost free and not even taxed. Additionally, products of oxygen-deprived combustion are harmful to the environment, e.g. carbon monoxide is highly toxic, several unburned hydrocarbons are toxic and contribute to photochemical smog, and soot is visible as smoke and accumulates in the worst case to pea-soup smog with its potential health hazards (Glassman, 1996). It follows for practical purposes that the overall mixture ratio has to be lean. This has led to the development of combustors operating with lean premixed (LP) flames.

If liquid fuel is used in LP mode, it has obviously to be vaporized before it can be premixed. The LP low- NO_x concept with liquid fuel is called lean premixed prevaporized (LPP) combustion. Whereas NO_x emissions for gas turbines operating with gaseous fuel are down to single-digit ppm levels, the emissions are significantly higher if liquid fuels are used (Lefebvre, 1995). This is due to local intermittent non-mixedness which leads to hot spots with excessive production of thermal NO_x . Fuel injection systems for LPP gas turbine combustors are therefore required to steadily provide a mixture of fuel and air with a specified equivalence ratio profile.

The spray jet in crossflow (JICF) is advantageous as fuel preparation system since atomization offers the opportunity to disintegrate the liquid fuel jet to fine droplets, which evaporate fast, while the momentum ratio, the injection angle, or swirl can be used to tailor various equivalence ratio profiles. Atomization is not well understood, and hence one needs to study a wide range of conditions.

Also the generic flow of a single-phase JICF plays a key role in gas turbines (Lefebvre, 1995). The hot combustion gases are mixed with dilution air to shape the temperature profile and reduce the heat transfer to the turbine blades to acceptable levels, especially for gas turbines operating in diffusion flame mode. For this purpose air jets are injected through the dilution holes, forming JICF. Secondly, also gaseous fuel may be injected into a crossflow. This may be an important point as gas turbines are designed to have flexible-fuel capacity. This wide range of applications of the JICF in gas turbines justifies and motivates detailed study of this generic flow field. Further, single- and multiphase JICF have comparable coherent structures, and one may infer knowledge from single-phase JICF to multiphase JICF.

1.2 Research Objectives and Contents

Many publications dealing with single-phase JICF have increased the understanding of this flow. This large amount work was partly motivated by the need to understand JICF for mixing and cooling applications as described above. There is also extensive literature regarding multiphase JICF, and these are mostly motivated by applications related to fuel spray injection. This thesis seeks to apply computational techniques to study single- and multiphase JICF for gas turbine application, i.e. fuel/air preparation for LPP burners. Through survey of the relevant literature, the following questions emerged to be answerable with the tools advocated in this thesis:

- What is the effect of the nozzle shape for the development of coherent structures and small-scale turbulence?
- How important is the nozzle shape for the global mixing performance?
- Why can there be a qualitative difference in the distribution of a passive scalar for various nozzle shapes?
- How large are the effects of nozzle geometry and swirl for multiphase flow?
- Where in the flow field are the model premises of the multiphase flow computation violated?
- What is the global effect of a model to account for aerodynamic particle-particle interaction / 4-way coupling?
- How does the flow field of a single-phase JICF compare to the flow field of a multiphase JICF and what is the effect of the Stokes number?

The ultimate goal is to improve models to enable one to make more accurate predictions of fuel injection systems in combustion devices. This thesis makes its modest contribution in this direction.

The main text body discusses the most relevant phenomena and methods to investigate them in more detail than is possible in publications. The most relevant physical features of turbulent flows, and methods of their description and modeling, are discussed in Ch.2. It is argued that LES is an appropriate turbulence model for the flows investigated in this thesis. Literature reviews of single-phase and spray JICF are given in Ch.3. This chapter is intended as a summary of related work and physical phenomena which this thesis attempts to model. The review for the single-phase case includes mechanisms for jet bending and the formation and transport of the coherent structures present in the flow field: The counter-rotating vortex pair (CVP), horseshoe vortices, wake vortices, and jet shear layer vortices. For the two-phase flow case, additional complicating issues are the breakup of the liquid jet and the

dense dispersed flow in the near-field. Ch.4 focuses on modeling two-phase flows with a dispersed phase. Lagrangian particle tracking (LPT) and the stochastic parcel method are chosen for modeling the spray motion. Atomization and droplet breakup are modeled by the wave breakup model or the Taylor analogy breakup (TAB) model. Submodels for evaporation, collision, and a novel submodel for aerodynamic four-way coupling are discussed. The mixture fraction transport equation is solved to study the mixing of evaporated fuel and air. Ch.5 contains a comparison of high-order discretization schemes in terms of formal accuracy, computational efficiency, and dispersion and dissipation errors: Third-order upwind schemes, a fifth-order so-called WENO scheme, and a second-order so-called optimized scheme. The schemes are applied in an LES computation of a spray JICF. The WENO scheme is seen fit for the given case.

1.3 Main Contributions

The main contributions of the thesis are several answers to the questions posed in Sec.1.2. These are summarized in the following sections.

1.3.1 Multiphase Jets in Crossflow

Consistency Issues

Maps for average Weber numbers, Stokes numbers, and the average droplet spacing are advanced to reveal the inadequacy of several model premises of LPT. In LPT, droplets are usually assumed to be spherical and isolated. These assumptions are demonstrated to be inconsistent with the computed Weber numbers, which suggest droplet distortion, and the computed droplet spacing, which suggests that the effects of passers-by droplets may be significant (indirect or aerodynamic four-way coupling).

Modeling of Aerodynamic Droplet Interaction

A novel model is proposed to account for aerodynamic four-way coupling in an LES with monodisperse particles: Correction factors for the particle drag coefficients are computed depending on relative positions of the particles. The penetration of the particles and the turbulence levels are shown to change significantly if four-way interaction is accounted for.

LES of Sprays

The LES/LPT technique is validated by computing the numerical accuracy, the sensitivity to various modeling parameters, and a comparison to experimental data.

Comparison Single- and Multiphase JICF

Multiphase JICF can be compared to single-phase JICF: One can identify corresponding coherent structures in the continuous phase. For small Stokes numbers the solution for multiphase flow approaches the solution for single-phase flow.

1.3.2 Single-Phase Jets in Crossflow

Nozzle Shape Effects

Turbulence statistics in this flow field are compared for circular, square, diamond-shaped, and elliptic nozzles with high and low aspect ratios. The results suggest that the distribution of a passive scalar in a cross-sectional plane can have qualitative differences: It can be single- or double-peaked, depending on the nozzle shape and orientation. Differences in large-scale coherent structures may be responsible for this phenomenon. The results indicate that nozzles with a single-peaked distribution have superior mixing performance.

Counter-Gradient Transport

It is demonstrated that the flow field contains large regions in which a passive scalar is transported up the mean gradient (counter-gradient transport) which implies failure of the eddy viscosity hypothesis.

Handling of Subgrid Structures

The nozzle geometry of the jet is handled as a subgrid structure, and hence the boundary conditions are handled consistently by applying a filter to them. The LES are validated against the experimental results obtained by particle image velocimetry (PIV) and laser-induced fluorescence (LIF) in a parallel in-house study and data previously published in the literature. The sensitivity of the computed results to numerical, modeling, and physical parameters is presented.

Chapter 2

Turbulence and Its Modeling

Flows can be divided into three regimes: Laminar, transitional, and turbulent. In *laminar* flows the fluid moves orderly in layers. *Turbulent* flows, on the other hand, are characterized by seemingly random motion. The regime can change from laminar to turbulent if the flow is unstable. If the instability leads to turbulent flow, the regime in which the change occurs is referred to as *transition*. Practically all flows relevant to engineering applications are turbulent. Compared to laminar flows, turbulence enhances heat-, mass-, and momentum transfer. Increased drag or pressure loss are examples for situations in which turbulence is disadvantageous; increased cooling, increased mixing, or decreased drag, however, make turbulence beneficial in other situations. The most significant parameter to characterize flow regimes is the Reynolds number Re :

$$Re = \frac{UL}{\nu} \tag{2.1}$$

U and L are characteristic velocity and length scales of the flow, and ν is the kinematic viscosity of the fluid. The Reynolds number is a non-dimensional parameter representing the ratio of convective and diffusive transport. Low Reynolds number flows are laminar, high Reynolds number flows are turbulent, and transition occurs over a range of Reynolds numbers typical for the particular flow.

2.1 Characteristics of Turbulence

In lieu of a precise definition of turbulence, the characteristics of turbulence are summarized by Tennekes and Lumley (1972):

- *Random.* Flow quantities fluctuate in space and time in a chaotic or apparently random manner.
- *High Reynolds number.* Convection is much faster than diffusion. High Reynolds number flows possess a *wide range of scales* as is shown in Sec.2.3.
- *Dissipative.* Kinetic energy is converted to heat at the smallest scales.
- *Continuum.* The continuum hypothesis demands a scale separation: The smallest flow scales are much larger than the molecular scales.
- *Three-dimensional.* Three dimensions are necessary for vortex stretching.
- *Diffusive.* Turbulence enhances mass-, momentum-, and heat transfer.
- *Turbulence is a property of the flow, not the fluid.*

2.2 Statistical Tools Relevant to Turbulence

Popper (1934) demands that scientific data must always be falsifiable and therefore must obviously be reproducible. As variables in turbulent flows fluctuate unpredictably, instantaneous data on turbulent flows is irreproducible and therefore unscientific. The statistical properties of turbulent flow, however, converge to unique values which depend on problem conditions only, and these statistical quantities are reproducible. If the flow is statistically steady, these values are also independent of initial state (disregarding the possibilities of multiple solutions and hysteresis). Thus a statistical description of turbulence offers the only solution for obtaining meaningful, reproducible, i.e. scientific, data that can characterize the particular flow. Among the many statistical quantities that can be defined, in this thesis averages, root mean squares (i.e. the rms of the fluctuations), probability density functions, and the proper orthogonal decomposition are computed. These tools are discussed in the following sections.

2.2.1 Averages

Depending on the situation different types of averages can be applied. Averages are commonly not defined operationally but axiomatic since population averages cannot be measured but they can be estimated along with a confidence level (Pope, 2000). One can take averages *a priori* and apply averaging operators to the governing equations before their solution, or *a posteriori* as in experiments or direct solution of the Navier-Stokes equations. *A posteriori* averages are random variables themselves as it is not likely to obtain the same average with a new (finite) set of samples. According to the central

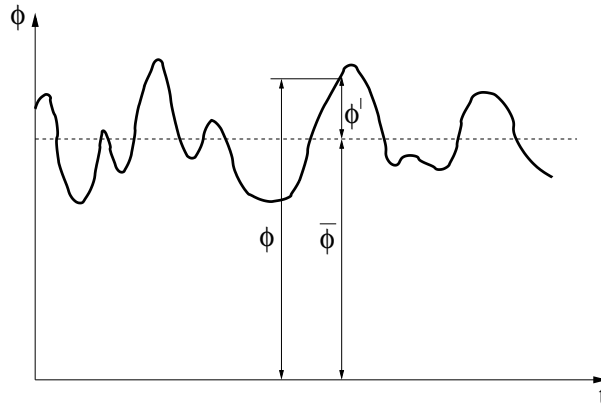


Figure 2.1: Variable in a turbulent flow field

limit theorem the sample averages will have a Gaussian distribution whose mean is the population mean. Any *a posteriori* sample average is therefore an approximation of the population average, and the difference is called a statistical error (see Sec.5.1). The most common averaging techniques are ensemble-, space-, time-, and phase-averages, and combinations of these. These averaging techniques are briefly discussed below.

Time-Average

Time-averaging is applied *a posteriori* on the gathered data in experiments, e.g. particle image velocimetry (PIV), and in detailed numerical simulations such as DNS (Sec.2.4.1) and LES (Sec.2.4.3), or *a priori* on the dependent variables and the governing equations in the RANS equations turbulence modeling approach (Sec.2.4.2). Experimental data may inherently be partially averaged in time *a priori* due to the finite temporal resolution of the apparatus. If ϕ is a random variable and T is the averaging time, then the time average is defined by:

$$\bar{\phi} = \lim_{T \rightarrow \infty} \frac{1}{T} \int_T \phi dt \quad (2.2)$$

Space-Average

Space-averages and filtering address the question of resolution of the applied technique. Experimental data may inherently be space-averaged due to the finite spatial resolution of the equipment, e.g. the interrogation region size in PIV or the wire diameter in temperature measurements with thermocouples.

Further applications of space-averaging are LES (Sec.2.4.3) and the modeling of multiphase flows (Sec.4.1.1). If V is the averaging volume, then the volume average $\tilde{\phi}$ is defined by:

$$\tilde{\phi} = \frac{1}{V} \int_V \phi \, dV \quad (2.3)$$

Ensemble-Average

Ensemble-averaging is applied if data from a finite number of samples has to be averaged. This is the case if N experiments are conducted and their results are averaged. It is also used instead of time-averaging which is according to the ergodic hypothesis a valid replacement. The ensemble average of N samples is:

$$\langle \phi \rangle = \frac{1}{N} \sum_{n=1}^N \phi_n \quad (2.4)$$

Phase-Average

Phase-averaging is practical to assess periodic processes statistically, e.g. flow in reciprocating engines or long-term weather data. $\Delta\tau$ is a characteristic time scale of the problem, e.g. one cycle in an engine, one rotation of the earth or one revolution around the sun.

$$\hat{\phi} = \frac{1}{N} \sum_{n=1}^N \phi_n(n\Delta\tau) \quad (2.5)$$

2.2.2 Reynolds and Favre Decomposition

Instantaneous flow variables can be decomposed into average and fluctuating parts as shown in Fig. 2.1. Two kinds of decomposition have wide application in numerical simulation of turbulent flows: Reynolds- and Favre-averaging. In Reynolds-averaging, flow variables are averaged, and instantaneous variables are decomposed as:

$$\phi = \bar{\phi} + \phi' \quad (2.6)$$

If Reynolds-averaging is applied to the continuity equation, additional terms appear in the averaged equation, the correlations between the fluctuating density and the fluctuating velocities. If the flow is incompressible, these

correlations are identically zero, and Reynolds-averaging is convenient. However, for flows with varying density the unclosed terms remain if Reynolds-averaging is used. They can be avoided if instead density-weighted variables are averaged. The density-weighted or Favre-average is defined as:

$$\tilde{\phi} = \frac{\overline{\rho\phi}}{\bar{\rho}} \quad (2.7)$$

The decomposition is then:

$$\phi = \tilde{\phi} + \phi'' \quad (2.8)$$

2.2.3 Root Mean Square

Averages alone give no information about the spread in the data. A common way to characterize the fluctuation is the the root mean square (RMS), here written for ensemble-averages:

$$\phi_{rms} = \sqrt{\frac{1}{N} \sum_{n=1}^N (\phi_n - \langle \phi \rangle)^2} \quad (2.9)$$

2.2.4 Probability Density Function

Probability density functions (PDF) give more detailed descriptions of random events than averages and RMS. (Pope, 2000). The PDF is the derivative of the cumulative distribution function (CDF). If U is a random variable in the sample space and V is an independent sample space variable, then the CDF, $F(V)$, is the probability P that the sampled variable U is smaller than V :

$$F(V) = P(U < V) \quad (2.10)$$

The CDF varies from probability 0 at $V \rightarrow -\infty$ to probability 1 at $V \rightarrow \infty$. The PDF, $f(V)$, is the derivative with respect to V :

$$f(V) = \frac{dF(V)}{dV} \quad (2.11)$$

Since the integral of the PDF is a probability, the ordinate must be a probability per unit of the abscissa, i.e. per unit sampled variable, and this is called probability density. This also means that the PDF cannot be negative and the improper integral is unity. The average and RMS can be linked to the PDF. The average is the integral of the variable-weighted PDF:

$$\bar{U} = \int_{-\infty}^{\infty} V f(V) dV \quad (2.12)$$

The n^{th} central moment is defined as:

$$\mu_n = \int_{-\infty}^{\infty} (V - \bar{U})^n f(V) dV \quad (2.13)$$

The square root of the second central moment can be identified as RMS. The third and fourth central moment are called skewness and flatness, respectively.

2.2.5 Fourier Decomposition

Fourier decomposition is a method to extract frequencies from a set of time-resolved data. It is, like the proper orthogonal decomposition, an expansion in orthogonal base functions. For the Fourier decomposition these orthogonal base functions are sine and cosine functions which can be conveniently represented by the exponential function with imaginary exponent ($e^{i\omega t} = \cos \omega t + i \sin \omega t$). Two functions f_1 and f_2 are orthogonal if their inner product disappears: $\int f_1 f_2 dt = 0$. Suppose $f(t)$ is periodic in T , then one can write $f(t)$ as (Feynman, Leighton, and Sands, 1963)

$$f(t) = \text{real} \left(\sum_{n=0}^{\infty} a_n e^{in\omega t} \right) \quad (2.14)$$

with $\omega = \frac{2\pi}{T}$.

a_0 is simply the (real part of the) time-average of $f(t)$, since the averages of sine and cosine functions are zero over one period. To find the other coefficients, a_k , Fourier's trick was to multiply Eq.2.14 with $e^{-ik\omega t}$ and time-average the resulting equation:

$$a_k = \frac{2}{T} \int_0^T f(t) e^{-ik\omega t} dt \quad (2.15)$$

Fourier exploited in his trick the fact that the terms in the Fourier series are orthogonal over the period T since the following identities hold for any integers n and m different from zero:

$$\int_0^T \sin n\omega t \cos m\omega t dt = 0 \quad (2.16)$$

$$\int_0^T \sin n\omega t \sin m\omega t dt = \frac{T}{2} \delta_{mn} \quad (2.17)$$

$$\int_0^T \cos n\omega t \cos m\omega t dt = \frac{T}{2} \delta_{mn} \quad (2.18)$$

$$\delta_{mn} = \begin{cases} 1 & \text{for } m = n \\ 0 & \text{for } m \neq n \end{cases} \quad (2.19)$$

All harmonics are mutually orthogonal over T due to trigonometric identities, and hence it is clear that Fourier decomposition is an orthogonal decomposition.

2.2.6 Proper Orthogonal Decomposition

The proper orthogonal decomposition (POD) is a method that is used to reduce the data in an efficient way as follows: The data is expanded in terms of ortho-normal base vectors such that this representation is optimal in the sense that the required number of terms recovering the kinetic energy of the field is minimal (i.e. if the data is velocity data). The method can be used to extract spatially dominant features, i.e. coherent structures, from space-time data, in this case data obtained by LES (Holmes, Lumley, and Berkooz, 1996). The data $u(y, t)$ is decomposed into a set of N empirical, mutually orthogonal eigenfunctions, or POD modes, $\phi_n(y)$. The random variable u can then be reconstructed from linear combinations of the POD modes which are multiplied with the amplitude coefficients $c_n(t)$. The POD modes are purely spatial correlations with no time dependence. The amplitude coefficients are independent of space and simulate the amplitude of the corresponding POD mode as function of time. Thus, the POD of u into N modes is called u_N and given by Eq.2.20.

$$u_N(y, t) = \sum_{n=0}^N c_n(t) \phi_n(y) \quad (2.20)$$

The POD modes are chosen such that the difference between u and u_N in L^2 -norm is minimal on average. This is the case if and only if the normalized average projection of u onto ϕ is larger than onto any other set of basis modes ψ for any number of modes N . This maximum condition is expressed in Eq.2.21 (Berkooz, Holmes, and Lumley, 1993).

$$\max_{\psi} \frac{\langle (u, \psi)^2 \rangle}{(\psi, \psi)} = \frac{\langle (u, \phi)^2 \rangle}{(\phi, \phi)} \quad (2.21)$$

The notation (f, g) stands for the inner product $(f, g) = \int f g^* dy$ where g^* denotes the complex conjugate of g . It is advantageous to allow complex values in a general context. In this case all functions ϕ are real. The maximum problem is not a problem of ordinary calculus but of the calculus of variations (Feynman, Leighton, and Sands, 1963). One has to find the maximum of $\langle (u, \psi)^2 \rangle$ under the normalization constraint $(\psi, \psi) = 1$. Applying the method of Lagrange multipliers one maximizes $J(\psi)$ with:

$$J(\psi) = \langle (u, \psi)^2 \rangle - \lambda((\psi, \psi) - 1) \quad (2.22)$$

Suppose ϕ is the true function which maximizes J , then add an arbitrary variation $\delta\omega$ to obtain fake functions $\psi = \phi + \delta\omega$. δ is an arbitrary scalar and ω an arbitrary function. Plugging in gives:

$$\begin{aligned} J(\phi + \delta\omega) &= \langle (u, \phi + \delta\omega)^2 \rangle - \lambda((\phi + \delta\omega, \phi + \delta\omega) - 1) \\ &= \langle (u, \phi)^2 + 2\delta(u, \phi)(u, \omega) + \delta^2(u, \omega)^2 \rangle \\ &\quad - \lambda((\phi, \phi) + 2\delta(\phi, \omega) + \delta^2(\omega, \omega) - 1) \end{aligned} \quad (2.23)$$

Since ϕ maximizes J , any change in ϕ must result in a second order variation in J . A necessary condition is therefore:

$$\frac{\partial J(\phi + \delta\omega)}{\partial \delta} = 0 \quad (2.24)$$

The derivative of J with respect to the arbitrary scalar δ is written out:

$$\langle 2(u, \phi)(u, \omega) + 2\delta(u, \omega)^2 \rangle - \lambda((2(\phi, \omega) + 2\delta(\omega, \omega))) = 0 \quad (2.25)$$

For the true function $\delta = 0$, and the derivative becomes:

$$\langle (u, \phi)(u, \omega) \rangle - \lambda(\phi, \omega) = 0 \quad (2.26)$$

Writing out the integrals gives:

$$\langle \int u(y')\phi(y')dy' \int u(y)\omega(y)dy \rangle - \lambda \int \phi(y)\omega(y)dy = 0 \quad (2.27)$$

Integration and averaging commutes:

$$\int \int \langle u(y')u(y) \rangle \phi(y')dy'\omega(y)dy - \lambda \int \phi(y)\omega(y)dy = 0 \quad (2.28)$$

Factoring out the common term gives:

$$\int [\int \langle u(y')u(y) \rangle \phi(y')dy' - \lambda\phi(y)]\omega(y)dy = 0 \quad (2.29)$$

Since $\omega(y)$ is arbitrary, the bracket must be zero.

$$\int \langle u(y')u(y) \rangle \phi(y')dy' = \lambda\phi(y) \quad (2.30)$$

Thus a necessary condition for a maximum of J is that ϕ is an eigenfunction of the average autocorrelation function of the random variable. Hence one has to solve the eigenvalue problem Eq.2.30. Since measurements and computations provide discrete values, one cannot obtain eigenfunctions, but must seek eigenvectors instead (which are also called POD modes). The

two-point correlation tensor of the random variable replaces the autocorrelation function in this case. This follows from the definition of the Riemann integral:

$$\int_a^b f(x)g(x)dx = \lim_{n \rightarrow \infty} \sum_{i=1}^n f(x_i)g(x_i) \frac{b-a}{n} \quad (2.31)$$

For a data set of size N the two-point autocorrelation tensor, which is a second order tensor, can be written as $N \times N$ matrix in Eq.2.32 in which u^T stands for the transpose of u . The problem for discrete samples is to find the eigenvalues and corresponding eigenvectors of the two-point autocorrelation tensor as stated in Eq.2.33. Since R is symmetric and positive semi-definite, all eigenmodes are orthogonal and all eigenvalues are non-negative and real.

$$R = \langle \vec{u}\vec{u}^T \rangle \quad (2.32)$$

$$R\vec{\phi} = \lambda\vec{\phi} \quad (2.33)$$

The eigenvalue λ_n is the variance of the random variable set in the direction of the eigenmode $\vec{\phi}_n$. It has the dimension of the square of the random variable (see Eq.2.33). In particular, if the random variable is a velocity, the eigenvalues have the dimension of specific energy. Therefore the eigenvalues are ordered by magnitude, and the set of the largest N eigenvalues contains the most energetic modes $\vec{\phi}_n$: Coherent structures. The total energy is then the sum of all eigenvalues. The fraction of energy k_n in the mode $\vec{\phi}_n$ is therefore given by Eq.2.34.

$$k_n = \frac{\lambda_n}{\sum_{i=1}^N \lambda_i} \quad (2.34)$$

For POD in two and three dimensions the $N \times N$ eigenvalue problem soon becomes impractical to solve as N , the number of data points, becomes large. Sirovich (1987) realized that the $N \times N$ eigenvalue problem can be reduced to the much smaller $M \times M$ eigenvalue problem by a simple substitution. M is the number of samples or snapshots of the flow field. This method is called method of snapshots. Sirovich (1987) noted simply that the samples from the data set are linear combinations of the POD eigenvectors (Eq.2.35). It must be assumed that the snapshots are linearly independent.

$$\vec{\phi} = \sum_{k=1}^M a_k \vec{u}_k \quad (2.35)$$

Equation 2.35 can be substituted in the eigenvalue problem Eq.2.33. The result of this substitution is Eq.2.36

$$\left(\frac{1}{M} \sum_{i=1}^M \vec{u}_i \vec{u}_i^T, \sum_{k=1}^M a_k \vec{u}_k\right) = \lambda \sum_{i=1}^M a_i \vec{u}_i \quad (2.36)$$

The left hand side of Eq.2.36 is still the inner product of an $N \times N$ matrix and a vector of dimension N . It can be written out explicitly which gives the following N -dimensional vector:

$$\left(\frac{1}{M} \sum_{i=1}^M \vec{u}_i \vec{u}_i^T, \sum_{k=1}^M a_k \vec{u}_k\right) = \frac{1}{M} \sum_{i=1}^M \vec{u}_i \sum_{k=1}^M (\vec{u}_i, \vec{u}_k) a_k \quad (2.37)$$

Plugging Eq.2.37 in Eq.2.36 gives:

$$\sum_{i=1}^M \left(\sum_{k=1}^M \frac{1}{M} (\vec{u}_i, \vec{u}_k) a_k - \lambda a_i\right) \vec{u}_i = 0 \quad (2.38)$$

As the components of \vec{u} are linearly independent, the brackets must be zero.

$$\sum_{k=1}^M \frac{1}{M} (\vec{u}_i, \vec{u}_k) a_k = \lambda a_i \quad (2.39)$$

for $i = 1, \dots, M$. Thus, one obtains an $M \times M$ eigenvalue problem for the coefficients a_i .

2.3 Turbulence Scales

Turbulent flows contain a wide range of length scales due to eddies of different sizes. The energy spectrum (Fig.2.2) shows the distribution of kinetic energy over the wavenumber of these eddies for a fully developed turbulent flow. The various wavenumbers in the energy spectrum can be divided with respect to their sizes: Since the large-scale eddies contain most of the kinetic energy, they make up the *energy containing range*. These eddies depend on the particular flow geometry and parameters. The smaller eddies make up the *universal equilibrium range* which is according to Kolmogorov's hypotheses statistically similar or universal for all high Reynolds number flows. It can be subdivided into *inertial subrange* and *dissipation subrange*, depending on whether inertial or dissipative effects are dominant. In the view of the *energy cascade*, energy is continuously transferred from large eddies to small eddies where it is dissipated. This range is dubbed 'equilibrium' as the energy

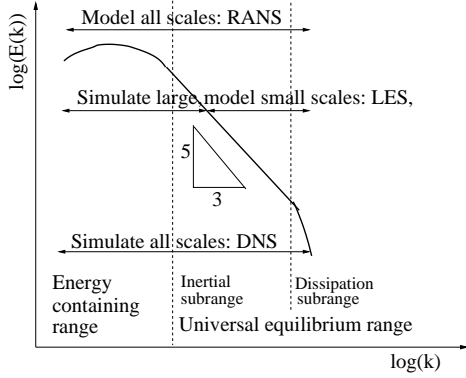


Figure 2.2: Energy spectrum in a turbulent flow

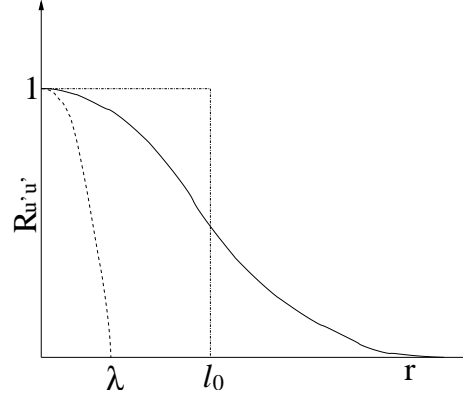


Figure 2.3: Autocorrelation coefficient over the distance

transfer from large to small eddies is thought to be independent of the scale of the eddy, i.e. the energy flux from the large eddies equals the energy flux to the small eddies for any particular eddy size in this range. Three important ranges of scales have emerged in the discussion about turbulence, the integral scales, the Taylor scales, and the Kolmogorov scales. The largest eddies are of the size of the integral length scale, and the smallest eddies are of the size of the Kolmogorov length scales. The mean distance for which the velocity fluctuations are correlated gives an estimate for the integral length scales. The autocorrelation function $R_{u'u'}$ is:

$$R_{u'u'}(r, x) = \frac{\overline{u'(x)u'(x+r)}}{\overline{u'(x)u'(x)}} \quad (2.40)$$

$u'(x)$ is the velocity fluctuation in point x , $u'(x+r)$ is the velocity fluctuation at a distance r from x . The overbar represents a time-average. The integral length scales l_0 can be estimated as:

$$l_0 = \int_0^\infty R_{u'u'}(r) dr \quad (2.41)$$

The autocorrelation function and an estimate for the integral length scales are plotted in Fig.2.3. The integral velocity scales u'_0 can be estimated as the RMS of u . The integral time scales τ_0 are then:

$$\tau_0 = \frac{l_0}{u'_0} \quad (2.42)$$

A turbulence Reynolds number Re_T is defined based on the integral scales:

$$Re_T = \frac{u'_0 l_0}{\nu} \quad (2.43)$$

The smallest scales are the Kolmogorov scales. According to Kolmogorov's first hypothesis, they depend on dissipation ϵ and viscosity ν only, if the turbulence Reynolds number is large. The dimensions of ϵ and ν are $\frac{m^2}{s^3}$ and $\frac{m^2}{s}$. The only possible combinations which have the dimensions of length, time, and velocity are, respectively:

$$\eta \sim \left(\frac{\nu^3}{\epsilon}\right)^{\frac{1}{4}} \quad (2.44)$$

$$\tau_\eta \sim \left(\frac{\nu}{\epsilon}\right)^{\frac{1}{2}} \quad (2.45)$$

$$u_\eta \sim (\nu\epsilon)^{\frac{1}{4}} \quad (2.46)$$

These are the Kolmogorov length scales η , the Kolmogorov time scales τ_η , and the Kolmogorov velocity scales u_η . It follows immediately that the Reynolds number based on the Kolmogorov scales is on the order of unity:

$$Re_\eta = \frac{u_\eta \eta}{\nu} \sim 1 \quad (2.47)$$

The integral length and velocity scales are on the same order of magnitude as the characteristic length and velocity scales of the particular problem (or somewhat less), and therefore also the turbulence Reynolds number Re_T is large if the Reynolds number Re is large. It follows for any flow with high Reynolds number that viscosity is unimportant for the largest eddies.

If the turbulence Reynolds number is very high, then there is according to Kolmogorov's second hypothesis a range of scales, the inertial subrange, which depends on the dissipation ϵ and the wavenumber k only, but not on viscosity. The Taylor length scales λ belong to this range. They are larger than the Kolmogorov length scales yet smaller than integral length scales. The corresponding time and velocity scales are τ_λ and u_λ , respectively. The independence of the large scales on viscosity implies an estimate for the kinetic energy flux from the large eddies to the small eddies (energy cascade). The energy flux can only depend on the velocity scale and the length scale (and on the density), but not on viscosity. The only possible combination which has the dimension of dissipation of energy gives a scaling rule describing the energy cascade:

$$P \sim \frac{u_0'^3}{l_0} \sim \frac{u_\lambda^3}{\lambda} \sim \frac{u_\eta^3}{\eta} \sim \nu \frac{u_\eta^2}{\eta^2} \sim \epsilon \quad (2.48)$$

The ratio of the Kolmogorov and the integral scales can be estimated from Eq.2.48 and Eq.2.44-2.46:

$$\frac{\eta}{l_0} \sim Re_T^{-\frac{3}{4}} \quad (2.49)$$

$$\frac{\tau_\eta}{\tau_0} \sim Re_T^{-\frac{1}{2}} \quad (2.50)$$

$$\frac{u_\eta}{u'_0} \sim Re_T^{-\frac{1}{4}} \quad (2.51)$$

Based on dimensional arguments, the slope of the turbulent kinetic energy spectrum in the inertial subrange can be derived to be $-5/3$ with logarithmic axes as shown in Fig.2.2:

$$E(k) \sim \epsilon^{\frac{2}{3}} k^{-\frac{5}{3}} \quad (2.52)$$

The Taylor length scales λ are scales on a size between the integral scales and the Kolmogorov scales. They are defined as the intersection point of the parabola shown in Fig.2.3 with the abscissa. The parabola has the same ordinate, gradient, and curvature as the autocorrelation function at $r = 0$. The Taylor length scales have no physical significance, other than being intermediate scales which lie in the inertial subrange. The Taylor length scales can be interpreted as the length scales which would be dissipative based on the assumption that the velocity scale does not change over all length scales (Panton, 2005). This is not physical as the energy spectrum clearly reveals (Fig.2.2) though the velocity scale does drop only as the third root of the length scale (see Eq.2.48).

$$\epsilon \sim \nu \frac{u_\eta^2}{\eta^2} \sim \nu \frac{u'_0{}^2}{\lambda^2} \quad (2.53)$$

$$\frac{\lambda}{\eta} \sim \frac{u'_0}{u_\eta} \sim Re_T^{\frac{1}{4}} \quad (2.54)$$

$$\frac{\lambda}{l_0} \sim \frac{\lambda}{\eta} \frac{\eta}{l_0} \sim Re_T^{\frac{1}{4}} Re_T^{-\frac{3}{4}} \sim Re_T^{-\frac{1}{2}} \quad (2.55)$$

2.4 Turbulence Modeling

Turbulent flows are governed by the continuity and Navier-Stokes equations. Due to the wide range of scales inherent in turbulent flows, averaging methods may be necessary if the computer power is insufficient. Furthermore, turbulent flows in scientific and engineering applications have meaning only in terms of averaged data as discussed in Sec.2.2. In the following, three

different approaches are discussed with respect to the present flow case. The Navier-Stokes equations in the low Mach number limit (incompressible flow) are more fully discussed in Ch.4. They reflect the conservation of mass and momentum, respectively:

$$\frac{\partial u_i}{\partial x_i} = 0 \quad (2.56)$$

$$\frac{\partial u_i}{\partial t} + u_j \frac{\partial u_i}{\partial x_j} = -\frac{\partial p}{\partial x_i} + \frac{1}{Re} \frac{\partial^2 u_i}{\partial x_j^2} \quad (2.57)$$

2.4.1 Direct Numerical Simulation

In direct numerical simulation (DNS) all scales are resolved and hence there is obviously no need for any turbulence model. It is considered only in order to relate it to other modeling approaches. The Kolmogorov length- and time scales are resolved and that implies that the numerical (spatial) resolution is higher than that of the Kolmogorov length scale. That is, the number of computational nodes N can be estimated by $N \sim (l/\eta)^3 \sim Re_T^{9/4}$. Further, since the time step size is proportional to the cell size (for equal Courant number), the required number of time steps scales also as $Re_T^{3/4}$. The computation time scales thus as Re_T^3 . In the near future, DNS will be restricted to low Reynolds number flows and simple geometries. As the resolution in space and time approaches zero, the Navier-Stokes equations are recovered. Therefore, DNS should be considered to be an *approximation* to the solution of the Navier-Stokes equations rather than a *model*. In applications related to gas turbines, e.g. the JICF, the Reynolds number is clearly too high for DNS.

2.4.2 Reynolds-Averaged Navier-Stokes Equations

In the Reynolds-averaged Navier-Stokes (RANS) approach the governing equations are time- or ensemble-averaged *a priori*. This has the advantage that time-averaged solutions can be computed fast: Since turbulence length scales are not resolved, the grid resolution is given by the length scales of the mean flow. As the governing equations are averaged, dynamic phenomena on time scales which are on the same order as turbulence time scales cannot be computed. Averaging also brings about the closure problem:

$$\frac{\partial \bar{u}_i}{\partial t} + \bar{u}_j \frac{\partial \bar{u}_i}{\partial x_j} = -\frac{\partial \bar{p}}{\partial x_i} + \frac{1}{Re} \frac{\partial^2 \bar{u}_i}{\partial x_j^2} - \frac{\partial \overline{u'_i u'_j}}{\partial x_j} \quad (2.58)$$

The closure problem is evident in the appearance of new terms in the averaged momentum equations. The new terms are called the Reynolds stresses τ_{ij} . They arise from Reynolds-averaging the convective terms in Eq.2.57.

$$\tau_{ij} = -\overline{u'_i u'_j} \quad (2.59)$$

The correlations of fluctuation velocities are unknown and have to be closed. These models, as a rule, lack resolution information. The Navier-Stokes equations are not recovered as the resolution in space approaches zero. Hence, RANS modeling must be classified as a *model*, and not as an *approximation*. A widespread closure hypothesis is Boussinesq's hypothesis, an assumed analogy between molecular diffusion and turbulent diffusion. The viscosity is argued to depend on turbulence time scales and length scales which are computed from the solution of additional transport equations, e.g. for the turbulent kinetic energy and its dissipation rate. Flows containing certain features are typically not computed accurately if turbulence modeling involves the Boussinesq hypothesis, e.g. flow with streamline curvature, anisotropy, flow separation, unfavorable pressure gradient, system rotation (Wilcox, 1993).

The deficiencies associated with the Boussinesq hypothesis can be overcome using an alternative closure: Reynolds stress models (RSM). In this approach, six transport equations are written for the six Reynolds stresses and an additional transport equation for the dissipation rate of the turbulent kinetic energy. The Reynolds stress transport equations in turn are unclosed and have to be closed by modeling.

If the time term in Eq.2.58 is retained, one speaks about unsteady RANS (URANS). It is applicable if the transient time scale τ_{trans} it describes is much larger than all turbulence time scales, especially the integral time scales τ_0 . One must have:

$$\tau_{trans} \gg \tau_0 \quad (2.60)$$

It has not been possible to deduce a consistent equation for statistical quantities of turbulence, e.g. the turbulent kinetic energy, if there is no separation of scales. The eddy viscosity ν_T is estimated from these equations, e.g. from the turbulent kinetic energy and its dissipation. The turbulent kinetic energy contains, by definition, all turbulence time scales: If there is no spectral gap, the k -equation does not contain all turbulent kinetic energy and is clearly not a transport equation for the turbulent kinetic energy. Thus URANS equations are inconsistent if there is no spectral gap. The same argument can be made for any statistical turbulence quantity.

The JICF is inherently unsteady and is dominated by large-scale coherent structures (with no spectral gap). For such flows, one important deficiency

of RANS models is that they are already conceptually not able to capture dynamic phenomena on turbulence time scales as *time-averaged* equations are solved.

2.4.3 Large Eddy Simulation

DNS is far out of reach for current computers. RANS modeling has several shortcomings. In LES, small scales are separated from large scales by a filtering technique. The large scales are resolved whereas the small scales are filtered out *a priori*. This approach is motivated by Kolmogorov's hypothesis: The small scales are thought to be universal and independent of specific flow realizations. The large scales, on the other hand, depend on the geometry and the problem parameters. The hope is then that general descriptions for the universal small-scale turbulence can be formulated while transport equations are solved for the non-universal large scales. The approach is justified based on the assumption that the unresolved turbulent kinetic energy is small with the imposed resolution or can be accounted for (i.e. modeled reasonably well). It is possible to resolve most of the turbulent kinetic energy as the amplitude of the unresolved turbulent kinetic energy decays more than linearly. Filtering is done with the filter function F :

$$\tilde{\phi}(\vec{x}_0, t) = \int_{-\infty}^{\infty} F(\vec{x} - \vec{x}_0) \phi(\vec{x}, t) d\vec{x} \quad (2.61)$$

The filter function is applied to the continuity and Navier-Stokes equations:

$$\frac{\partial \tilde{u}_i}{\partial x_i} = 0 \quad (2.62)$$

$$\frac{\partial \tilde{u}_i}{\partial t} + \tilde{u}_j \frac{\partial \tilde{u}_i}{\partial x_j} = -\frac{\partial \tilde{p}}{\partial x_i} + \frac{1}{Re} \frac{\partial^2 \tilde{u}_i}{\partial x_j^2} + \frac{\partial \tau_{ij}}{\partial x_j} \quad (2.63)$$

Due to the volume-averaging procedure new terms in the filtered Navier-Stokes equations appear:

$$\tau_{ij} = -(\widetilde{u_i u_j} - \tilde{u}_i \tilde{u}_j) \quad (2.64)$$

Those terms are referred to as *residual* or *subgrid scale stresses (SGS)*, even though conceptually a difference between the filter and the grid is desirable. However, usually the numerical grid is the only filter (an implicit filter), and hence the term SGS is appropriate. As in the RANS framework, a closure hypothesis has to be introduced. Since closure hypotheses should ensure that the subgrid scale stresses are identically zero for infinitely fine resolution, the Navier-Stokes equations are recovered in this limit. Therefore,

LES qualifies as an *approximation*. The closure should account for dissipation at the smallest scales. Furthermore, the SGS model should account for the effect of small scales on the resolved ones (through the so-called backscatter). Some alternative closures are as follows:

- Smagorinsky model (Smagorinsky, 1963)
- Scale Similarity Model (Bardina, Ferziger, and Reynolds, 1980)
- Dynamic Model (Germano, Piomelli, Moin, and Cabot, 1991)
- Dynamic Divergence Model (Held and Fuchs, 1998)
- Exact Differential Model (Fuchs, 1996)
- No explicit SGS model, i.e. "Implicit Model", e.g. Pope (2000) or Sagaut (1998)

In this thesis, no explicit SGS model is applied. Dissipation is given implicitly by the numerical scheme. The implicit model can be justified if large parts of the energy spectrum are resolved. Then the unresolved eddies contain little energy which can therefore be neglected. As the resolution improves, the implicit model has an increasing level of acceptance, since there is an increasing separation of scales between the neglected eddies and the largest eddies. Since LES can be regarded as an approximation to DNS, it follows that there is no need for an explicit SGS turbulence model if just the resolution is fine enough. The implicit form of the dissipation of the SGS depends on the numerical scheme, and any stable high-order scheme can. Furthermore, it has been demonstrated that the discretization error is often of the same order as the subgrid scale stress terms for the high wavenumber end of resolvable waves, and therefore the discretization intrinsically interacts with subgrid scale modeling (Ghosal, 1996; Kravchenko and Moin, 1997). The implicit model has been applied in many LES applications (Olsson and Fuchs, 1996, 1998; Gullbrand, Bai, and Fuchs, 2001).

In LES, the required resolution goes down to the Taylor scales below which turbulence is thought to be universal. This gives an estimate for the necessary number of grid points: $N \sim (l/\lambda)^3 \sim Re_T^{3/2}$. As the time step size is proportional to the cell size, $o(Re_T^{1/2})$ time steps are required for a simulated time on the order of the integral time scales. Therefore, the computational time scales as Re_T^2 . Pope (2004) claims the cross-over point between necessary and available computer resources with respect to LES has been reached, and LES will be applied to complex engineering problems at high Reynolds in the near future.

Chapter 3

Jets in Crossflow

Jets in crossflow (JICF) have been studied for some seventy years, beginning with studies of chimney exhaust plumes and the dispersion of smoke. Other examples for applications of JICF are roll control and thrust vector control of rockets, vertical take-off / landing aircraft, or fuel injection, blade cooling, and hot gas dilution in gas turbines. Margason (1993) reviews JICF research beginning from the thirties and provides an exhaustive list of references concerning experiments and computations. The present review therefore emphasizes literature thereafter.

The flow field of JICF (see Fig.3.1) is three-dimensional and unsteady. The transverse jet describes a curved trajectory as it bends into the crossflow. The term "crossflow" is the common terminology for the main channel flow, in which the transverse jet is injected. A JICF flow field may be divided into the *jet region*, in which the deflection of the jet is still small, and a *wake-like region* in which the jet is almost aligned with the crossflow. In between there is a region of high jet trajectory curvature. Several vortex systems form in a JICF flow field: The most obvious is the *counter-rotating vortex pair* (CVP). Other coherent structures are *horseshoe vortices*, *wake vortices*, and *jet shear layer vortices*. The concepts of a *near-field* and a *far-field* of JICF constitute another useful description of the flow. In the far-field, $x/D \gg 1$, the jet may be regarded as point source of momentum and mass. The jet region, the horseshoe vortices, and the jet shear layer layer vortices are best described in the near-field while the CVP and the wake-like character are most evident in the far-field.

The present investigation is motivated by the fact that JICF can be applied in gas turbines to enhance mixing in premixing tubes. The mixing is enhanced in small and large scales by a corresponding increase in turbulence level and by presence of unsteady coherent structures (Papers IV and V). Also, compared to free jets, mixing is faster due to enhanced entrainment of

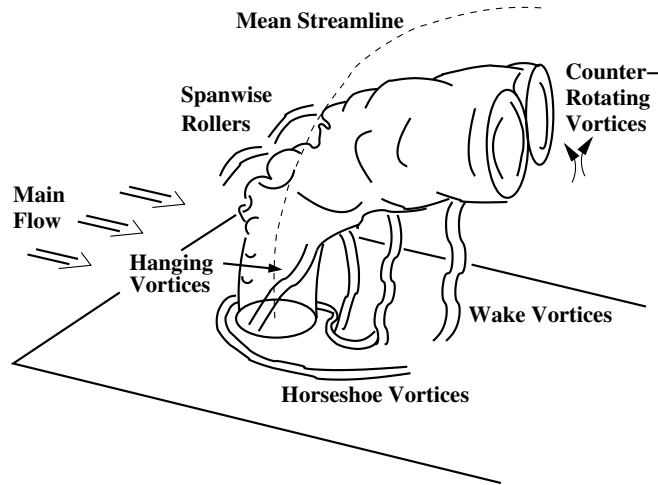


Figure 3.1: Coherent Structures JICF flow fields (adapted from Fric and Roshko (1994))

crossflow into the jet, after which molecular mixing can occur in regions of steep mixture fraction gradients.

LES offers the opportunity to track the coherent structures mentioned above accurately in space and time. These coherent structures are the main contributor to large-scale mixing, and therefore essential advantages are gained by applying LES. Especially in the JICF there are various mutually interacting coherent vortices, and this interaction can be accurately tracked by LES. For multiphase flow, additionally the interaction of the continuous phase and the droplets can be described accurately with LES, as droplets tend to have stronger interaction with large eddies, and these are not modeled but simulated.

In this chapter the flow topology of JICF is outlined, an overview of previous experimental and computational work is given, mechanisms leading to the formation of the vortex systems and to jet bending are discussed, and characteristic parameters are defined. A distinction between JICF with a single phase and the injection of a liquid spray into the crossflow is reflected in the organization of this chapter: To clearly separate the impact of multiphase flow on the flow field of JICF, a single-phase JICF is reviewed first without the complication due to multiphase flow phenomena. Thereafter, spray JICF are considered separately. A literature overview is given, and additional questions due to multiphase flow phenomena are discussed.

3.1 Characteristic Parameters

The momentum flux ratio J (Eq.3.1), the velocity ratio R (Eq.3.2) or the effective velocity ratio R_e (Eq.3.3) are frequently used to characterize the flow field. The effective velocity ratio is the square root of the momentum flux ratio. If the density of the jet fluid and crossflow fluid are equal, the effective velocity ratio becomes the velocity ratio. The subscript "cf" stands for crossflow.

$$J = \frac{\rho_{jet} V_{jet}^2}{\rho_{cf} V_{cf}^2} \quad (3.1)$$

$$R = \frac{V_{jet}}{V_{cf}} \quad (3.2)$$

$$R_e = \sqrt{\frac{\rho_{jet} V_{jet}^2}{\rho_{cf} V_{cf}^2}} \quad (3.3)$$

Various JICF regimes can be identified in terms of the effective velocity ratio, e.g. Smith and Mungal (1998). Obviously, the higher the effective velocity ratio, the deeper the jet penetrates into the main flow. In the limit of very small effective velocity ratio, the jet remains unnoticed in a channel flow; in the limit of very large effective velocity ratio, a free jet develops into essentially quiescent fluid. Velocity ratios of $R_e \sim 0.5 - 2$ are investigated by Andreopoulos and Rodi (1984) using hot wire anemometry in a wind tunnel. At $R_e \sim 0.5$ the main flow merely curves over the jet exit and reattaches few diameters afterwards where there is no evidence for a CVP. This regime is suitable for film cooling applications. At $R_e \sim 1 - 2$, the CVP is attached to the wall and is still evident six and ten diameters downstream, respectively. Fric and Roshko (1994) perform their wind tunnel experiments at $R_e \sim 4 - 5$. In this regime the lower jet boundary is close to the wall, and the formation of wake vortices and the entrainment of main flow boundary layer fluid into the wake are most pronounced. Smith and Mungal (1998) visualize the regimes from $R_e \sim 10 - 200$ by laser-induced fluorescence (LIF): At $R_e \sim 10$, the jet penetrates fully into the main flow, and no jet fluid enters the wake of the jet; at $R_e \sim 20 - 100$, there is evidence of jet fluid in the wake of the jet; and at $R_e \sim 200$, the lower part of the jet has characteristics of a free jet.

The trajectory of the jet can be defined in many ways which may lead to significantly varying reported trajectories. Some of these are discussed in Su and Mungal (2004) or Paper V. Fearn and Weston (1974) provide empirical back-of-the-envelope rules for the trajectory of the jet and the vortex curve. The jet trajectory in Eq.3.4 is defined as the mean streamline through the

nozzle center. The vortex curve is the locus of maximum upwash between the two vortices of the CVP (Eq.3.5).

$$\frac{y}{D} = 0.9772R_e^{0.9113}\left(\frac{z}{D}\right)^{0.3346} \quad (3.4)$$

$$\frac{y}{D} = 0.3473R_e^{1.127}\left(\frac{z}{D}\right)^{0.4291} \quad (3.5)$$

y is the penetration, z the downstream distance, and D is the nozzle diameter. The experimentally fitted curves are valid for circular nozzles. In Paper V the current LES is compared to the experimental data which Fearn and Weston (1974) used to fit this rule and satisfactory agreement between simulation and experiment was noted. However, there is considerable scatter in the literature data concerning trajectories, even for nominally the same conditions. Hasselbrink and Mungal (2001a) and Hasselbrink and Mungal (2001b), who apply particle image velocimetry (PIV) and laser-induced fluorescence (LIF) of OH radicals, derive further scaling rules. In addition to the momentum flux ratio, Muppidi and Mahesh (2005) show that the lift-off of the jet into the main flow also increases with the boundary layer thicknesses of jet and crossflow. Turbulence levels and confinement also influence the jet trajectory (Kamotani and Greber, 1974). The possibility to change the flow by varying the nozzle geometry is discussed in Sec.3.4.

3.2 Jet Deflection Mechanisms

The mechanisms due to which JICF bend into the main flow direction are discussed in Yuan and Street (1998). The jet deflects due to momentum exchange with the main flow by entrainment and pressure difference. Entrainment of ambient fluid into the jet enhances momentum transfer from the main flow fluid to the jet fluid in the main flow direction. The large-scale coherent structures provide fluid with high streamwise momentum to the jet interior where momentum is exchanged efficiently in regions with high velocity gradients. In the lower part of the jet the quasi-steady hanging vortices (Sec.3.3.3) at the lateral sides of the nozzle are the most significant contributors of entrainment. The spanwise rollers (Sec.3.3.3) undulate the jet, but pockets of main flow fluid are not frequently observed in the jet. In the region of strongest curvature in the jet trajectory, the spanwise rollers deform the jet surface so severely that pockets of main flow fluid penetrate the jet (Yuan and Street, 1998). This mixing is the reason for the efficient momentum transfer in this region which is evident in the strong curvature

of the jet. Pressure drag is a second mechanism which is responsible for the bending of the jet. Upstream of the jet the pressure is high, downstream in the wake low. The pressure difference gives rise to a pressure drag. Yuan and Street (1998) compute the pressure drag for a JICF to be about twice as large as the pressure drag of a corresponding solid cylinder. The reason for the high pressure drag is the different shape of the cross sectional areas: The concave curvature on the downstream side results in a lower downstream pressure. The pressure drag drops sharply along the jet trajectory.

3.3 Coherent Structures

Coherent structures are large-scale, turbulent, frequently occurring, vortical flow patterns. Fric and Roshko (1994) describe four types of coherent structures in the flow field of a JICF: A so-called counter-rotating vortex pair (CVP), horseshoe vortex systems, jet shear layer vortices, and wake vortices. Those vortex systems are shown in Fig.3.1. To understand the formation and transport of vortices, the transport equation of vorticity gives valuable insight. It can be obtained by taking the curl of the Navier-Stokes equations, here for incompressible, isothermal, barotropic flow of Newtonian fluid with no body forces:

$$\frac{D\omega}{Dt} = \omega \nabla u + \frac{1}{Re} \nabla^2 \omega \quad (3.6)$$

For the above mentioned conditions, there is no explicit source term in the vorticity transport equation. Therefore, vorticity can only be introduced through the boundaries. The vorticity is convected (the left hand side terms in Eq.3.6) and modified through vortex stretching and viscous diffusion (the first and second terms on the right of Eq.3.6, respectively). For JICF it follows that all vorticity has its origin in the injection pipe of the jet and the main flow boundary layer, but not in the CVP, as Fric and Roshko (1994) first realize in the late eighties. The vorticity is merely reoriented and stretched and diffuses as is evident from the vorticity transport equation.

3.3.1 Counter-Rotating Vortex Pair

The formation of the CVP is still a research topic. In the eighties the CVP was viewed as a far-field phenomenon which forms due to the jet momentum (Broadwell and Breidenthal, 1984). In analogy to the CVP of finite wing sections, the transverse jet was understood as point source of lift and it was argued that the lift or transverse momentum flux generates the CVP. In the

nineties, a near-field view is generally agreed upon: The CVP is thought to be initiated by the vorticity in jet shear layer as e.g. Haven and Kurosaka (1997) explain. The nozzle sidewall vorticity is aligned with the mean flow direction and convects into the far-field within the CVP. The nozzle upstream and downstream wall vorticity can be tilted and reoriented in streamwise direction. It is reasonable to assume that the main flow boundary layer vorticity plays a lesser role in the initialization of the CVP, as a CVP also forms downstream of extended tubes in the main flow, e.g. chimneys, and in computations with slip boundary conditions on the lower wall, e.g. Sykes, Lewellen, and Parker (1986). The exact mechanism of vortex tilting and stretching, which leads to the formation of the CVP, is under investigation by several researchers and no generally accepted mechanism has emerged as yet.

Kelso, Lim, and Perry (1996) suggest that the jet vorticity rolls up periodically to form vortex rings in analogy with a free jet. These vortex rings are then thought to fold and tilt due to interaction with the main flow. The vortex sheet from the nozzle exit to the vortex ring then folds, and a secondary vortex ring is formed which in turn is folded and tilted. The downstream branch of the secondary vortex ring contributes to the vorticity of the CVP. Cortelezzi and Karagozian (2001) apply potential flow and vortex methods in which discrete vortex elements are tracked in Lagrangian coordinates. The main flow has constant velocity outside the boundary layer of constant thickness and a cubic velocity profile inside the boundary layer. The vortex elements which model the jet are convected in the velocity field superposed from the underlying main flow and Biot-Savart integrated induced velocities of all vortex elements. Cortelezzi and Karagozian (2001) confirm the mechanism proposed by Kelso et al. (1996) and show that the zone of largest vorticity coincides with the downstream branch of folded secondary vortex rings. They suggest that the CVP originates from the time-averaged jet shear layer vortices described below.

Yuan, Street, and Ferziger (1999) and Yuan and Street (1998) compute the flow field and scalar concentrations with LES. In these studies, a JICF flow field is simulated qualitatively, and coherent structures match flow visualizations, but to obtain experimental data also quantitatively, different Reynolds number and momentum flux ratios are used. They argue that a sequence of vortex rings postulated by Kelso et al. (1996) and later advocated by Cortelezzi and Karagozian (2001) is misleading as the mixing layer is skewed. They do not observe vortex rings in LES but vortices of different classes which are dubbed spanwise rollers, vertical streaks, and hanging vortices (see Sec.3.3.3). They confirm the observation of Kelso et al. (1996) that the hanging vortex pair on the lateral sides of the nozzle contributes to

initialize the CVP. They also confirm the occurrence of vortex breakdown. They propose an alternative formation mechanism for the CVP: The fluid in the hanging vortices on opposing lateral sides of the nozzle is observed to come from the skewed mixing layer from the same side only. This means firstly that the sign of vorticity in jet direction is opposite on each site due to roll-in towards the centerplane, and secondly that the sign of vorticity in the main flow direction is opposite, too, due to roll-in on opposite side of the upward forcing jet. Fluid with vorticity of opposite signs flows upwards through the hanging vortices up to the vortex breakdown. Whereas vertical vorticity above the breakdown location is found on both lateral sides of the jet, the streamwise vorticity of opposite sign remain on their sides of the jet and form a weak CVP. The CVP formation is delayed with increasing effective velocity ratio (Smith and Mungal, 1998). The CVP is known to interact with the wake vortices as discussed in Sec.3.3.4 (Fric and Roshko, 1994).

Toy et al. (1993) investigate the interaction of twin side-by-side and in-line JICF. The mixing region in the far-field is reported to be similar in shape but larger for twin JICF than for single JICF. This means especially that in the far-field of side-by-side jets there is only one CVP. The mechanism for the disappearance of the inner two vortices is unclear, as stated by Schlüter and Schönfeld (2000). Ibrahim and Gutmark (2006) study the penetration of such twin JICF by PIV. They demonstrate that the jet in the lee deflects less as compared to the jet in the wind.

3.3.2 Horseshoe Vortices

The horseshoe vortices have their front upstream of the jet. Their two branches have the form of a horseshoe if looked upon in the direction parallel to the jet axis. The horseshoe vortices result from the interaction between the jet and main flow boundary layer. As the fluid in the main flow boundary layer is deflected laterally away from the centerplane due to the adverse pressure gradient in front of the jet, the spanwise vorticity in the boundary layer is stretched to form the front of the horseshoe vortices, as Andreopoulos and Rodi (1984) argue. The vortices are convected and tilted such that the two branches compose the characteristic horseshoe shape. Kelso and Smits (1995) visualize the horseshoe vortices with hydrogen bubbles. They report a steady, an oscillating, and a coalescing regime of the horseshoe vortices. In the steady regime, the horseshoe vortices oscillate with the same Strouhal number as the jet shear layer roll-up but with a small amplitude. In the oscillating regime, the horseshoe vortices follow elliptical paths. The amplitude of these oscillations is not large enough that the vortices are engulfed in the jet. In the coalescing regime, the vortices are periodically generated

upstream, convect towards the jet and merge with their successor just before the jet. The bubble trails suggest that the horseshoe vortices enter the wake. Furthermore, an interaction with wake vortices seems likely as oscillations in the horseshoe vortices correspond to oscillations in the wake (see Sec.3.3.4).

3.3.3 Jet Shear Layer Vortices

In a free jet one can observe periodic roll-up of the mixing layer due to Kelvin-Helmholtz instability. As a free jet is axi-symmetric, one can imagine a succession of vortex rings. In a JICF, Kelvin-Helmholtz instability of such a character prevails at the upstream and downstream edges of the nozzle. At these locations spanwise rollers form which ride on top of the jet and hang below it. However, at the lateral edges the mixing layer is skewed. Hence a quasi-steady hanging vortex pair forms instead of periodic roll-up as Yuan, Street, and Ferziger (1999) point out. They also note that the upstream spanwise rollers roll up earlier due to the adverse pressure gradient in front of the jet, and then ride on top of the jet defining the upper boundary of the jet. The mixing layer downstream of the jet is more stable due to a favorable pressure gradient, and hence the roll-up of vortices is delayed. Kelso, Lim, and Perry (1996) identify a small separation bubble inside the nozzle at the upstream edge which oscillates up and down with the same Strouhal number as the jet shear layer roll-up. Haven and Kurosaka (1997) demonstrate using LIF and PIV that the presence of the horseshoe vortices affects the roll-up of the jet shear layer, consistent with the findings of Andreopoulos (1985).

3.3.4 Wake Vortices

Wake vortices are upright vortices which connect the bent jet and the main flow boundary layer. Fric and Roshko (1994) realize that the wake vortices are fundamentally different from wake vortices which form behind a solid obstacle, as vorticity cannot be generated in the flow field for incompressible fluids (see Sec.3.3). Therefore, all vorticity must originate from the boundaries or must have been in the flow initially. Smoke visualizations by Fric and Roshko (1994) suggest that wake vortices are composed of the main flow boundary layer fluid, not of jet fluid, at least in the regime they investigated. In their experiments wake vortices are observed to transport fluid from the boundary layer to the jet, much like a tornado. By this mechanism new vorticity is supplied to the CVP.

The above mentioned experiments and LIF by Smith and Mungal (1998) imply that the wake vortices form due to an interaction between the main flow boundary layer and the jet. Kelso et al. (1996) show with dye visualizations

that the main flow boundary layer separates downstream of the jet due to the adverse pressure gradient behind the jet. The upright wake vortices then appear during the separation events.

Yuan, Street, and Ferziger (1999) claim the origin of wake vortices to be an interaction between the horseshoe vortices and the vertical jet. In their computation, branches of the horseshoe vortices are lifted irregularly by the jet. The fact that the horseshoe vortices and the wake vortices oscillate with the same Strouhal number support this view, e.g. Kelso and Smits (1995), who visualize the flow field with hydrogen bubbles.

Various vortex shedding regimes exist: Unlike for vortex shedding behind a solid obstacle, the wake vortices do not need to have alternating vorticity. Kelso, Delo, and Smits (1993) observe a regime in which vortices are shed in pairs of opposite vorticity, giving rise to a mushroom-like flow structure if viewed upon in the direction of the nozzle axis. They perform flying hot wire measurements, dye visualization, and laser induced fluorescence (LIF) in a water tunnel, and smoke visualization in a wind tunnel. In the experiments of Fric and Roshko (1994), the wake vortices are strongest at a velocity ratio of around four; at a velocity ratio of two at the lower end and eight at the upper end the vortices become difficult to detect.

3.4 Non-Circular Jets in Crossflow

Free jets in quiescent atmosphere (no crossflow) can be passively controlled by changing the nozzle shape, for example the aspect ratio (AR) or the nozzle edges (Gutmark and Grinstein, 1999). This passive control is also possible for JICF. Non-circular nozzles always introduce smaller scale vortices into the flow compared to circular nozzles as they have locally higher curvature or even sharp nozzle edges. This enhances turbulent diffusion of momentum and passive scalars. The aspect ratio (AR) has been identified as a second parameter of importance (Haven and Kurosaka, 1997; Liscinsky, True, and Holdeman, 1996; Ibrahim, Murugappan, and Gutmark, 2005). It is defined as the ratio of spanwise (W) to streamwise (Q) dimensions ($AR = W/Q$). Elliptic nozzles with high AR have their minor axis aligned with the crossflow direction.

Liscinsky et al. (1996) compare circular, square, elliptic, and rectangular nozzles using Mie-scattering. They find that low AR nozzles form stronger CVPs. This is confirmed by Paper V. Haven and Kurosaka (1997) measure scalar mixing and visualize vortical structures in a water tunnel by LIF and PIV for elliptic and rectangular nozzles with high and low AR. They show evidence that for rectangular or elliptical nozzles additional vortices

with streamwise vorticity can appear. These ride on top of the CVP, are intermittent, and can spin clockwise or anti-clockwise on either side. If the orientation of their spin and the spin of the CVP are likewise, they are dubbed kidney vortex pair; if they rotate in the opposite sense, they are referred to as anti-kidney vortex pair. Unsteady kidney vortices appear for low AR nozzles whereas unsteady anti-kidney vortices for high AR nozzles.

As for trajectory data for circular nozzles, there is also inconsistent data regarding the nozzle shape: Haven and Kurosaka (1997) advocate a lower jet trajectory of their square nozzle compared to their circular nozzle whereas Liscinsky et al. (1996) claim the opposite.

The effect of nozzle shape on the trajectory, the flow field, coherent structures, and mixing is further discussed in Papers IV and V, Ibrahim et al. (2005), Liscinsky et al. (1996), and Haven and Kurosaka (1997).

3.5 Spray Jets in Crossflow

Spray JICF have applications in premixing tubes of LPP burners for gas turbines in which liquid fuel is injected into a crossflow of air. The fuel atomizes to small droplets and evaporates. The evaporated fuel and the air should be a homogeneous mixture in the flame region to avoid high emissions, unstable operation, and low efficiency (Madabhushi, 2003). The flow field of single-phase JICF is discussed in previous sections. It is argued in Paper VI that one can compare the flow fields of single- and multiphase JICF. There are corresponding coherent structures in both flow fields, and the continuous phase solution of multiphase JICF approaches the solution for single-phase JICF in the limit of small Stokes number (see Ch.4). These coherent structures have significant impacts on the secondary atomization of the spray. In the case of a spray JICF additional questions related to multiphase flow phenomena are raised. In Ch.4 some of the most relevant issues concerning flows with a dispersed phase are discussed: Droplet dispersion, collision, breakup, and evaporation. The interaction of the droplets and the flow is highly non-linear, and the mechanisms acting in the flow field of JICF are complicated further and not well understood. This section focuses on atomization and the immediate vicinity of the liquid JICF.

On top of the parameters which characterize a single-phase JICF (Sec.3.1), additional parameters are of interest. The *spray penetration* is defined here as the distance from the uppermost spray to the jet exit plane. The spray penetration is controlled by the momentum flux ratio. Schetz and Padhye (1977) solve momentum equations to estimate maximum penetration heights. Wu, Kirkendall, Fuller, and Nejad (1998) provide estimations for the spray pene-

tration, defined by the uppermost boarder of the spray plume (Eq.3.7), and for the locus of points with maximum spray volume flux in a cross-sectional plane (Eq.3.8):

$$\frac{y}{D} = 4.3J^{0.33}\left(\frac{x}{D}\right)^{0.33} \quad (3.7)$$

$$\frac{y}{D} = 0.51J^{0.63}\left(\frac{x}{D}\right)^{0.41} \quad (3.8)$$

In Paper III the spray penetration for various momentum flux ratios is computed in agreement with the measurements of Rachner, Becker, Hassa, and Doerr (2002) and Becker and Hassa (2002). The *spray width* is a measure for the lateral dispersion of the spray. Becker and Hassa (2002) claim the spray width to be nearly independent of the momentum flux ratio whereas Wu et al. (1998) conclude that the spray width grows with the momentum flux ratio.

Wu et al. (1998) measure droplet sizes, axial velocities, and volume fluxes in the far-field using phase-Doppler anemometry (PDA) for water spray JICF. Droplets disperse in layered regions such that large droplets tend to be in the uppermost layers and small droplet sizes in the lower layers. For small momentum flux ratios ($J = 9.5$), however, large droplets remain in the central region of the spray and small droplets disperse to the peripheral regions. PDA measurements indicate that the core region of the spray has the largest volume flux. The decay of volume flux around the core region is observed to qualitatively follow a normal distribution. The higher the momentum flux ratio, the smaller the largest measured volume flux becomes. The PDA volume flux measurements are estimated to be accurate to the order of magnitude only.

Rachner et al. (2002) and Becker and Hassa (2002) investigate a kerosene spray JICF experimentally using shadowgraphy, Mie-scattering, and PDA. The experiments are conducted at elevated pressure. The core region of the spray is measured to have the largest volume flux.

Fuller, Wu, Kirkendall, and Nejad (2000) apply shadowgraph photography on a water spray JICF. They vary the jet angle and show that the spray not only penetrates farthest but is also most dispersed and most uniform for injection at right angles. Lower angles result in denser spray cores with less dispersion. Leong, McDonell, and Samuelsen (2001) study spray boundaries of an atomized spray JICF at various ambient pressures and atomizing air pressures. They include the momentum flux of the atomizing air and correlate jet trajectories to the momentum flux ratio.

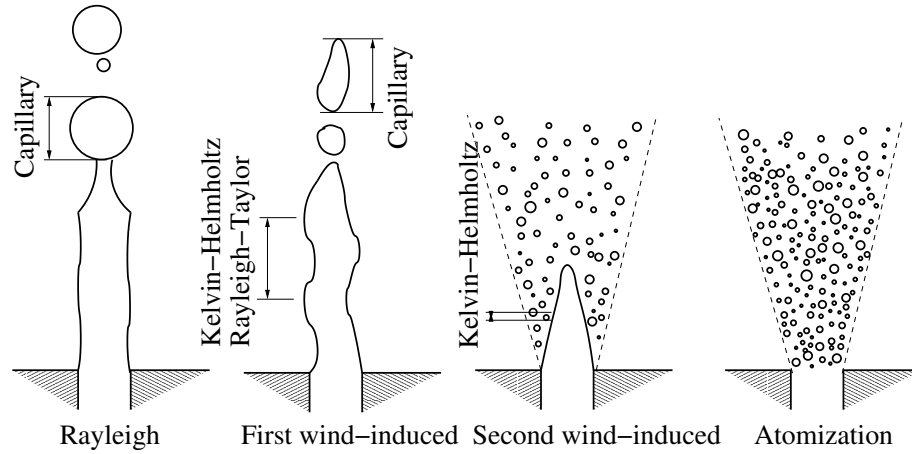


Figure 3.2: Breakup regimes of a liquid jet in quiescent atmosphere

Ghosh and Hunt (1998) model the near-field of spray JICF with simplified conservation equations. They point out that streamwise vorticity is generated at the interface between a liquid jet and a gas flow, unlike it is discussed for single-phase JICF (Sec.3.3). They distinguish a strong crossflow case, in which the ratio of induced air speed u_i and streamwise speed u_c is $u_i/u_c < 0.1$, and a weak crossflow case in which $u_i/u_c > 0.3$. In the weak crossflow case crossflow fluid is entrained close to the nozzle. If $u_i/u_c > 0.1$, a recirculation bubble downstream of the jet diminishes the probability for small droplets to leave the spray, and a pair of axial vortices is formed. In the strong crossflow case there is no entrainment but only a slow-down of the streamwise flow which transports small particles in the wake.

Caraeni, Bergström, and Fuchs (2000) study a spray jet in a gaseous crossflow with LES and a RANS-like approach with focus on nonlinear interactions among turbulence, temperature, and the dispersed phase. They investigate the far-field and the CVP. In their simulations, a better qualitative representation of the volume fraction field is obtained with a full LES computation compared to a RANS-like approach.

3.5.1 Breakup of Liquid Jets

A jet of liquid is inherently unstable and will break up into droplets in any case (Lin and Reitz, 1998). Four regimes of droplet breakup can be delineated: The *Rayleigh* regime, the *first* and *second wind-induced* regimes, and the *atomization* regime. These are sketched in Fig.3.2. Breakup is controlled by the relative importance of inertia, surface tension, viscous, and

gravity forces (Sirignano and Mehring, 2000). Dimensional analysis leads to three independent non-dimensional numbers, the Reynolds number, the Weber number We (Eq.3.9), and the Froude number Fr (Eq.3.10). The Weber number is the ratio of inertia and surface tension forces, the Froude number the ratio of inertia and gravity forces. One can form these numbers based on characteristic scales U and D and dynamic viscosity μ in the gas phase and the liquid phase. g is the acceleration due to gravity and σ the surface tension. If one more non-dimensional number, e.g. the density ratio of liquid and gas ρ_l/ρ_g , is specified, then the problem is completely determined by these seven numbers. Another non-dimensional group is the Ohnesorge number Oh which also accounts for viscosity (Eq.3.11).

$$We = \frac{\rho D U^2}{\sigma} \quad (3.9)$$

$$Fr = \frac{U^2}{gD} \quad (3.10)$$

$$Oh = \frac{\mu}{(\rho\sigma D)^{1/2}} = \frac{We^{1/2}}{Re} \quad (3.11)$$

If the Ohnesorge number is fixed, then the breakup regime is determined by the Weber number: In the Rayleigh regime the Weber numbers are smallest; for increasing Weber numbers one reaches the first and second wind-induced regimes, and finally the atomization regime. There are, however, Ohnesorge number effects. The atomization regime produces the smallest droplets of all regimes and is therefore desired for gas turbine applications. Jet breakup mechanisms are research topics, especially in the atomization regime where it is difficult to obtain experimental data due to the optically dense spray close to the nozzle exit.

It is shown by Rayleigh that a cylindrical jet has unstable axisymmetric modes for disturbance wavelengths which are larger than the jet circumference; the fastest growing disturbance has a wavelength of about nine times the radius. The *Rayleigh regime* therefore produces droplet sizes on the order of the nozzle diameter. In the Rayleigh regime the instability is inherent to the liquid jet (i.e. no air is required to trigger it) and is called *capillary instability*. The capillary instability is due to the action of van-der-Vaals forces which are attractive and drop rapidly with increasing distance between two molecules. Thus there is net attraction towards the more closely packed liquid phase, and therefore interfaces tend to contract (Batchelor, 1967). The interface of a liquid column does contract if the perturbation has a wavelength given by Rayleigh's criterion (Sirignano and Mehring, 2000). This leads to formation of spheres instead of a cylindrical column.

The first wind-induced regime is different from the Rayleigh regime due to gas inertia effects, due to which the jet is also unstable in non-axisymmetric modes. In this regime *Rayleigh-Taylor instability* and *Kelvin-Helmholtz instability* trigger the breakup of the jet, though the pinching itself is due to the capillary mechanism described above (Bachalo, Chigier, and Reitz, 1997). Rayleigh-Taylor instability occurs when a light fluid accelerates a heavy fluid normal to the surface. Such a disturbance leads to a misalignment of the pressure and density gradients. The more misaligned density and pressure gradients are, the smaller the acceleration of the liquid phase at that point is. This mechanism leads to growth of the disturbance. When gas inertia effects become more important, Kelvin-Helmholtz instability grows faster than Rayleigh-Taylor instability, and droplet sizes become much smaller than the nozzle diameter. Kelvin-Helmholtz instability wrinkles the droplet surface, if the local surface parallel velocities of the jet surface and the gas at the surface are unequal. A small disturbance leads to a pressure differential which amplifies the disturbance, until small droplets are sheared off the surface. A Kelvin-Helmholtz instability on a liquid jet implies that the length scales of the Kelvin-Helmholtz waves are much smaller than the jet diameter. Such sizes are formed in the second wind-induced regime. The jet is thought to be unstable to short wavelength disturbances. In the atomization regime the mechanism for jet breakup is still unclear.

Linear stability analysis can predict the onset, but not the development, of instability. It reveals effects of Weber, Reynolds, and Ohnesorge numbers (Lin and Reitz, 1998). The wavelength to which the jet is most unstable can be identified along with the initial growth rate of the disturbance. Increasing Weber number will yield the jet more unstable to disturbances of shorter wavelength. Moreover, their growth rate is larger. Increasing Ohnesorge number will increase the wavelength of the disturbance which growth fastest while its growth rate is reduced. The breakup length can well be predicted for the Rayleigh and first wind-induced regime using linear stability analysis. In the second wind-induced and atomization regimes, however, nonlinear effects are too strong. The breakup length can vary from directly at the nozzle to several diameters downstream depending on the nozzle design. Lin and Reitz (1998) suggest that cavitation or flow separation in the nozzle has significant effects on the breakup length. The observed instabilities in liquid jets can be *convective* or *absolute*. Convective instabilities grow in time while they are convected downstream. Such instabilities occur in the Rayleigh and the first and second wind-induced regime (Lin and Reitz, 1998). Absolute instabilities grow in space and time which means that they also propagate in upstream direction. This is the case under gas turbine conditions, and the atomization and droplet sizes can therefore vary in time due to feedback

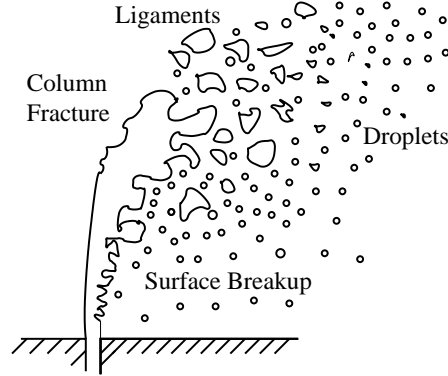


Figure 3.3: Liquid column breakup of a spray JICF (after Wu et al. (1997))

from the turbulent flow outside the nozzle.

The order of magnitude of droplet sizes in the various regimes can be estimated for all regimes but the atomization regime: It is simply proportional to the wavelength of the fastest growing instability, i.e. capillary, Rayleigh-Taylor, or Kelvin-Helmholtz. In the atomization regime, however, no instability mechanism is known, and hence one can give only crude estimates for the expected droplet sizes. An upper estimate for the droplet sizes is that in order of magnitude they are not larger than the nozzle diameter. On the low end of possible droplet sizes one can make the estimate that the surface tension energy of a droplet must be on the same order as the kinetic energy and assume some geometry of the droplet, e.g spherical. D_p is the droplet diameter, and u_{rel} the relative velocity of the the gas and the droplet.

$$E_{surface} \stackrel{!}{\sim} E_{kinetic} \quad (3.12)$$

$$\pi D_p^2 \sigma \sim \frac{1}{2} \frac{\pi}{6} D_p^3 \rho_d u_{rel}^2 \quad (3.13)$$

$$We = \frac{\rho D_p u_{rel}^2}{\sigma} \sim 12 \quad (3.14)$$

Changing the assumed geometry of the droplet just changes the numerical value 12. Thus one can see that the droplets on the low end of possible diameters are of such an order of magnitude that their Weber number is $We \sim 12$. This simplistic argument is also applied in droplet breakup models (Sec.4.2.5).

3.5.2 Breakup of Liquid Jets in Crossflow

Wu, Kirkendall, Fuller, and Nejad (1997) divide the breakup region into a

column region, a *big droplet* or *ligament region*, and a *spray region*. A breakup process of a spray JICF is sketched in Fig.3.3. In this view large droplets form in the column fracture region at the tip of the column and subsequently break up to smaller droplets. Simultaneously small droplets may be stripped off the surface. The breakup of the liquid jet in flows typical for gas turbine combustors may be thought to occur due to the *surface breakup mechanism* and the *column breakup mechanism* (Wu et al., 1997). The surface breakup mechanism is due to Kelvin-Helmholtz instability. Small droplets are stripped off the surface of the liquid jet due to aerodynamic shear. The column breakup mechanism refers to the growth of surface waves until the amplitude is so large that the jet fractures into ligaments and large droplets. The surface breakup mechanism is the dominant breakup mechanism at large momentum flux ratios and aerodynamic Weber numbers. Gas turbine combustors operate typically in this regime. The column breakup mechanism is dominant at low momentum flux ratios or low aerodynamic Weber numbers.

Fuller, Wu, Kirkendall, and Nejad (2000) vary the Mach number in the subsonic regime. High Mach numbers promote aerodynamic jet breakup whereas liquid JICF at low Mach numbers are observed to undergo column breakup. This is expected as high Mach numbers correlate with high aerodynamic Weber numbers. The overall penetration of the spray is suggested not to depend on the breakup mechanism but only on the momentum flux ratio.

Nguyen and Karagozian (1992) model the jet as a succession of elliptical slices in a potential flow for low Mach numbers and inviscid flow for higher Mach numbers. Madabhushi (2003) models liquid jet atomization taking into account the bending of the jet and the penetration of the jet before column fracture. The jet is modeled as droplets of nozzle size with a drag coefficient of a liquid jet as suggested by Wu et al. (1997). This drag coefficient is applied up to the fracture point of the liquid column. A wave model is applied to simulate droplet stripping from the jet. A water jet in subsonic air crossflow is simulated with a RANS turbulence model and compared to PDA data for various momentum flux ratios. Rachner et al. (2002) solve one-dimensional mass-, momentum-, and energy equations to obtain the jet trajectory while they model the deformation from the cylindrical shape empirically. They compute an aerodynamic breakup time scale at which a column breakup occurs. The arbitrarily chosen distribution of droplets inherits the jet velocity at this point. Before the jet fracture small droplets are stripped off the jet.

Chapter 4

Multiphase Flows with a Dispersed Phase

Matter is composed of molecules whose interactions determine whether the matter is in solid, liquid, or gaseous state. A *phase* contains matter in only one state, and is therefore a concept which requires a scale larger than the molecular scales. *Multiphase* flows are composed of more than one moving, distinct phases. This chapter is concerned with specific two-phase flows, i.e. dispersed particles in a continuous gas phase. A phase is defined to be *continuous* if a path between two arbitrary points in the phase can be found along which no phase change occurs. If such a line cannot be found for arbitrary points, a phase is said to be *dispersed*. The dispersed phase can further be subdivided into *monodisperse* (all dispersed particles have equal sizes) and *polydisperse* (they can have different sizes). A particle is here defined as any suspended phase in a continuum: It can be solid or liquid (as the continuum is gaseous). The liquid particles can also be called droplets, which in the present terminology implies that they can break up, coalesce, and evaporate. Droplet deformation and internal circulation are not taken into account.

A characteristic parameter for multiphase flow is the volume fraction of each phase. Suppose there is a material volume ΔV , in which the continuous phase occupies ΔV_c and the dispersed phase ΔV_d . Then the volume fractions of the dispersed phase and the continuous phase are given by Eq.4.1 and Eq.4.2, respectively.

$$\alpha_d = \frac{\Delta V_d}{\Delta V} \quad (4.1)$$

$$\alpha_c = \frac{\Delta V_c}{\Delta V} \quad (4.2)$$

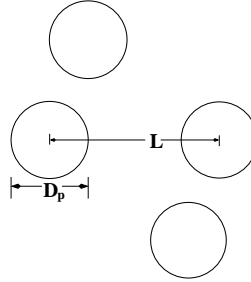


Figure 4.1: Particle spacing

The volume fractions α_d and α_c obviously add to one. For monodisperse, spherical particles the volume fraction is related to the mean particle spacing L/D_p by Eq.4.3 (Crowe, Sommerfeld, and Tsuji, 1998). The distance L and the particle diameter D_p are sketched in Fig.4.1.

$$\alpha_d = \frac{\pi D_p^3}{6L^3} \quad (4.3)$$

The momentum response time is a time scale which can be derived from Newton's law of motion (Eq.4.37). The momentum response time-scale τ_v describes the time which a particle needs to adjust to a change in flow velocity: After τ_v a particle has nearly reached 2/3 of a step change in constant free stream velocity in the vanishing Reynolds number limit. For a spherical particle the momentum response time is:

$$\tau_v = \frac{\rho_d}{\rho_c} \frac{D_p^2}{18\nu_c} \quad (4.4)$$

The momentum response time can be compared to typical flow time scales, e.g. a characteristic flow time scale τ_f . The Stokes number St is the ratio of these time scales:

$$St = \frac{\tau_v}{\tau_f} \quad (4.5)$$

If $St \gg 1$, the momentum response time is large as compared to the flow time-scale and the particle trajectory is marginally affected by the flow. If $St \ll 1$, the particle reacts quickly and follows the local fluid flow. The Stokes number is sensitive to the particle diameter, $St \sim D_p^2$ in the vanishing Reynolds number limit. As there is a wide range of scales in a turbulent flow, one can form various Stokes numbers, using representative scales in order to make comparisons. For example, one can base a Stokes numbers on the integral scales $St_0 = \frac{\tau_v}{\tau_0}$ or on the Kolmogorov scales $St_\eta = \frac{\tau_v}{\tau_\eta}$. It follows

from Eq.2.50 that these are related by:

$$St_\eta = St_0 Re_T^{1/2} \quad (4.6)$$

According to this scaling rule, the particles may follow large scales ($St_0 \ll 1$), but do not react quickly to small scales ($St_\eta \gg 1$) if the turbulence Reynolds number is large enough. One can conclude that LES is an especially efficient turbulence model under the above mentioned conditions since large scales are simulated whereas small scales modeled. Moreover, it has been shown in computations that particles disperse mainly due to large scales, e.g. Wang and Squires (1996) or Yeh and Lei (1981).

The characteristic time between particle collisions τ_c can also be compared to the momentum response time. If their ratio $\tau_v/\tau_c \gg 1$, the particle motion is highly affected by collisions. Such a flow is called *dense* dispersed flow. If on the other hand $\tau_v/\tau_c \ll 1$, the particles react to aerodynamic forces much faster than inter-particle collisions occur which implies that the flow is *dilute*.

4.1 Governing Equations for Two-phase Flows

The governing equations for multiphase flow are in principle known; they are simply the Navier-Stokes equation with matching boundary conditions at the interface between the liquid and the gas. They can be written in the following way (for low Mach number):

$$\frac{\partial \rho}{\partial t} + \frac{\partial \rho u_j}{\partial x_j} = \dot{m}_s \delta \quad (4.7)$$

$$\frac{\partial \rho u_i}{\partial t} + \frac{\partial \rho u_i u_j}{\partial x_j} = -\frac{\partial p}{\partial x_i} + \frac{1}{Re} \frac{\partial}{\partial x_j} (\mu^{(k)} (\frac{\partial u_i}{\partial x_j} + \frac{\partial u_j}{\partial x_i})) + \frac{\kappa n_i \delta}{We} \quad (4.8)$$

$\mu^{(k)}$ denotes the ratio of viscosity to the reference viscosity, i.e. it is unity for the phase for which the Reynolds number is defined. The interface in these equations is written as Dirac's delta function δ which is one at the interface and zero elsewhere. The mean curvature of the interface is represented by κ , and n_i is the unit normal to the interface (Panton, 2005). However, the number of grid points required to solve the Navier-Stokes equations for a spray consisting of several millions of droplets is many orders of magnitude too large for any current or foreseeable computer to handle. Thus further simplifications are introduced, leading to the Euler/Euler or the Euler/Lagrange approach.

4.1.1 Euler/Euler

In the Euler/Euler approach, changes of each phase are monitored at grid points. The equations are volume-averaged in a volume which is much larger than the mean spacing between the particles. This volume averaging (Sec.2.2.1) gives the following equations (Crowe, Sommerfeld, and Tsuji, 1998).

$$\frac{\partial \alpha_c \rho_c}{\partial t} + \frac{\partial \alpha_c \rho_c u_j}{\partial x_j} = \dot{m}_s \quad (4.9)$$

$$\frac{\partial \alpha_c \rho_c u_i}{\partial t} + \frac{\partial \alpha_c \rho_c u_i u_j}{\partial x_j} = -\alpha_c \frac{\partial p}{\partial x_i} + \frac{1}{Re} \alpha_c \frac{\partial^2 u_i}{\partial x_j^2} + \dot{F}_{s,i} \quad (4.10)$$

The interaction between the phases is reduced to the source terms $\dot{F}_{s,i}$ and \dot{m}_s which must be modeled. Corresponding equations can be written for the dispersed phase. As in the continuum assumption (see Sec.5.1), the volume-averaging ensures that the properties of each phase can be defined at any mathematical point. Both continuous and dispersed phase properties exist at the same point. The modeling of elementary processes (as evaporation or breakup) is more difficult in the two-continua formulation as the particles are not described on the level of an individual particle.

The present application includes breakup, collisions, and evaporation, and these processes depend on particle radii, temperatures, and distortion parameters (see Sec.4.2.5). The spray is then represented by ten variables, three spatial, three velocity, radius, temperature, distortion, and the derivative of the distortion. The discretization of a ten-dimensional equation is only feasible on extremely coarse grids in all ten dimensions, leading to excessive numerical diffusion.

4.1.2 Euler/Lagrange

The Eulerian/Lagrangian framework is selected in this thesis. Every particle of the dispersed phase is tracked in the Lagrangian framework, i.e. by integrating Newton's law of motion. Then the particle properties can be calculated individually, e.g. size, velocity, distortion etc. The main advantage of the Lagrangian description is that elementary processes as evaporation, breakup, or collision can be modeled on the level of an individual particle. A second advantage is that polydisperse spray particles of variable temperature and deformation parameters can be described with little extra effort.

In the Euler/Lagrange approach, one has two choices for the continuous phase equation: Either volume-averaged equations are written for the continuous phase, identical with Eq.4.9 and Eq.4.10, or one neglects the impact

of the dispersed phase on the continuous phase. Volume-averaged equations are appropriate for dense spray situations. However, if the averaging volumes have to be so large that relevant features of the continuous flow are averaged out, the volume averaging procedure is not applied, and the volume fraction of the particles is simply neglected. However, there are inherent inconsistencies in the Eulerian/Lagrangian description of multiphase flows with dispersed phases. One allows the two inconsistent notions that particles are regarded as mathematical points with no dimension, but also attributes a radius to them. Other inconsistencies concern the assumption that particles are spherical and the particles are isolated. These underlying premises of LPT are advanced to be inadequate for the spray JICF for a wide range of momentum ratios and particle sizes in Paper I.

Momentum, energy, and mass can be transferred between the phases: If such transfer is mutual, the phase coupling is referred to as *two-way coupling*. If the momentum transfer from the dispersed phase to the continuous phase can be neglected, the phase coupling is called *one-way coupling*. If in addition to the two-way coupling the particles do interact directly with each other, one talks about *four-way coupling* (Elghobashi, 1994). The interaction can be direct (contact) or indirect (aerodynamic). While collision models are readily available, remote particle interaction through aerodynamic effects has commonly been neglected. In Paper II this remote particle interaction is taken into account by modifying the drag coefficient according to relative positions of the particles, e.g. the drag force decreases substantially in the wake of a particle. The average computed drag force on particles decreases by as much as 40% in the near-field of the spray nozzle.

Continuous Phase

The non-dimensional continuity, momentum, energy, and mixture fraction transport equations for Newtonian fluids with constant diffusivities are described in Eulerian framework. The equations are valid for flow in the limit of low Mach number. The continuous phase volume fraction α_c is assumed to be unity (point particles).

$$\frac{\partial \rho}{\partial t} + \frac{\partial \rho u_j}{\partial x_j} = \dot{m}_s \quad (4.11)$$

$$\frac{\partial \rho u_i}{\partial t} + \frac{\partial \rho u_i u_j}{\partial x_j} = -\frac{\partial p}{\partial x_i} + \frac{1}{Re} \frac{\partial^2 u_i}{\partial x_j^2} + F_{s,i}^{\dot{}} \quad (4.12)$$

$$\frac{\partial \rho h}{\partial t} + \frac{\partial \rho u_j h}{\partial x_j} = \frac{1}{RePr} \frac{\partial^2 h}{\partial x_j^2} + \dot{Q}_s \quad (4.13)$$

$$\frac{\partial \rho Z}{\partial t} + \frac{\partial \rho u_j Z}{\partial x_j} = \frac{1}{ReSc} \frac{\partial^2 Z}{\partial x_j^2} + \dot{Z}_s \quad (4.14)$$

$\dot{m}_s, \dot{F}_{s,i}, \dot{Q}_s, \dot{Z}_s$ are source terms for mass, momentum, energy, and mixture fraction, respectively. The source terms account for the coupling from the liquid phase to the gas phase. The Schmidt number Sc is the ratio of momentum and mass diffusivities, the Prandtl number Pr the ratio of momentum and heat diffusivities.

$$Sc = \frac{\nu_c}{D_c} \quad (4.15)$$

$$Pr = \frac{\nu_c}{\alpha_c} \quad (4.16)$$

The equations are valid in the low Mach number limit, which in turn does not imply that the density is constant. It may very well change due to heat release or varying molecular composition. The system of equations is closed by an equation of state, the ideal gas law:

$$p = \rho RT \quad (4.17)$$

The ideal gas law can be simplified for low Mach number flows. The pressure can be decomposed into a reference pressure p_0 and a pressure change δp .

$$p_0 + \delta p = \rho RT \quad (4.18)$$

Eq.4.18 can be non-dimensionalized by the reference quantities p_0, ρ_0, R_0 , and T_0 . The correct scaling for the pressure change δp is $\rho_0 U_0^2$ in high Reynolds number flow. The non-dimensional quantities $\rho^*, T^*, R^*, \delta p^*$ are then all of order unity. Note that the specific gas constant is inversely proportional to the molecular mass. As evaporating fuel gases, e.g. heptane, can be 3-4 times as heavy as air, the density differences due to non-uniform mixture fraction can be significant (also by the same factor). Therefore the specific gas constant is not assumed constant in the present formulation. One can introduce the reference quantities into the ideal gas law:

$$p_0 + \rho_0 U_0^2 \delta p^* = \rho_0 R_0 T_0 \rho^* R^* T^* \quad (4.19)$$

Dividing by $\rho_0 R_0 T_0$ and introducing the Mach number $Ma_0 = \frac{U_0}{a_0}$ with $a_0 = \sqrt{\gamma R_0 T_0}$ gives:

$$1 + \gamma Ma_0^2 \delta p^* = \rho^* R^* T^* \quad (4.20)$$

In the limit of low Mach number the product $\rho^* R^* T^*$ is unity, therefore ρRT is constant and especially equal to $\rho_0 R_0 T_0 = p_0$. Thus, in the limit of low Mach number the equation of state becomes simply:

$$p_0 = \rho RT \quad (4.21)$$

The conclusion is that in the limit of low Mach number the density is inversely proportional to the temperature and the specific gas constant and the pressure may be regarded as constant in the equation of state. Acoustic waves propagate at a Mach number of unity. It is obvious that there can be no acoustic waves described by the low Mach number assumption. This has the advantage that acoustic waves do not have to be tracked in the computation.

Dispersed Phase

The dispersed phase is described by a PDF, or the corresponding particle distribution function f .

$$f(\vec{x}, \vec{v}, r, T, y, \dot{y}) d\vec{x} d\vec{v} dr dT dy d\dot{y} \quad (4.22)$$

The particle distribution function describes the number of particles per unit volume at a position between \vec{x} and $\vec{x} + d\vec{x}$ which have a velocity between \vec{v} and $\vec{v} + d\vec{v}$, a temperature between T and $T + dT$, and a radius between r and $r + dr$ with distortion parameters between y and $y + dy$ and \dot{y} and $\dot{y} + d\dot{y}$. The distortion parameters are discussed in Section 4.2.5. The spray equation (Eq.4.23) governs the change of the particle distribution function in all dependent variables, e.g. Kuo (1986).

$$\begin{aligned} & \frac{\partial f}{\partial t} + \frac{\partial(fv_j)}{\partial x_j} + \frac{\partial(fa_j)}{\partial v_j} + \frac{\partial(fr)}{\partial r} + \frac{\partial(f\dot{T})}{\partial T} + \frac{\partial(f\dot{y})}{\partial y} + \frac{\partial(f\ddot{y})}{\partial \dot{y}} \\ & = \dot{f}_{coll} + \dot{f}_{break} \end{aligned} \quad (4.23)$$

The liquid volume fraction α_d (Eq.4.24) can be redefined as a moment of the particle distribution function.

$$\alpha_d = \int f \frac{4}{3} \pi r^3 d\vec{v} dr dT dy d\dot{y} \quad (4.24)$$

The source terms for the continuous phase are given by the rates of change of mass, momentum, and energy of all particles in the incremental volume.

$$\dot{m}_s = -\frac{L}{\rho_c U} \int f \rho_d 4\pi r^2 \frac{dr}{dt} d\vec{v} dr dT dy d\dot{y} \quad (4.25)$$

$$\dot{F}_{s,i} = -\frac{L}{\rho_c U^2} \int f \rho_d \left(\frac{4}{3} \pi r^3 \frac{dv_i}{dt} + 4\pi r^2 \frac{dr}{dt} v_i \right) d\vec{v} dr dT dy dj \quad (4.26)$$

$$\dot{Q}_s = -\frac{L}{\rho_c U h_\infty} \int f \rho_d \left(4\pi r^2 \frac{dr}{dt} h_{latent} + \frac{4}{3} \pi r^3 c_p \frac{dT}{dt} \right) d\vec{v} dr dT dy dj \quad (4.27)$$

$$\dot{Z}_s = -\frac{L}{\rho_c U} \int f \rho_d 4\pi r^2 \frac{dr}{dt} d\vec{v} dr dT dy dj \quad (4.28)$$

4.2 Lagrangian Particle Tracking

4.2.1 Stochastic Parcel Method

If the number of particles is too large to permit individual treatment of particles efficiently, the stochastic parcel method may be applied (Dukowicz, 1980). A computational particle, a parcel, represents a group of particles with identical properties. The number of particles in a parcel is interpreted only in a statistical sense, and may be any real, positive number. Such a parcel is treated as if it would be an individual particle, and the submodels for particle transport, evaporation, collision, and breakup rely on this assumption. The sensitivity of the solution to the number of parcels is presented in Sec.4.3.4.

4.2.2 Particle Trajectories

The particle trajectories are calculated in Lagrangian framework. The instantaneous parcel positions \vec{x} are obtained by integration of the parcel velocities \vec{v} which in turn are obtained from integration of the parcel accelerations \vec{a} .

$$\vec{v} = \frac{d\vec{x}}{dt} \quad (4.29)$$

$$\vec{a} = \frac{d\vec{v}}{dt} \quad (4.30)$$

The instantaneous parcel accelerations are computed from Newton's law, assuming that the momentum flux due to evaporation is uniformly distributed over the particle surface. Newton's law is then

$$\vec{F} = m\vec{a} \quad (4.31)$$

The force \vec{F} can depend on all parameters in the Navier-Stokes equations: The particle diameter D_p , the relative velocity u_{rel} between particle and gas, the continuous phase density ρ_c , and the continuous phase kinematic

viscosity ν_c . Consider first steady, uniform flow around a single, rigid, spherical particle at very small Reynolds number (Stokes flow). The time terms and convective terms can be neglected in the Navier-Stokes equations. The density and the kinematic viscosity occur only as a product and can be combined to the dynamic viscosity $\mu_c = \rho_c \nu_c$. The force F on the sphere must be $F \sim \mu D u_{rel}$, i.e. proportional to the diameter D_p , the flow velocity u_{rel} and the dynamic viscosity μ as it is impossible to form other combinations that have the dimension of a force (Landau and Lifshitz, 1987). It follows directly that the drag coefficient is $C_d \sim \frac{1}{Re_p}$ if C_d is defined by Eq.4.32 and the particle Reynolds number Re_p by Eq.4.33.

$$C_d = \frac{F}{\frac{1}{8}\pi D_p^2 \rho_c u_{rel}^2} \quad (4.32)$$

$$Re_p = \frac{u_{rel} D_p}{\nu_c} \quad (4.33)$$

The constant of proportionality can also be given since Stokes found an exact solution for this flow:

$$F = 3\pi\mu D_p u_{rel} \quad (4.34)$$

$$C_d = \frac{24}{Re_p} \quad (4.35)$$

Now consider large Reynolds numbers, yet so low that the boundary layer remains laminar. The position of the flow separation is nearly independent of the Reynolds number (Landau and Lifshitz, 1987). Therefore the drag cannot depend on viscosity and it can be inferred by dimension that the force is proportional to $F \sim \rho u_{rel}^2 D_p^2$ and therefore $C_d = constant$. The value of the constant is likewise empirical. In the present simulation, C_d is correlated to the parcel Reynolds number as:

$$C_d = \begin{cases} \frac{24}{Re_p} (1 + \frac{1}{6} Re_p^{2/3}) & \text{for } Re_p \leq 1000 \\ 0.424 & \text{for } Re_p \geq 1000 \end{cases} \quad (4.36)$$

Traditionally, in spray simulations all terms except the aerodynamic forces are neglected: Gravitation, gas phase flow acceleration, added mass, the Basset history integral, Magnus, Saffman, and Faxen forces. Mach number effects are also neglected. The validity of several of these assumptions is discussed in Sec.4.2.3. The parcel accelerations are then:

$$\frac{d\vec{v}}{dt} = -\frac{3}{4} \frac{\rho_c}{\rho_d} \frac{1}{D_p} C_d |\vec{v} - \vec{u}| (\vec{v} - \vec{u}) \quad (4.37)$$

$|\vec{v} - \vec{u}|$ is the relative speed, \vec{v} and \vec{u} are velocity vectors of the parcels and the gas. Introducing the particle Reynolds number gives:

$$\frac{d\vec{v}}{dt} = -\frac{C_d Re_p}{24} 18 \frac{\rho_c}{\rho_d} \frac{\nu_c}{D_p^2} (\vec{v} - \vec{u}) \quad (4.38)$$

The first fraction will approach unity in the limit of low Stokes number (see Eq.4.35). A time scale inherent to Newton's law is $\tau_v = \frac{1}{18} \frac{\rho_d D_p^2}{\rho_c \nu_c}$. Eq.4.37 rests on the assumptions that the particles are isolated and spherical. These assumptions are evaluated in Paper I and it is established that they are violated in large portions of the flow field for the present application. Especially the 4-way coupling is shown to have considerable effects in Paper II.

4.2.3 Forces on a Particle

It is necessary to establish under which conditions it is a reasonable approximation to neglect all forces on the particle except the steady-state aerodynamic drag. The discussion starts with the Basset-Boussinesq-Oseen (BBO) equation as derived by Maxey and Riley (1983). The total drag force on the particle may be written as the sum of the Stokes drag F_{St} , the force due to fluid acceleration F_{fa} , the virtual mass force F_{vm} , the Basset history term F_{Bas} , gravity F_g (or buoyancy), and the sum of all Faxen corrections F_{Fax} .

$$\frac{\pi}{6} D_p^3 \rho_d \frac{dv}{dt} = -F_{in} = F_{St} + F_{fa} + F_{vm} + F_{Bas} + F_g + F_{Fax} \quad (4.39)$$

F_{in} is the inertial force after d'Alembert. His ansatz was to formulate Newton's law as a so-called dynamic equilibrium in analogy to a static equilibrium ($F_{in} + \sum F = 0$). The inertial force signifies the resistance of the particle against acceleration. One can then compare the forces that act on the particle with the inertial force to estimate how strong the effects of the forces are. The inertial force is proportional to the Lagrangian derivative $\frac{dv}{dt}$ following the particle according to Newton's law (but in the opposite direction of the acceleration). The estimates given below are for isolated, rigid, spherical particles. The force due to flow acceleration F_{fa} is dependent on the Lagrangian derivative following a fluid element near the particle $\frac{Du}{Dt}$ (Eq.4.41). The virtual mass force F_{vm} is the force due to the fact that acceleration of a particle requires acceleration of the surrounding fluid. This acceleration of the fluid requires work which is done by the particle on the flow. Hence the body has an apparently larger inertial mass which is called virtual mass. The virtual mass force is dependent on the Lagrangian derivatives following the particle $\frac{du}{dt}$ and $\frac{dv}{dt}$, or one could write $\frac{du_{rel}}{dt}$ (Eq.4.42). The Basset history

term accounts for the time delay in the development of the boundary layer (Eq.4.43). The second term in Eq.4.43 is due to an initial velocity difference and was derived by Maxey in 1993 (Sirignano, 1999).

$$F_{St} = 3\pi D_p \rho_c \nu_c u_{rel} \quad (4.40)$$

$$F_{fa} = \frac{\pi}{6} D_p^3 \rho_c \frac{Du}{Dt} \quad (4.41)$$

$$F_{vm} = \frac{\pi}{12} D_p^3 \rho_c \left(\frac{du}{dt} - \frac{dv}{dt} \right) \quad (4.42)$$

$$F_{Bas} = \frac{3}{2} D_p^2 \sqrt{\pi \rho_c \mu_c} \left(\int_0^t \frac{\frac{du}{dt} - \frac{dv}{dt}}{\sqrt{t-t'}} dt' + \frac{u-v_0}{\sqrt{t}} \right) \quad (4.43)$$

$$F_g = \frac{\pi}{6} D_p^3 (\rho_d - \rho_c) g \quad (4.44)$$

If the flow is nonuniform, the Faxen forces can be added as corrections to relative velocities in the Stokes drag and Basset history term ($\frac{D_p^2}{24} \nabla^2 u_{rel}$) and the virtual mass force ($\frac{D_p^2}{40} \nabla^2 u_{rel}$) (Sirignano, 1999). One can immediately see that the Faxen corrections are of order $o(\frac{D}{l})^2$ if l is the length scale of the flow non-uniformity. The Faxen corrections can be neglected if the particle size is much smaller than the size of the scale, in a turbulent flow the Kolmogorov scale. However, the Kolmogorov scales may be of the same size as the particle sizes, and hence neglecting the terms may not be justified. If high particle Reynolds number effects are included, the Stokes drag must be replaced by the empirical relation for the steady-state aerodynamic drag force F_{ss} .

$$F_{ss} = \frac{\pi}{8} C_D D_p^2 \rho_c u_{rel}^2 \quad (4.45)$$

It is necessary to estimate ratios of several Lagrangian derivatives. If flow non-uniformities are on a scale larger than the particle diameter (which was supposed to neglect the Faxen forces), the Lagrangian derivatives of the flow velocity following the particle and following a fluid element are of the same order, and the distinction between them can be dropped. The ratio of flow acceleration $\frac{du}{dt}$ and the particle acceleration $\frac{dv}{dt}$ can be estimated to be of the order of the Stokes number, assuming that the velocity scale is of the same order and the Stokes number is not too small. However, for small Stokes numbers, the particle acceleration will be of the same order as the flow acceleration, and therefore 1 is added to the Stokes number. The limiting behavior of the expression is sufficient in order to estimate the order of magnitude.

$$\frac{\frac{Du}{Dt}}{\frac{dv}{dt}} \sim \frac{\frac{du}{dt}}{\frac{dv}{dt}} \sim (St + 1) \quad (4.46)$$

Thus the ratio of the unsteady forces to the inertial force can be found (neglecting the numerical values of the constants):

$$\frac{F_{fa}}{F_{in}} \sim \frac{\rho_c \frac{Du}{Dt}}{\rho_d \frac{dv}{dt}} \sim \frac{\rho_c}{\rho_d} (St + 1) \quad (4.47)$$

$$\frac{F_{vm}}{F_{in}} \sim \frac{\rho_c}{\rho_d} \left(\frac{du}{dt} - 1 \right) \sim \frac{\rho_c}{\rho_d} St \quad (4.48)$$

$$\begin{aligned} \frac{F_B}{F_{in}} &\sim \sqrt{\frac{\rho_c^2 \nu_c}{\rho_d^2 D_p^2} \frac{du}{dt} - \frac{dv}{dt}} \tau_0 \sim \sqrt{\frac{\rho_c^2 \nu_c l_0}{\rho_d^2 D_p^2 u_0'} \left(\frac{du}{dt} - 1 \right)} \\ &\sim \frac{\rho_c}{\rho_d} \frac{l_0}{D_p} \sqrt{\frac{1}{Re_T}} St \sim \frac{\rho_c}{\rho_d} \frac{\lambda}{D_p} St \end{aligned} \quad (4.49)$$

The ratio of the force due to flow acceleration to the inertial force is on the order of the density ratio, if the Stokes number is not too large. The virtual mass force / inertial force ratio is on the order of the density ratio times the Stokes number. For the Basset history force it is further supposed that the boundary layer adapts to the unsteady flow in the time scale of the largest eddies. This implies that the memory effects are limited to a relatively short time in the past. The last estimate in Eq.4.49 shows that when the particle size is of the order of the Taylor micro-scale, the relative contribution of the Basset force is proportional to the density ratio times the Stokes number.

As discussed above, one can define various Stokes numbers for a turbulent flow, as there is a continuum of time scales. If one bases the Stokes number on the largest eddies, it seems justified to neglect the unsteady forces. At the smallest scales, however, this may not be justified.

Next, gravity and buoyancy are examined. It is easier to show that these forces are small compared to the steady-state aerodynamic forces, and this is also sufficient since the steady-state aerodynamic force is usually the largest contributor to the drag.

$$\frac{F_g}{F_{ss}} \sim \frac{\frac{\pi}{6} D_p^3 \rho_d g \left(1 - \frac{\rho_c}{\rho_d} \right)}{C_d \frac{\pi}{8} D_p^2 \rho_c u_{rel}^2} \sim \frac{1}{C_d} \left(\frac{\rho_d}{\rho_c} - 1 \right) \frac{g D_p}{u_{rel}^2} \quad (4.50)$$

$$\sim \frac{1}{C_d} \left(\frac{\rho_d}{\rho_c} - 1 \right) \frac{1}{Fr^2} \quad (4.51)$$

For bubble flow $\rho_d/\rho_c \ll 1$, meaning one can neglect the gravity force compared to Archimedes' principle. Contrarily, for particle in gas $\rho_d/\rho_c \gg 1$, implying one can neglect Archimedes' principle compared to the gravity force. If

the Froude number Fr is large, one may neglect gravity or buoyancy. Hence one has for particles in gas:

$$\frac{F_{gravity}}{F_{ss}} \sim \frac{1}{C_d} \frac{\rho_d}{\rho_c} \frac{1}{Fr^2} \quad (4.52)$$

and for bubbles in liquid:

$$\frac{F_{buoyancy}}{F_{ss}} \sim \frac{1}{C_d} \frac{1}{Fr^2} \quad (4.53)$$

4.2.4 Droplet Evaporation

To account for evaporation, mass (species) and energy balances have to be satisfied for each individual droplet (Amsden, O'Rourke, and Butler, 1989). In this thesis, only single-component droplets are investigated. The non-dimensional gradients of species and temperature at the droplet surface are the Sherwood number Sh and the Nusselt number Nu .

$$Sh = -\frac{D_p}{Y_{F,s} - Y_{F,\infty}} \left(\frac{dY_F}{dr} \right)_s \quad (4.54)$$

$$Nu = -\frac{D_p}{T_s - T_\infty} \left(\frac{dT}{dr} \right)_s \quad (4.55)$$

The evaporation is calculated considering single, spherical, mono-component droplets with homogeneous temperature and constant density. Recently models for treating multicomponent droplets have appeared (Sirignano, 1999; Torres, O'Rourke, and Amsden, 2003a,b). No gas is allowed to be solved in the droplets or condense. Neglecting forced convection, the problem is reduced to spherically symmetric Stephan convection. Species and energy balances can be integrated over a control volume from the droplet surface to a boundary far away. Species conservation gives the rate of change of the parcel radius.

$$\frac{dr}{dt} = -\frac{\rho_c D_g B_d}{\rho_d D_p} Sh \quad (4.56)$$

$$B_d = \frac{Y_F^s - Y_F^\infty}{1 - Y_F^s} \quad (4.57)$$

$$Sh = \left(2 + \frac{3}{5} Re_p^{1/2} Sc^{1/3} \right) \quad (4.58)$$

The mass transfer number B_d relates the fuel vapor mass fraction far away, Y_F^∞ , to the fuel vapor mass fraction at the surface, Y_F^s (Eq.4.57). Forced

convection is then taken into account by the empirical Ranz-Marshall correlation (Eq.4.58), due to which the increase in fluxes due to convection is modeled from the Reynolds number Re_p and the Schmidt number Sc . The properties are evaluated at the film temperature T_f which is calculated from the gas temperature T and the parcel temperature T_p :

$$T_f = \frac{T + 2T_p}{3} \quad (4.59)$$

The fuel mass fraction Y_F^s very close to the droplet surface is computed under an equilibrium assumption (the partial pressure of fuel vapor p_v is equal to the vapor pressure at the parcel temperature T_p). Under this assumption Raoult's law gives the fuel mass fraction.

$$Y_F^s = \frac{M_l}{M_l + M_g \left(\frac{p}{p_v} - 1 \right)} \quad (4.60)$$

An energy balance for the droplet gives the change in droplet temperature: The change in temperature can be computed from the convective heating of the droplet and the latent heat. The temperature is assumed to be continuous over the interface.

$$\frac{\pi}{6} D_p^3 \rho_d c_{liq} \frac{dT_p}{dt} - \pi D_p^2 \rho_d \frac{dr}{dt} h_{latent} = \pi D_p^2 Q \quad (4.61)$$

Similarly to the convective mass flux, the convective heat flux Q is computed analog to species conservation according to Eq.4.62 and Eq.4.63. In these equations, the thermal diffusivity is represented by $\alpha_{T,c}$, and Nu is the Nusselt number which can be related to the Reynolds and the Prandtl numbers analog to the Sherwood number for mass transfer.

$$Q = \frac{\alpha_{T,c}(T - T_p)}{2r} Nu \quad (4.62)$$

$$Nu = \left(2 + \frac{3}{5} Re_p^{1/2} Pr^{1/3} \right) \quad (4.63)$$

4.2.5 Droplet Breakup

Neglecting gravity, the shape of a droplet is determined by two forces: Surface tension and aerodynamic forces. Surface tension acts to minimize the surface-to-volume ratio and tends to restore a spherical shape whereas aerodynamic forces act in order to disturb the droplets from spherical shape. Their ratio, the Weber number We , is therefore a characteristic parameter

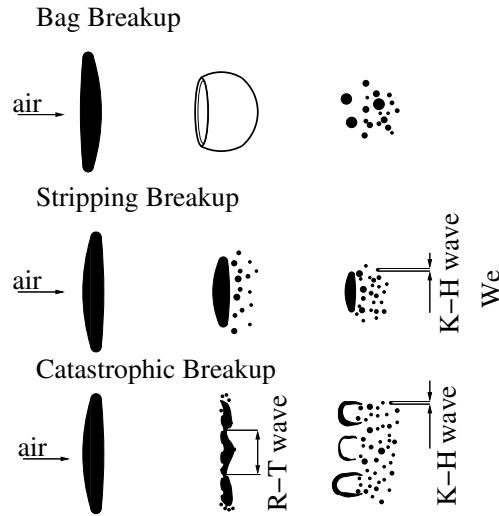


Figure 4.2: Droplet breakup regimes (after Tanner (2004))

for droplet breakup. Droplets can break up if they are unstable. Three important regimes for droplet breakup are bag breakup, stripping breakup, and catastrophic breakup. In the bag breakup regime, the droplet is distorted and breaks up due to oscillations; in the stripping breakup regime, small droplets are stripped off the parent droplets; and in the catastrophic breakup regime, the droplet is distorted and shatters. The breakup processes in these three regimes are sketched in Fig.4.2. The breakup regimes are in principle due to the same instabilities as were explained in Sec.3.5.1: Kelvin-Helmholtz instability or Rayleigh-Taylor instability. The newly formed droplets have sizes on the order of the wavelength of the instability which generated them, as pictured in Fig.4.2.

Droplet breakup is modeled using either the Taylor analogy breakup (TAB) model (O'Rourke and Amsden, 1987) or the breakup model by Reitz (Reitz and Diwakar, 1986, 1987). Alternatively, the following combination may be chosen (Caraeni, Bergström, and Fuchs, 2000): Droplets with more than 95% of the injected mass are modeled to break up according to Reitz, droplets with less than 95% of the injected mass after Taylor's analogy. Droplet breakup models rely on the stochastic parcel method: Since the number of droplets grows with the cube of the ratio of the droplet diameters before and after breakup, the number of droplets quickly becomes prohibitive for individual treatment. The number of parcels remains constant over the breakup process, but the number of droplets in the parcels changes.

Wave Breakup Model (Reitz)

The wave breakup model is after Reitz and Diwakar (1986) or Reitz and Diwakar (1987).

Bag Breakup

If the droplets in a parcel break up due to bag breakup ($We > 12$, as explained in Sec.3.5.1), the droplet size in the parcel is adjusted to a smaller, stable size. The time in which the droplets in a parcel satisfy the breakup criterion, i.e. they are unstable, is accumulated. The life time t_{bag} of an unstable droplet is:

$$t_{bag} = C_{bag} \sqrt{\frac{\rho_d D^3}{8\sigma_s}} \quad (4.64)$$

C_{bag} is a free parameter and set to $\pi/\sqrt{2}$ (Bergström, 1999). If the accumulated time in which the parcel is unstable is larger than the droplet life time, the droplets in the parcel break up. The droplet diameter after breakup D_{stable} can be derived from the breakup criterion:

$$D_{stable} = \frac{12\sigma_s}{\rho_c U_{rel}^2} \quad (4.65)$$

Mass conservation is applied to obtain the new number of droplets f in the parcel after breakup.

$$(fD^3)_{before} = (fD^3)_{after} \quad (4.66)$$

Conservation of total energy is required to find the new parcel velocity magnitude.

$$(f\frac{1}{2}mU_{rel}^2 + f\pi D^2\sigma_s)_{before} = (f\frac{1}{2}mU_{rel}^2 + f\pi D^2\sigma_s)_{after} \quad (4.67)$$

Thus one can see that the breakup model suggested by Reitz and Diwakar (1986) decreases the velocity of the parcel. However, the momentum is conserved for every parcel breakup, as the difference in momentum is transferred to the continuous phase.

Stripping Breakup

If the criterion for stripping breakup ($We > \sqrt{Re_p}$) is satisfied, the droplets in a parcel are unstable and break up by stripping small droplets off their surfaces. From the stripping criterion the stable droplet diameter D_{stable} can be computed.

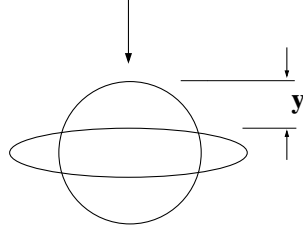


Figure 4.3: Droplet distortion (after Bergström (1999))

$$D_{stable} = \frac{\sigma_s^2}{\rho_c^2 U_{rel}^3 \nu} \quad (4.68)$$

The life time t_{str} of an unstable droplet is the time after which the droplet has reached the stable radius:

$$t_{str} = C_s \frac{D}{2U_{rel}} \sqrt{\frac{\rho_d}{\rho_c}} \quad (4.69)$$

C_s is a free parameter which is proportional to the life time of a stripping droplet. Several values for the free parameter C_s have been used which are summarized in Bergström (1999): Reitz and Diwakar set $C_s = 20$, Patterson et al. $C_s = 30$, and Nicholls $C_s = 8$. In this thesis, $C_s = 20$ is assumed. The change in size of the droplet due to stripping is then given by:

$$\frac{dD}{dt} = -\frac{D - D_{stable}}{t_{str}} \quad (4.70)$$

New parcels are created if the stripped mass is more than 1/10 of the injected parcel mass. Mass conservation requires that the mass of the stripped small droplets is equal to the change in mass of the parent droplets. The velocity of the stripped droplets is obtained by conservation of total energy. The droplet size is given by the stability criteria.

Taylor Analogy Breakup Model

Bag breakup can be modeled using the Taylor analogy breakup (TAB) model (O'Rourke and Amsden, 1987). A distortion equation is derived in analogy to an oscillating spring-mass system.

$$m\ddot{x} + d\dot{x} + kx = F \quad (4.71)$$

F is an external force on a mass m which is attached to a spring with spring constant k and damping constant d . The disturbing force on the spring is

analog to the aerodynamic forces acting on the droplets, the liquid viscosity provides the damping, and the surface tension, analog to a spring, acts to restore a spherical shape. The distortion parameter y is analog to the distortion of a strained spring, as Fig.4.3 illustrates. The distortion parameter y is scaled by $y = x/(C_b r)$.

$$\frac{F}{m} = C_F \frac{\rho_c u_{rel}^2}{\rho_d r} \quad (4.72)$$

$$\frac{k}{m} = C_k \frac{\sigma}{\rho_d r^3} \quad (4.73)$$

$$\frac{d}{m} = C_d \frac{\mu_l}{\rho_d r^2} \quad (4.74)$$

Then the distortion equation is obtained:

$$\ddot{y} + C_d \frac{\mu_l}{\rho_d r^2} \dot{y} + C_k \frac{\sigma}{\rho_d r^3} y = \frac{C_F}{C_b} \frac{\rho_c}{\rho_d} \frac{u_{rel}^2}{r} \quad (4.75)$$

The solution to the differential equation for the distortion parameter y is:

$$\begin{aligned} y(t) &= \frac{C_F}{C_k C_b} We + e^{-t/t_d} \left((y(0) - \frac{C_F}{C_k C_b} We) \cos \omega t \right. \\ &\quad \left. + \frac{1}{\omega} (\dot{y}(0) + \frac{(y(0) - \frac{C_F}{C_k C_b} We)}{t_d}) \sin \omega t \right) \end{aligned} \quad (4.76)$$

$$\frac{1}{t_d} = C_d \frac{\mu_l}{2 \rho_d r^2} \quad (4.77)$$

$$\omega^2 = C_k \frac{\sigma}{\rho_d r^3} - \frac{1}{t_d^2} \quad (4.78)$$

$C_F = \frac{5}{24}$, $C_k = 8$, $C_d = 10$, and $C_b = \frac{1}{2}$ are non-dimensional free parameters cited in Caraeni et al. (2000). Breakup occurs if $y(t) > 1$. As in the bag breakup model due to Reitz, the Weber number of the newly formed droplets is $We = 12$. Mass and energy conservation are applied as in the bag breakup model by Reitz.

4.2.6 Droplet Collision

Droplet collisions control the spray propagation in dense spray regions in which the collision time scales are smaller than the momentum relaxation

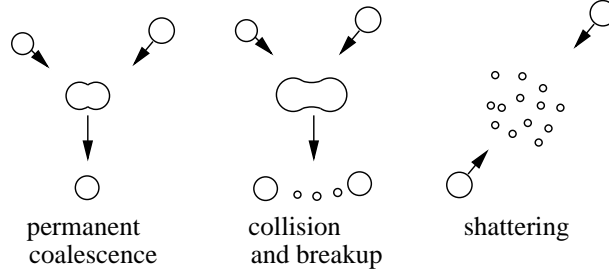


Figure 4.4: Droplet collision regimes (after Bergström (1999))

times. Droplet collision models have employed direct simulation of the collision (Amsden, O'Rourke, and Butler, 1989) or stochastic techniques which create virtual collision partners based on the local properties of the flow (Sommerfeld, 2001). The former approach becomes inefficient for large particle numbers, as one needs to investigate possible collisions between each pair of droplets. The computational effort for this scales with the square of the number of parcels. The present droplet collision model is described in Bergström (1999) or Amsden, O'Rourke, and Butler (1989).

Depending on the ratio of surface tension and excess inertia, the droplets are thought to coalesce, bounce, or shatter to various sizes. This is sketched in Fig.4.4. The outcome is dependent on the ratio of inertia forces to surface tension forces, from which a collision Weber number can be formed. The index "small" denotes the smaller of the two droplets, "large" the larger one.

$$We_{col} = \frac{\rho_d D_{p,small} (v_{small} - v_{large})^2}{\sigma} \quad (4.79)$$

At small collision Weber numbers the droplets coalesce, at larger droplet Weber number they bounce elastically, and at very large collision Weber number the droplets shatter. Shattering is not taken into account in the present collision model. For more complete description see Bergström (1999) or Amsden, O'Rourke, and Butler (1989).

4.3 Parameter Sensitivity Regarding JICF

The spray JICF is computed for a geometry sketched in Fig.4.5. The channel has no-slip conditions at top and bottom walls and periodic conditions at the lateral walls. The channel is divided into two sequential channel halves: The first half has flux conservative periodic conditions. The second half has outflow from the first channel as inlet condition and flux conservative zero

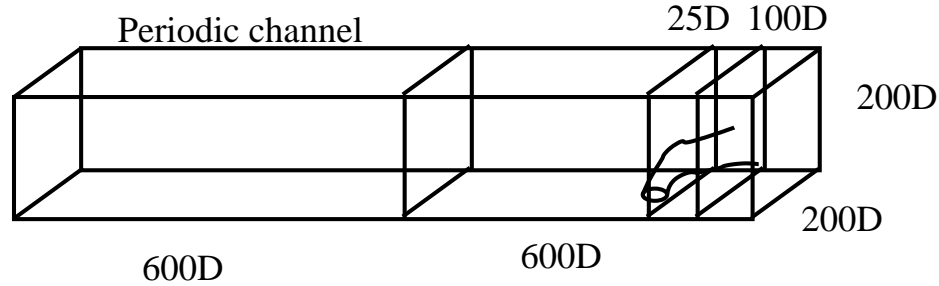


Figure 4.5: Channel geometry

Spray			
Fuel	<i>Octane</i>	Injection velocity	$75m/s$
SMD	$500\mu m$	Density	$860kg/m^3$
Temperature	$298K$	Surface tension	$0.022N/m$
Fuel mass flow	$12.4g/s$	Cone angle	$14deg$
Gas			
Velocity	$55m/s$	Density	$8.6kg/m^3$
Temperature	$600K$	Re	10000

Figure 4.6: Spray and gas parameters

gradient conditions at the outlet plane. The spray is injected in the second channel 200 nozzle diameter from the outlet. Data is sampled on lines in the plane of symmetry downstream of the nozzle at a distance of 25 nozzle diameters and 100 nozzle diameters. As the ratio of nozzle diameter and channel width is 200, it is impossible to resolve the nozzle. The nozzle diameter is roughly one third of the cell size on the finest grid. The momentum flux ratio is $J = 185$. In Fig.4.6 other physical parameters for spray and gas are summarized. This case was compared to experimental data in Bergström (1999) with satisfactory agreement between numerical and experimental results.

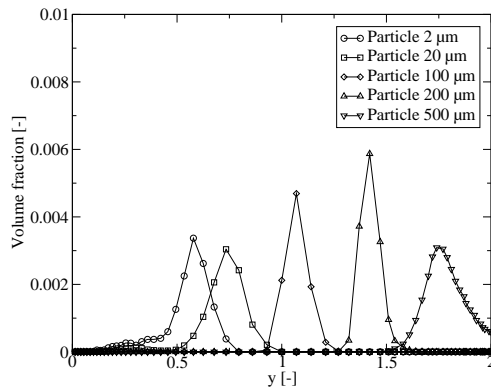
4.3.1 Initial Droplet Size and Its Distribution

The droplet size near the nozzle (as in any dense spray region) is difficult to measure since the region is optically dense. Furthermore, it is not clear whether there is a liquid core in the atomization regime which in turn depends on the injection procedure and the flow (with possible cavitation) in the nozzle. Additionally, droplet sizes may vary in time. Liquid jet breakup is therefore an active research topic. In this thesis the liquid jet is modeled by assuming droplets which are of sizes on the order of the nozzle diameter. Moreover, the injection droplet size distribution also has to be assumed.

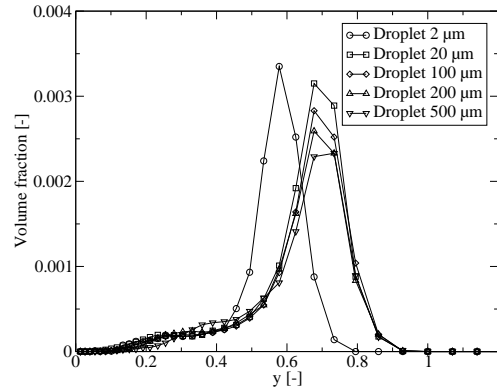
The sensitivity of the computed results to the droplet diameter is due to the large uncertainties of utmost importance. The uncertainty due to the assumed droplet size is often the limiting parameter in the certainty of the computed results as these may vary significantly with the assumed injection diameters. Even though the droplet size appears to be a physical parameter, it is better to regard it as a modeling parameter.

To elaborate on the effect of droplet breakup and evaporation, the solutions are compared to the solution for solid (non-atomizing) particles. Fig.4.7 compares dispersed phase volume fractions and streamwise and cross-stream velocities between particles on the right hand side and droplets on the left hand side for injection sizes ranging from $2\mu m$ to $500\mu m$. Fig.4.7a) shows that larger particles follow higher trajectories. Whereas the aerodynamic forces scale as the particle surface area, the inertial forces scale as the particle volume. The volume-to-surface ratio increases with increasing size, and therefore the aerodynamic force per unit mass decreases. This is a typical example of the elephant effect, which refers to the impossibility to arbitrarily scale physical bodies without changing their properties, as some effects scale with an area (drag, heat transfer, material strength) and others with a volume (mass, heat production, weight). The Stokes number is a non-dimensional parameter to study this effect: If the Stokes number is small, the momentum exchange between the particles and the flow is large. Due to their small momentum transfer the flow is widely undisturbed by large particles as is revealed in Fig.4.7c) and Fig.4.7e). The situation is more complex if droplets are injected instead. These also break up and evaporate, so that the average Stokes numbers drop along the trajectory (Paper I). If droplets are large, they break up to small droplets. The stable droplet sizes are the same in all cases. Therefore all curves lie closer to each other in the droplet case (Fig.4.7): The elephant effect is much less pronounced. If the Weber number of the given case were smaller, the elephant effect would be more pronounced than in Fig.4.7.

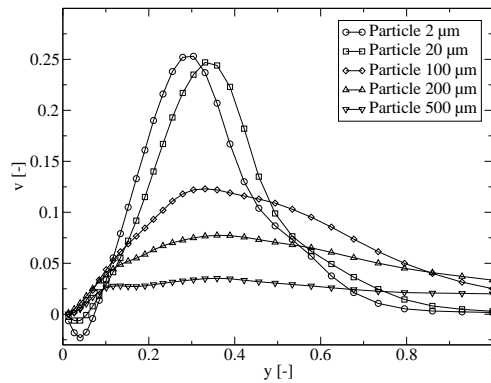
Figs.4.7c and 4.7d demonstrate that the vortex curve of the CVP (the locus of maximum upwash in the centerplane) is located at a higher distance (above the jet nozzle plane) with increasing injection droplet size. For larger droplets the momentum injection into the gas phase is delayed along the trajectory as momentum transfer is less efficient for larger droplets. The large droplets first have to break up before they dispose of their excess momentum at large rates. The delay of momentum transfer along the droplet trajectories is therefore the reason of the higher trajectory of the CVP. A comparison between droplets and particles up to $20\mu m$ reveals that they behave similarly as long as their Stokes numbers are similar. The difference between particles and droplets becomes more pronounced with increasing size as the droplets



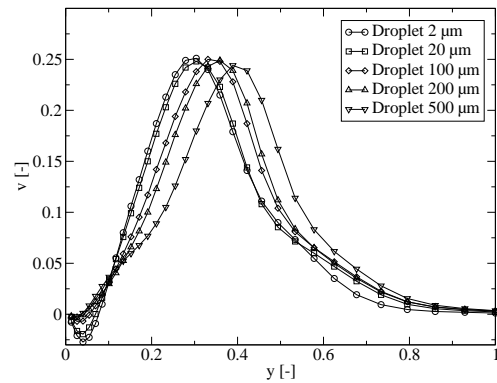
a) Volume fraction profiles for various particle injection diameters



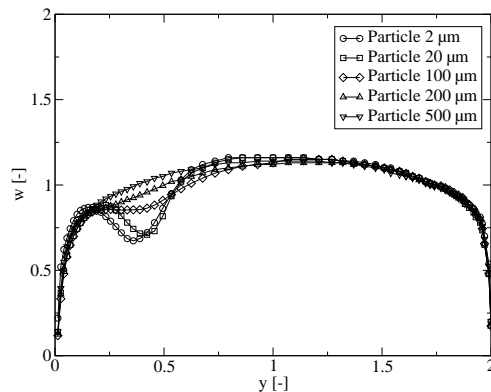
b) Volume fraction profiles for various droplet diameters



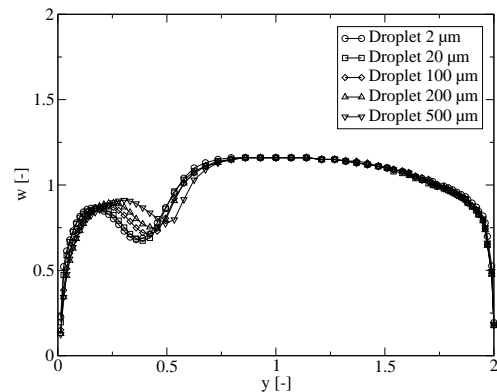
c) Cross-stream flow profiles for various particle injection diameters



d) Cross-stream flow profiles for various droplet diameters



e) Streamwise flow profiles for various particle injection diameters



f) Streamwise flow profiles for various droplet diameters

Figure 4.7: v and w velocity and liquid volume fraction profiles for various droplet injection diameters and solid particle diameters 100 diameters downstream

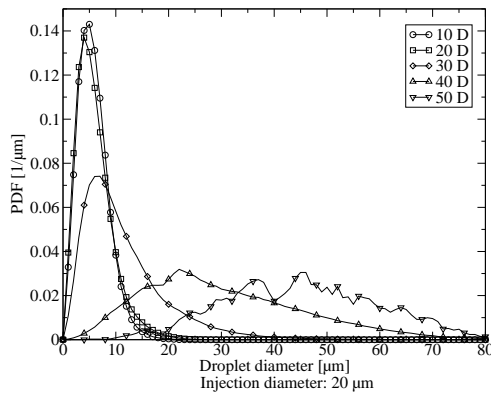
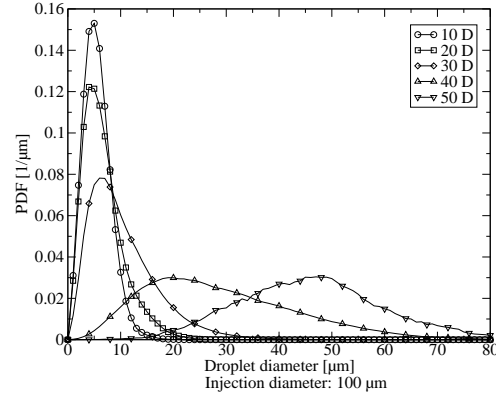
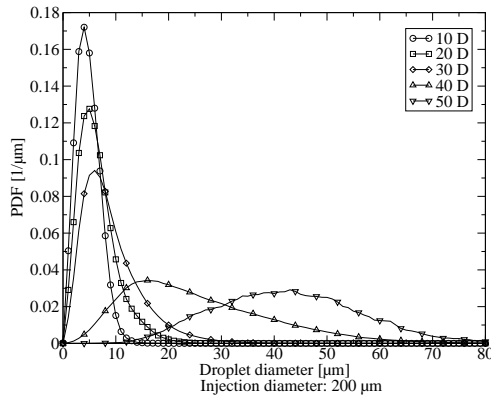
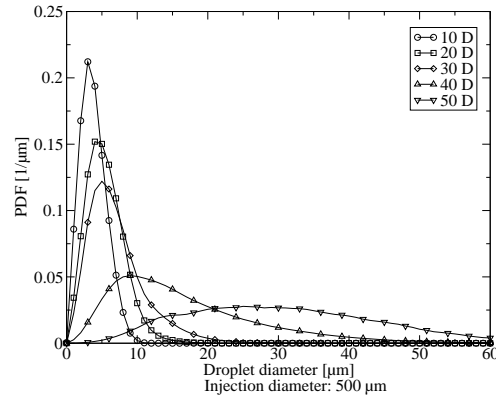
a) Sauter mean diameter 20 μm b) Sauter mean diameter 100 μm c) Sauter mean diameter 200 μm d) Sauter mean diameter 500 μm

Figure 4.8: Droplet size distributions at various heights 25 diameters downstream for various injection Sauter mean diameters

break up and thus have smaller Stokes numbers.

Fig.4.8 shows the effect of the injection droplet diameter on the droplet size distribution $25D$ downstream for SMD in the range $20 - 500 \mu m$. The curves in each graph are PDFs at five different heights above the wall (10D, 20D, 30D, 40D, 50D). The higher the location above the injection plane the larger the droplets become: The PDFs are shifted to the larger droplet sizes. This is explained again by the elephant effect. The larger droplet injection diameter promotes faster breakup of droplets as their Weber numbers are larger. This results in distributions with smaller droplet sizes for the largest injection SMD= $500 \mu m$. Furthermore, the peak probability densities of the curves increase, as the area under each curve is unity and the curves look similar. As the curves are compressed to the left for larger injection SMD, they expand upwards due to the equal area condition.

4.3.2 Injection Droplet Velocity Fluctuation

The droplet injection velocity fluctuation is, like the injection droplet diameters, a parameter which is difficult to estimate since no accurate measurements are available. Any assumed value including zero is questionable. The parameter sensitivity to the RMS of the injection velocity is therefore estimated in a wide range from zero to one hundred percent in Fig.4.9. The droplet size distributions close to the wall are sensitive to the velocity fluctuations if the latter are larger than 0.5 (Fig.4.9a). For large velocity fluctuation, large droplets can penetrate the region close to the wall if they have small velocities in jet direction. The peak in probability density for small droplets decreases due to this presence of larger droplets.

4.3.3 Flow Reynolds Number

The computed solution is not sensitive to the Reynolds number of the main flow as Fig.4.10 shows. The grid spacing is the same for all computed cases. As y^+ is proportional to the square root of the Reynolds number, the resolution near the wall deteriorates for increasing Reynolds number with fixed grid. However, as usual in LES, the resolution is in practice determined by the computational resources. As the resolution at the largest Reynolds numbers is less reliable (due to the lack of handling near wall effects) the results for the high Reynolds numbers, in Fig.4.10 should be interpreted as an indicator for the Re effects. In this respect, it is implied that the solution is not sensitive to the flow Reynolds number.

4.3.4 Number of Parcels

Similarly as in the question of grid accuracy, it has to be established that the number of computational parcels is sufficient. Fig.4.3.4a shows the liquid volume fraction along a line 25 jet diameters downstream of the nozzle along with the PDFs of particle sizes. The spray in the whole computational domain is represented by 4500, 11000, 28000, and 54000 parcels. There is no striking difference between the solutions if more than 11000 computational parcels are in the domain. Fig.4.3.4b shows the PDFs of the droplet sizes at four different heights above the wall (10D, 20D, 30D, 40D) as in Fig.4.8d). The droplet size distribution is represented with no large errors if more than 11000 parcels are used.

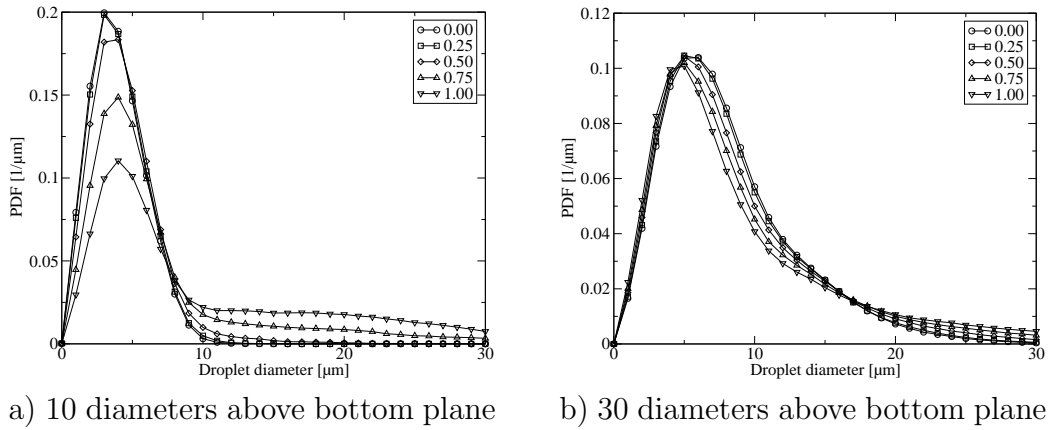


Figure 4.9: Droplet size distributions at various heights 25 diameters downstream for various droplet injection velocity fluctuations

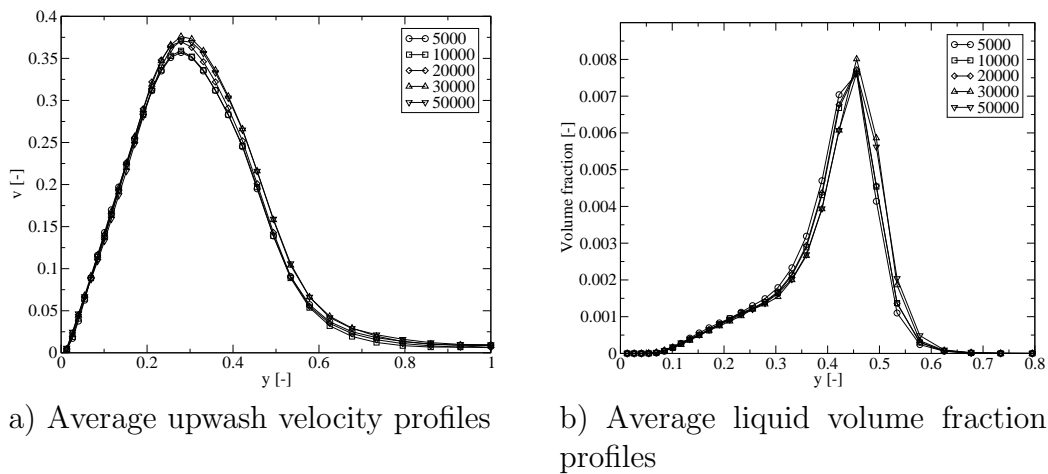


Figure 4.10: Average profiles along vertical centerline for various flow Reynolds numbers (5000-50000) 25 diameters downstream

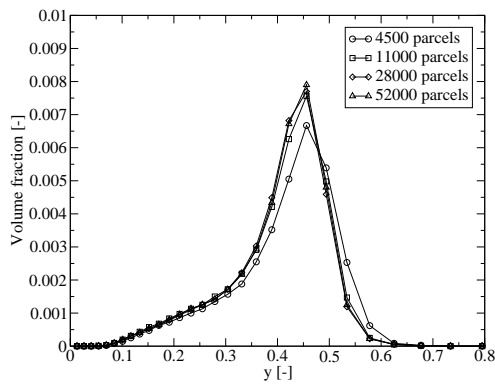


Figure 4.11: Volume fraction profiles for various average parcel numbers at $z/D = 25$ in the centerplane

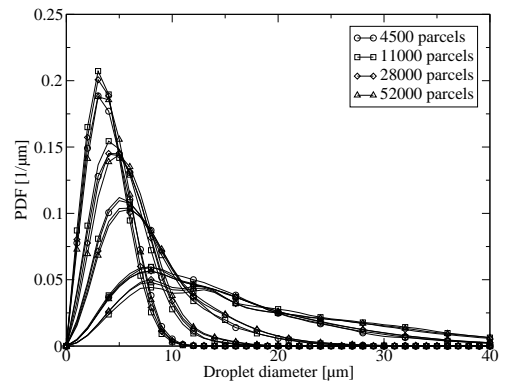


Figure 4.12: Droplet size distributions for various average parcel numbers at $z/D = 25$ in the centerplane

Chapter 5

Numerical Methods

5.1 Computational Fluid Dynamics

Flows are governed by the Navier-Stokes equations which consist of a system of non-linear partial differential equations (PDEs), representing the conservation of mass, momentum and energy. Analytic solutions are available for special cases with simplifying assumptions only, as for example for boundary layer flows or some laminar, creeping flows. Contrarily, numeric solutions can be computed to any well-posed problem. Using finite difference techniques, the PDEs are approximated by algebraic equations. This discretization results in a systematic error which is called the *discretization error*. It depends on purely numerical parameters, e.g. the grid spacing or time step size. The discretization error is the main focus of this chapter. Third-order upwind schemes, a fifth-order weighted essentially non-oscillatory (WENO) scheme, and an optimized second-order scheme are investigated as alternative discretization schemes. Further, boundary treatment and other features of the solver are discussed.

There are other systematic errors in the results of CFD calculations with which the discretization error must be compared (Ferziger and Peric, 2002). The *modeling errors* are the errors one makes when the governing equations are tailored to the flow case of interest. Modeling errors are introduced by the continuum assumption, the low Mach number assumption, the assumption of Newtonian fluids, the various spray submodels, and turbulence modeling among others. The error which arises because the algebraic equations are only solved approximately is called *iteration errors*. If the equations contain random variables (Pope, 2000), one seeks expectations of the variables, and these are only computed within *statistical errors* (Sec.2.2.1). To make a prediction about a real flow in a real geometry, one must keep all these

errors in check. Ideally, the sensitivity of the computed solution to changes in numerical and modeling parameters should be small compared to the sensitivity to physical parameters. This makes the sensitivity analysis to all of these parameters often more important than the solution itself. It is easy to control the statistical errors and the iteration errors below any value one can specify (above machine accuracy). Therefore, in this thesis only sensitivities to modeling and numerical errors are presented along with the solutions.

5.2 Discretization

The spatial discretization is done on a structured, stretched, and staggered grid which is depicted in Fig.5.1. The stretched grid is chosen to have higher resolution near the walls. Compared to unstructured grids, discretization schemes can be applied with ease on structured grids. For a staggered grid, velocities are stored at the cell face centers whereas scalars are stored at the cell volume centers. Due to grid staggering there is no odd-even decoupling of the pressure field. On the other hand, grid staggering necessitates the use of interpolation schemes. The spatial discretization is a major item for LES. Therefore, it will be described in more detail in Sec.5.2.1 to 5.2.3 in which the following schemes are discussed: WENO schemes, optimized schemes, and standard upwind schemes. A comparison between these schemes in terms of accuracy, efficiency, and resolution properties is made in Sec.5.2.4. The temporal discretization of the momentum equations is done with a third-order accurate Runge-Kutta scheme. The mixture fraction transport equation is discretized with a fourth-order accurate Runge-Kutta scheme. The diffusive terms are discretized with a fourth-order central finite difference scheme.

$$(\phi'')_j = \frac{-\phi_{j-2} + 16\phi_{j-1} - 30\phi_j + 16\phi_{j+1} - \phi_{j+2}}{12h^2} + \frac{1}{90}h^4\phi^{(VI)} \quad (5.1)$$

5.2.1 Upwind Schemes

The convective terms are discretized with a third-order accurate upwind scheme proposed by Rai and Moin (1991) which is similar to the third-order accurate scheme proposed by Kawamura and Kuwahara (1984). The two schemes can be represented by Eq.5.2 with $a = 12$ for the scheme by Rai and Moin (1991) and $a = 4$ for the scheme by Kawamura and Kuwahara (1984). The splitting of terms implies an interpretation of the scheme to be composed of a central part and an upwind part. The first bracket is the classic fourth-order central scheme to which an upwinding part, a hyper-viscous term, is

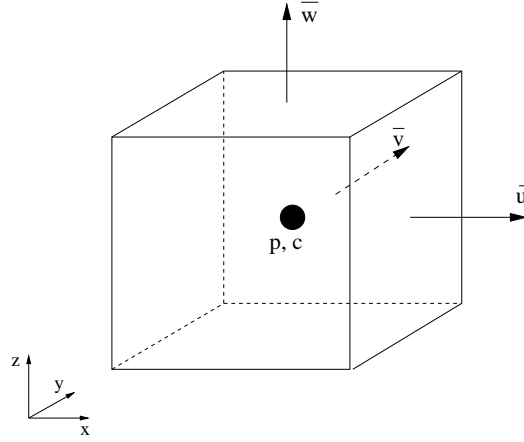


Figure 5.1: Computational cell in a 3D staggered grid

added. While the central part is fourth-order accurate, the hyper-viscous term is third-order accurate and accounts for the leading-order truncation error. The leading-order truncation error is therefore inversely proportional to the factor a .

$$\begin{aligned}
 (u\phi')_j &= \frac{u_j}{12h} (8(\phi_{j+1} - \phi_{j-1}) - (\phi_{j+2} - \phi_{j-2})) \\
 &+ \frac{|u_j|}{ah} ((6\phi_j - 4(\phi_{j+1} + \phi_{j-1}) + (\phi_{j+2} + \phi_{j-2}))) \\
 &+ \frac{|u_j|}{a} h^3 \phi^{(IV)}
 \end{aligned} \tag{5.2}$$

Thus, for the smooth components (for which the expansion above is valid) the scheme proposed by Kawamura and Kuwahara (1984) has a larger truncation error compared to that of the scheme of Rai and Moin (1991). This is further discussed in Sec.5.2.4.

5.2.2 Weighted Essentially Non-Oscillatory Schemes

Adaptive Stencil Methods

Adaptive stencil methods as Essentially Non-Oscillatory (ENO) schemes and Weighted Essentially Non-Oscillatory (WENO) schemes use the idea of computing the finite differences from several candidate stencils. Harten, Engquist, Osher, and Chakravarthy (1987) introduce ENO schemes. These choose the smoothest out of all candidate stencils to obtain a uniformly high

accuracy. Moreover, near discontinuities this choice prevents usage of stencils with discontinuous values and accounts for the essentially non-oscillatory property while the high accuracy is maintained. Shu and Osher (1988) develop the idea such that an ENO scheme with an accuracy of order r can be constructed from r candidate stencils.

WENO schemes use a weighted combination of all candidate stencils, following the idea of Liu, Osher, and Chan (1994). The smoothest stencil is assigned the largest weight whereas stencils with strong curvature or discontinuity are assigned near zero weight. In this adaptive combination of stencils lies the high efficiency of WENO schemes compared to ENO schemes: It seems unnecessary to choose between candidate stencils of an ENO scheme in regions where the solution is smooth, as all stencils contain equally valuable information. WENO schemes use all these stencils and assign them optimal weights such that a high accuracy is obtained in smooth regions. Near discontinuities WENO schemes effectively are as accurate as ENO schemes as near zero weights are assigned to all stencils bearing discontinuous values. By the method given in Liu et al. (1994) from ENO schemes of order r WENO schemes of order $r + 1$ can be constructed.

The present WENO scheme is constructed by Jiang and Shu (1996). Their computed weights approach the optimal linear weights with second-order accuracy such that from an ENO scheme of accuracy order r a WENO scheme of order $2r - 1$ is obtained. As the candidate stencils are third-order accurate, the present WENO scheme is fifth-order accurate in smooth regions while at discontinuities it approaches the parent ENO scheme of order three.

If the stencil is smooth, the weights assigned to the third-order fluxes are close to the optimal linear weights. In this case the scheme approaches the fifth-order upwind scheme in Eq.5.3.

$$\begin{aligned}
 (u\phi)'_j &= \frac{u_j}{60h} (45(\phi_{j+1} - \phi_{j-1}) - 9(\phi_{j+2} - \phi_{j-2}) + (\phi_{j+3} - \phi_{j-3})) \\
 &+ \frac{|u_j|}{60h} (20\phi_j - 15(\phi_{j+1} + \phi_{j-1}) + 6(\phi_{j+2} + \phi_{j-2}) - (\phi_{j+3} + \phi_{j-3})) \\
 &+ \frac{|u_j|}{60} h^5 \phi_j^{(VI)}
 \end{aligned} \tag{5.3}$$

Balsara and Shu (2000) extend this construction up to $r = 7$, resulting in WENO schemes of order up to thirteen. Shu (2001) reviews WENO schemes among other high-order methods, and shows the ability of the fifth-order WENO scheme to handle non-uniform, but smooth grids. Yang, Yang, Chen, and Hsu (1998) apply the present WENO scheme to Navier-Stokes equations for incompressible flow and simulate laminar flow through an elbow square

duct and a lid-driven cavity flow. They find the convergence of the WENO scheme to be much faster than of the corresponding ENO scheme.

Numerical Procedure

The partial derivatives at the location x_j are computed from the numerical fluxes $\hat{\phi}_{j+1/2}$ and $\hat{\phi}_{j-1/2}$ at half distances to the neighboring points.

$$(\phi')_j = \frac{1}{h}(\hat{\phi}_{j+1/2} - \hat{\phi}_{j-1/2}) \quad (5.4)$$

For $u_j \geq 0$ the numerical flux is computed from three third-order fluxes, each computed on a different stencil and assigned a different nonlinear weight w_i .

$$\hat{\phi}_{j+1/2} = w_1\hat{\phi}_{j+1/2}^{(1)} + w_2\hat{\phi}_{j+1/2}^{(2)} + w_3\hat{\phi}_{j+1/2}^{(3)} \quad (5.5)$$

The three third-order fluxes are given by

$$\begin{aligned} \hat{\phi}_{j+1/2}^{(1)} &= \frac{1}{3}\phi_{j-2} - \frac{7}{6}\phi_{j-1} + \frac{11}{6}\phi_j \\ \hat{\phi}_{j+1/2}^{(2)} &= -\frac{1}{6}\phi_{j-1} + \frac{5}{6}\phi_j + \frac{1}{3}\phi_{j+1} \\ \hat{\phi}_{j+1/2}^{(3)} &= \frac{1}{3}\phi_j + \frac{5}{6}\phi_{j+1} - \frac{1}{6}\phi_{j+2} \end{aligned} \quad (5.6)$$

The nonlinear weights are assigned according to the smoothness of the values. Whereas in smooth regions the weights are large, in regions of discontinuity or strong curvature nearly zero weights are assigned. The smoothness indicators β_k are computed for each candidate stencil.

$$\begin{aligned} \beta_1 &= \frac{13}{12}(\phi_{j-2} - 2\phi_{j-1} + \phi_j)^2 + \frac{1}{4}(\phi_{j-2} - 4\phi_{j-1} + 3\phi_j)^2 \\ \beta_2 &= \frac{13}{12}(\phi_{j-1} - 2\phi_j + \phi_{j+1})^2 + \frac{1}{4}(\phi_{j-1} - \phi_{j+1})^2 \\ \beta_3 &= \frac{13}{12}(\phi_j - 2\phi_{j+1} + \phi_{j+2})^2 + \frac{1}{4}(3\phi_j - 4\phi_{j+1} + \phi_{j+2})^2 \end{aligned} \quad (5.7)$$

The nonlinear weights are computed from the linear weights γ_k and the smoothness indicators. A small number ϵ is added to the denominator, here $\epsilon = 10^{-6}$, so as to avoid that the denominator can become zero,

$$w_i = \frac{\left(\frac{\gamma}{\epsilon + \beta}\right)_i}{\sum_{k=1}^3 \frac{\gamma_k}{(\epsilon + \beta_k)^2}} \quad (5.8)$$

The linear weights are

$$\begin{aligned}\gamma_1 &= \frac{1}{10} \\ \gamma_2 &= \frac{6}{10} \\ \gamma_3 &= \frac{3}{10}\end{aligned}\tag{5.9}$$

5.2.3 Compact and Optimized Schemes

The idea of compact schemes is to approximate the derivative not only from the values at neighboring points but also from the derivatives at neighboring points. Optimized schemes are schemes which do not have the highest possible order of accuracy for their given stencil but are optimized in wave number space for desired resolution properties. Lele (1992) defines a general class of schemes following this idea. Restricting the stencil of the left hand side to five and of the right hand side to seven, the first derivative of a central scheme is approximated by

$$\begin{aligned}& \beta_1\phi'_{j-2} + \alpha_1\phi'_{j-1} + \phi'_j + \alpha_1\phi'_{j+1} + \beta_1\phi'_{j+2} \\ &= c_1\frac{\phi_{j+3} - \phi_{j-3}}{6h} + b_1\frac{\phi_{j+2} - \phi_{j-2}}{4h} + a_1\frac{\phi_{j+1} - \phi_{j-1}}{2h}\end{aligned}\tag{5.10}$$

and the second derivative by

$$\begin{aligned}& \beta_2\phi''_{j-2} + \alpha_2\phi''_{j-1} + \phi''_j + \alpha_2\phi''_{j+1} + \beta_2\phi''_{j+2} \\ &= c_2\frac{\phi_{j+3} - 2\phi_j + \phi_{j-3}}{9h^2} + b_2\frac{\phi_{j+2} - 2\phi_j + \phi_{j-2}}{4h^2} \\ &+ a_2\frac{\phi_{j+1} - 2\phi_j + \phi_{j-1}}{h^2}\end{aligned}\tag{5.11}$$

The accuracy of these schemes can be estimated by Taylor expansions about ϕ_j and ϕ'_j . The result is shown for the first derivative

$$\begin{aligned}0 &= ((a + b + c) - (1 + 2\alpha + 2\beta))\phi'_j \\ &+ \left(\frac{1}{3!}(a + 2^2b + 3^2c) - \frac{2}{2!}(\alpha + 2^2\beta)\right)h^2\phi'''_j\end{aligned}$$

$$\begin{aligned}
& + \left(\frac{1}{5!}(a + 2^4b + 3^4c) - \frac{2}{4!}(\alpha + 2^4\beta) \right) h^4 \phi_j^{(V)} \\
& + \left(\frac{1}{7!}(a + 2^6b + 3^6c) - \frac{2}{6!}(\alpha + 2^6\beta) \right) h^6 \phi_j^{(VII)} \\
& + \left(\frac{1}{9!}(a + 2^8b + 3^8c) - \frac{2}{8!}(\alpha + 2^8\beta) \right) h^8 \phi_j^{(IX)} \\
& + \left(\frac{1}{11!}(a + 2^{10}b + 3^{10}c) - \frac{2}{10!}(\alpha + 2^{10}\beta) \right) h^{10} \phi_j^{(XI)} \quad (5.12)
\end{aligned}$$

From this expression, constraints on the coefficients can be imposed: As all derivatives are linearly independent, the leading-order truncation error is the lowest order term which is not identically zero. For example, if $a + b + c = 1 + 2\alpha + 2\beta$, the first bracket disappears, and the approximation is second-order accurate. If also $a + 2^2b + 3^2c = 2\frac{3!}{2!}(\alpha + 2^2\beta)$, the second bracket disappears, and the approximation is fourth-order accurate, and so on. The general class of schemes can be categorized in several ways: The degrees of freedom, the order of accuracy, the stencil, and the bandwidth. As there are five coefficients, a maximum of five constraints can be enforced, yielding a tenth-order accurate scheme. Dropping the last constraint gives one degree of freedom, and a one-parameter family of eighth-order schemes is obtained. Dropping the two last constraints gives a two-parameter family of sixth-order schemes. Constraints can successively be dropped until a four-parameter family of second-order schemes is obtained. The stencil is the number of grid points a scheme uses. If c is non-zero, the stencil is seven. If b or β are non-zero and c is zero, the stencil is five. If only a is non-zero, the stencil is three, and the classic second-order central scheme is obtained. Classic fourth- and sixth-order schemes can also be obtained. The stencil is an important parameter with respect to computation time, with respect to the ability of a scheme to be applied close to the boundary, and with respect to parallelization. The bandwidth refers to the number of derivatives used in the computation. If the approximation for the derivatives is written for all points, a system of equations is obtained which can be written in matrix form. If α and β are zero, the matrix has zeros everywhere except on the diagonal, the bandwidth is one. If α is non-zero and β is zero, three diagonals are non-zero, and the bandwidth is three. If all five derivatives are used, the bandwidth is five. The larger the bandwidth, the longer the computation time to solve the system. With these categorizations at hand, two additional categorizations can be defined. A scheme is called *compact* if derivatives of neighboring points are used in the approximation of the derivative. This means, the bandwidth of compact schemes is more than one, the stencil at least three. A scheme is called *optimized* if for its given stencil, not all constraints are enforced and the obtained degrees of freedom, one for a one-

parameter family of schemes, are used to optimize the resolution properties of the scheme.

Explicit Filtering

As the leading-order truncation error of central schemes is dispersive, the numerical solution of the Navier-Stokes equations is often difficult due to unresolved flow features. Spurious (high-frequency) waves can be amplified and render the numerical scheme unstable. Therefore, spurious waves have to be filtered out. The explicit digital filter applied in this thesis is sixth-order accurate for the smooth components. The filter is applied in all three directions in the accuracy estimation. In the channel flow case the digital filter is applied in both grid directions in which the grid is not stretched. Filtering in the direction of the grid stretching results in a commutation error and is therefore skipped (Gullbrand and Chow, 2003). The filter is written for two dimensions as:

$$\hat{\phi}_{i,j} = a_0\phi_{i,j} + \sum_{m=1}^3 a_m \frac{\phi_{i+m,j} + \phi_{i-m,j} + \phi_{i,j+m} + \phi_{i,j-m}}{4} \quad (5.13)$$

with the coefficients $a_0 = 0.6875$, $a_1 = 0.46875$, $a_2 = -0.1875$, and $a_3 = 0.03125$. The truncation error can be found by Taylor expansion.

$$\hat{\phi}_{i,j} = \phi_{i,j} + \frac{47}{6!2} h^6 \phi_{i,j}^{(VI)} \quad (5.14)$$

5.2.4 Comparison of the Schemes

Several measures are available to compare the efficiency of numerical schemes for LES. The formal accuracy is measured by the truncation error which is the difference between the PDEs and FDEs. The order of accuracy measures the order with which the error becomes smaller upon grid refinement. For infinitely fine grids, the error should be identically zero. However, the resolution is always finite. In LES, the small resolved scales contain significant amounts of energy. Therefore, resolution properties in the high frequency end of resolvable waves are another important factor for computational efficiency (Nagarajan, Lele, and Ferziger, 2003). The resolution properties of a scheme determine how many grid points are required to represent a flow feature. A third factor is the computational time which is determined by the operation count and efficient implementation.

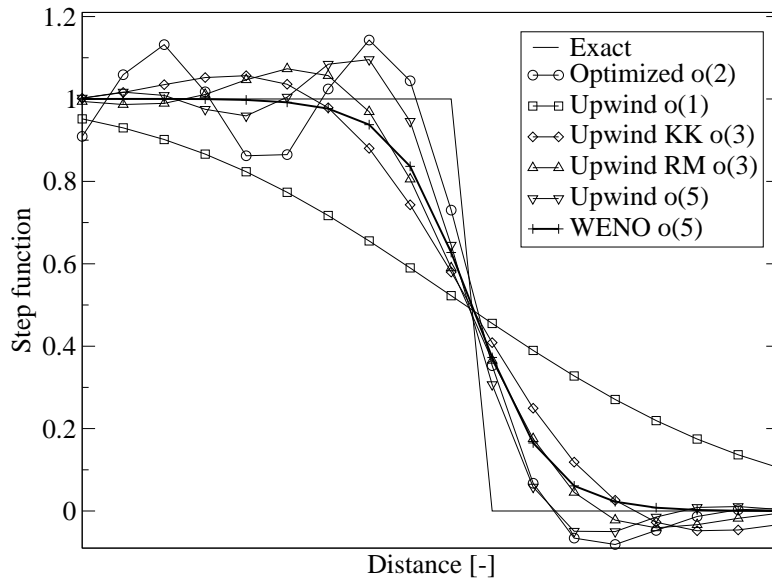


Figure 5.2: Propagation of a step

One-Dimensional Numerical Tests

As easy test and to elucidate the properties of different schemes, the propagation of a sine^2 wave and a jump are investigated using the first-order, linear wave equation. As a jump contains no length scale, any length scale which appears in the solution is purely numerical. The numerical length scale is proportional to the cell size, and grid refinement gives qualitatively the same result. Fig.5.2 shows the jump after 10000 time steps. The first-order upwind scheme smears out the jump over several cells due to excessive numerical diffusion. Classical high-order schemes approximate the jump with steeper gradients. The larger truncation error of the scheme by Kawamura and Kuwahara (1984) is reflected in the larger numerical length scale. Moreover, high-order methods have numerical wiggles preceding and following the jump. Whereas the third-order schemes dissipate these close to the jump, the optimized scheme shows propagation of the wiggles. This behavior is typical for central schemes as the leading order truncation error is dispersive. Apart from the first-order upwind scheme, only the WENO scheme has essentially no numerical wiggles, unlike its parent fifth-order upwind scheme. This property makes the WENO scheme suitable for the computation of jumps which are found in shocks or flame fronts.

Another example is the propagation of a sine^2 wave which is different from the jump as the sine^2 wave does contain the wave length as a length scale. As all schemes perform well if the resolution is high, a low resolution is

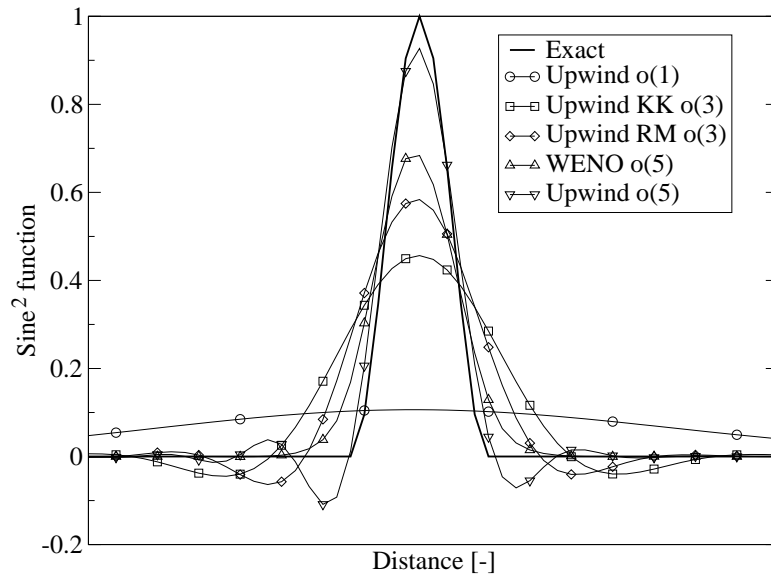


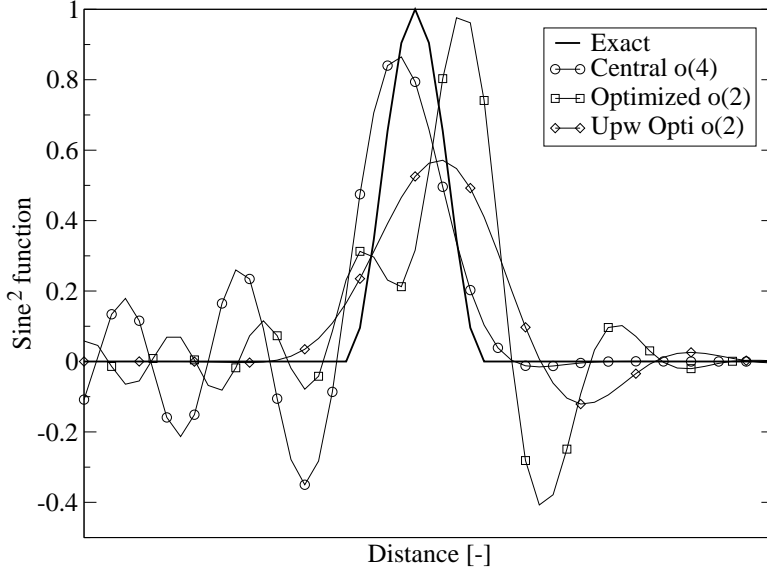
Figure 5.3: Propagation of a sine^2 wave with upwind schemes

selected: In Figs. 5.3 and 5.4 the wavelength is resolved with 12 cells. Fig. 5.3 shows the performance of upwind schemes. Numerical diffusion results in a decrease in amplitude of the wave. Whereas with a first-order upwind scheme the wave has nearly disappeared, the fifth-order upwind scheme still gives a reasonable representation of the sine^2 wave. At this resolution the non-linear weights of the WENO scheme are far away from the optimal weights, and the scheme is more diffusive than the fifth-order upwind scheme. One needs several hundred cells on the sine^2 wave to approach the fifth-order upwind scheme with the WENO scheme, but only several ten cells to obtain fifth-order accuracy as is discussed in Sec.5.2.4. Yet, the WENO scheme is considerably less diffusive than the third-order upwind methods. Fig. 5.4 shows the dispersion error of central schemes. The oscillations spread in the whole domain unless they are removed by a digital filter or diffused by upwinding as shown for the optimized scheme.

Fourier Analysis

The resolution properties of numerical schemes can be investigated by means of Fourier analysis. The function $\phi(x)$ is considered to be periodic over the domain $[0, L]$. Assuming the problem is *linear*, the principle of superposition is valid, and the function may be decomposed into Fourier modes.

$$\phi(x) = \sum \hat{\phi}_k e^{\frac{i2\pi kx}{L}} \quad (5.15)$$

Figure 5.4: Propagation of a sine^2 wave with central schemes

L is divided in N cells, so the grid spacing is $h = L/N$. It is convenient to define a scaled wavenumber ω and a scaled coordinate s .

$$\omega = 2\pi kh/L \quad (5.16)$$

$$s = x/h \quad (5.17)$$

The Fourier modes become $e^{i\omega s}$. Differentiating with respect to s yields

$$\hat{\phi}'_k = i\omega \hat{\phi}_k \quad (5.18)$$

On the other hand, the derivative can be computed using the finite difference scheme:

$$(\hat{\phi}'_k)_{fd} = i\omega' \hat{\phi}_k \quad (5.19)$$

The modified wavenumber w' is a complex number. The real part of w' (as defined here) is associated with a dispersive error. The dispersion error for the schemes is plotted in Fig.5.5. The first-order upwind and second-order central schemes have the same dispersion error, as well as the fourth-order central and the third-order upwind schemes by Rai and Moin (1991) and Kawamura and Kuwahara (1984). The superior resolution characteristics of the optimized scheme are evident in the later departure from the exact derivative line $w' = w$. The WENO scheme is only comparable to the third-order

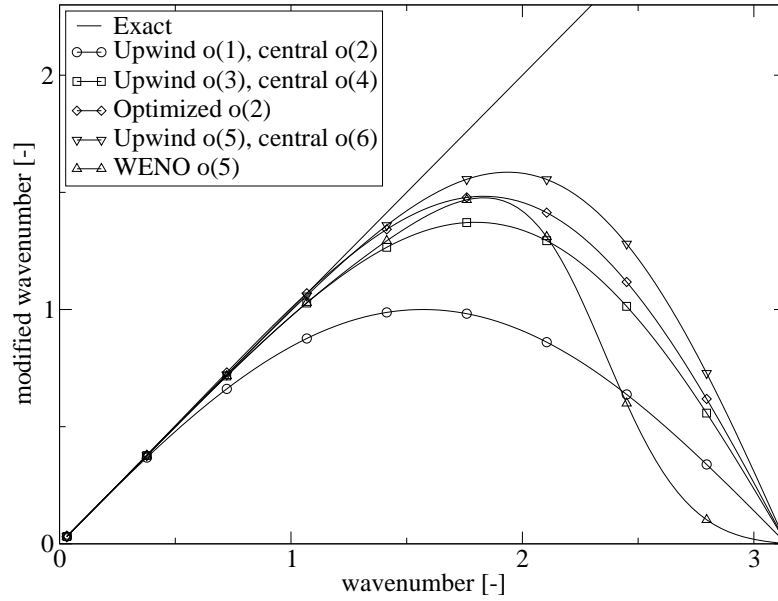


Figure 5.5: Dispersion error

schemes, but the departure from the exact derivative is delayed marginally. The parent fifth-order upwind has much better resolution characteristics in the high wavenumber range than the WENO scheme. This is expected as with this resolution the non-linear weights are far from optimal. The imaginary part of the modified wavenumber quantifies a dissipation error. Fig. 5.6 shows dissipation errors $e^{Imaginary(\omega')s}$ of upwind schemes and the low pass filter which is used to stabilize the optimized scheme. Central schemes have no dissipation error at all and are therefore not plotted. The first-order upwind scheme has large dissipation errors even for low wavenumbers and is therefore useless for LES. The third-order upwind scheme by Kawamura and Kuwahara (1984) has better dissipation characteristics and the drop of the dissipation curve is delayed to larger wavenumbers. This drop is delayed to even larger wavenumbers for the third-order upwind scheme by Rai and Moin (1991), the WENO scheme, and the fifth-order upwind scheme. The dissipation errors are also compared to the dissipation error of the low pass filter which is used to stabilize the optimized scheme.

Formal Accuracy

As numerical test a three-dimensional Gaussian function is suitable as it contains the width of the bell as length scale. The derivatives can be computed analytically and the solution can be compared with the solution com-

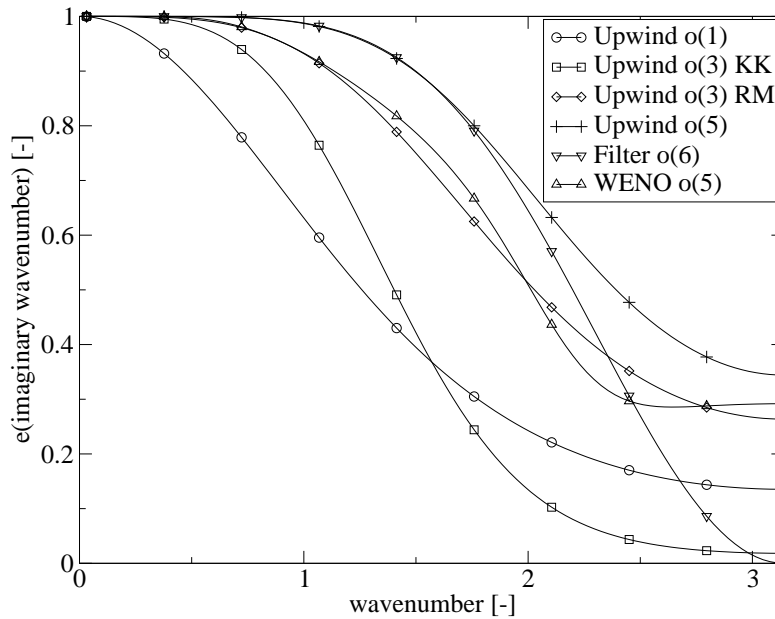


Figure 5.6: Dissipation error

puted with the discretization schemes. Fig.5.7 shows the error for high-order schemes for the momentum equations in L_2 -norm. The length scale used to normalize the abscissa is one standard deviation.

The fifth-order upwind scheme has the lowest error. The WENO scheme has the same formal accuracy, but a larger error. For very smooth stencils the curve of the WENO scheme approaches the fifth-order upwind scheme, and it fully mimics it if all stencils are assigned equal weight. In Fig.5.7 it appears that the WENO scheme has a higher accuracy than five. This has previously been celebrated as super-convergence of WENO schemes. However, Jiang and Shu (1996) point out that this super-convergence of WENO schemes in the medium wavenumber range is due to larger error than classic fifth-order schemes in the high wavenumber range. In the limit of very smooth stencil the parent scheme is recovered, and that is fifth-order accurate. The inferior resolution at high wavenumbers is also evident in the Fourier analysis.

High-order schemes converge faster to the real solution than low-order schemes upon grid refinement. However, the cell size is finite, and schemes with high formal accuracy do not necessarily have the lowest absolute error. If the length scale of the Gaussian bell is resolved with less than four cells, the optimized scheme has a lower truncation error than the other schemes. Such schemes are of interest if the wavenumbers of interest are not resolved well by the computational grid. In DNS such schemes may be advantageous as all

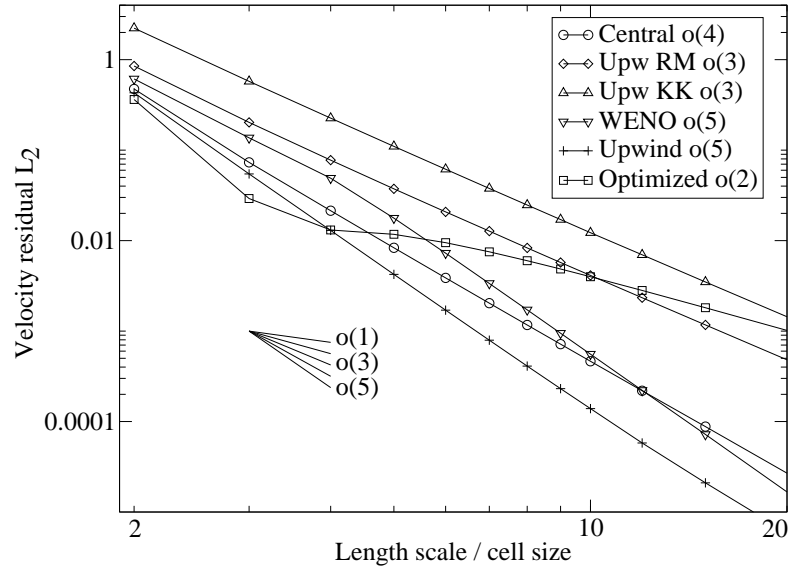


Figure 5.7: Comparison of accuracy for momentum equations for high-order schemes

length scales may be resolved with sufficiently small errors on comparatively coarse grids.

As the optimized scheme is a central scheme, spurious waves can render the scheme unstable and make stabilization necessary. Two options for stabilization are low-pass filtering and upwinding, as explained in Sec.5.2.3 and 5.2.1, respectively. Based on Fourier analysis the low-pass filter should have higher accuracy as is revealed in Fig.5.6 where the filter has lower dissipative error compared to upwinding, at least in linear analysis.

Fig.5.8 compares the accuracy of these options applied to the optimized scheme and the parent central scheme. The upwinded central scheme is the scheme by Rai and Moin (1991) (Upwind RM); its upwinded optimized analog (Opt Upw RM), the low-pass filter, and the central scheme with low-pass filter, and its optimized analog are also plotted. Out of the stabilized central and optimized schemes the best option with respect to resolution of high wavenumbers is to be found. In Fig.5.8 it becomes apparent that the upwinded optimized scheme, the analog to the scheme by Rai and Moin (1991), is of no use as it inherits the resolution of the scheme by Rai and Moin (1991) for high wavenumbers and the resolution of the optimized scheme for low wavenumbers: An upwinded optimized scheme is for all resolutions worse than any of the other schemes in the comparison. Also if the filter is applied to stabilize the scheme, the resolution of the low-pass filter for high wavenumbers will be inherited. However, here a length scale range in which

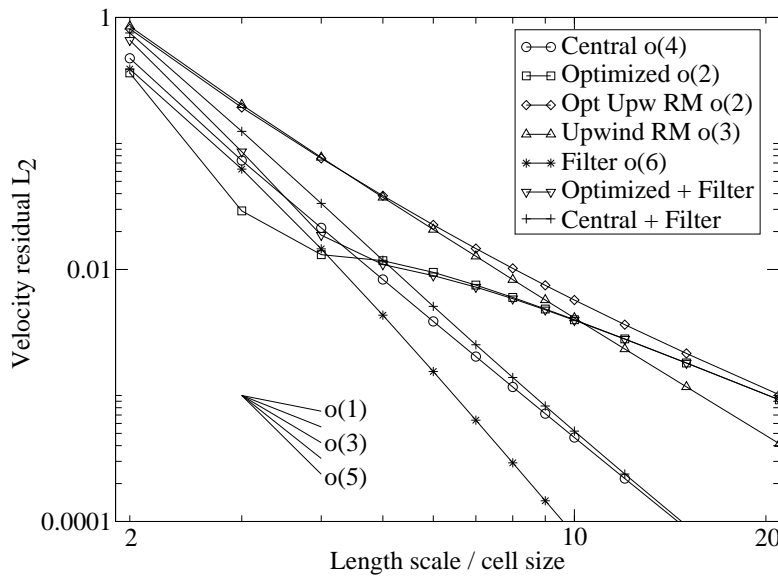


Figure 5.8: Comparison of accuracy for momentum equations for central schemes, upwinded central schemes, and central schemes with explicit filtering

the optimized scheme with low-pass filtering has better properties than the other options can be found: The cross-over of the curve with the curve for the central scheme with low-pass filtering is at five cells per length scale.

Computational Time and Efficiency

The computational time is a third important measure for the efficiency of a numerical scheme. It has been pointed out that the truncation error can be below any arbitrary value if only the grid is fine enough. However, the cost at which convergence is obtained may vary significantly. Normally, low-order schemes require more nodes than high-order schemes for the same truncation error. In Fig.5.7 a desired error level is represented by an imagined horizontal line. The abscissa of the intersection points between this imagined horizontal line and the accuracy curve of each scheme give the required number of nodes on a length scale which is to be resolved for each scheme.

In Fig.5.9 the average computer times per explicit time step are compared for identical grids. The optimized scheme is slightly faster than the upwind scheme, as the filtering is faster than the upwinding. The WENO scheme is slower by a factor of two. This result is obtained for a two-phase flow computation. The result changes with the number of parcels (~ 20000 in this case), as the time for the Lagrangian particle tracking depends on the number

10^6 Nodes	Upwind	Optimized	WENO
1.9	12.5	11.5	22.6
3.4	17.1	16.0	31.3
3.8	22.8	21.4	43.1

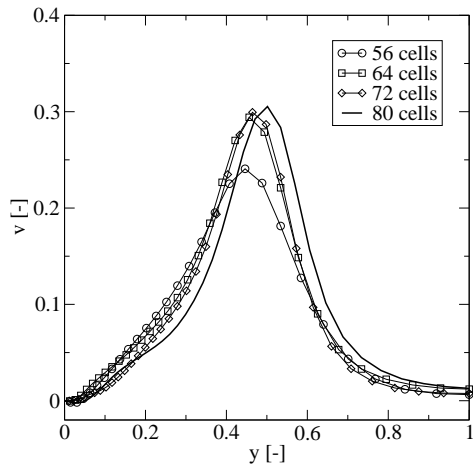
Figure 5.9: Required time per time step in seconds for various discretization schemes on three grids

of droplets, especially in the collision submodel. For a single-phase flow, the WENO scheme is about 3-4 times slower than the third-order upwind scheme. To illustrate how the efficiency can be judged from the provided data, a simple example is considered: A length scale is to be resolved with an error of less than 0.01. According to Fig.5.7, a WENO scheme requires 6 nodes on this length scale whereas the upwind scheme RM requires 8 nodes. For a three-dimensional problem that gives 216 versus 512 nodes. In the two-phase flow case the WENO requires twice as much time as the upwind scheme for the same grid. However, more than twice as many nodes are required, so in this comparison the WENO scheme is more efficient. This is certainly not to be understood as proof, but illustrates that the computational time should not be compared for the same grids but for the same error.

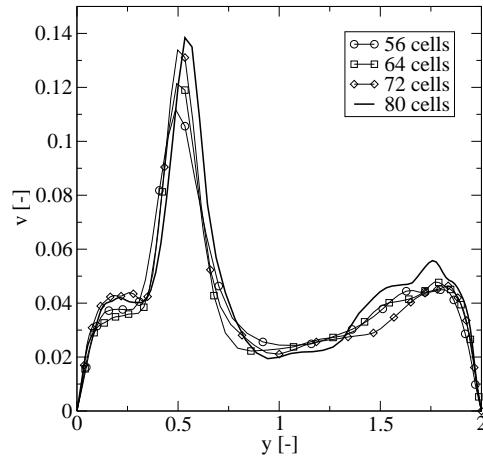
Grid Sensitivity

The grid sensitivity of the LES results can be estimated from solutions on a sequence of refined grids. The boundary conditions are described extensively in Sec.4.3. On the finest grid, the channel height is resolved with 80 cells. The grid is smoothly stretched in the wall normal direction to obtain a higher resolution near the wall. The resolution near the wall for the finest grid is $y^+ \sim 3$ while the cells in the x- and z-direction are coarser: $x^+ = z^+ \sim 10$.

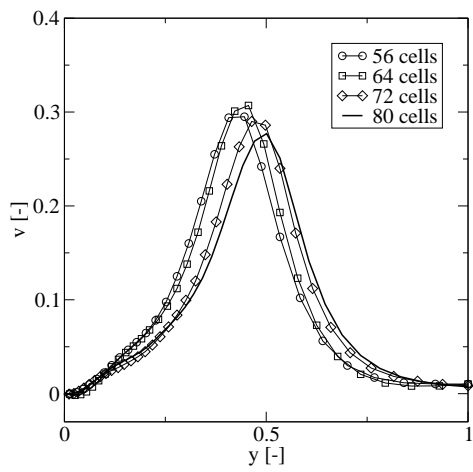
In Fig.5.10 the solutions on various grids for the average and rms of the velocity along the vertical centerline in the far-field (i.e. 100 diameters from the jet inlet) downstream are compared. Fig.5.10a shows the average vertical flow velocity profiles, and Fig.5.10b their rms, as computed with the fifth-order WENO scheme. The upwash between the two vortices of the CVP can be seen. The magnitude of the velocities indicates the strength of the CVP while the y-coordinate gives its penetration height. With the given momentum ratio, the maximum upwash occurs at $y \sim 0.5$. In Fig.5.10b the strong velocity fluctuations in the wake of the jet are apparent. These are due to the unsteady CVP and contribute to the good mixing properties of the JICF flow field. The rms profiles have peaks where the averages have large gradients (i.e. coinciding with the location for most production of



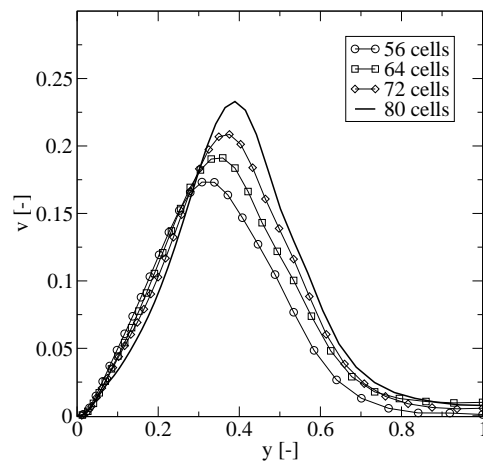
a) Average, WENO o(5)



b) RMS, WENO o(5)



c) Average, upwind o(3)



d) Average, optimized o(2)

Figure 5.10: Average and rms of vertical velocity profiles along vertical centerline 100 diameters downstream

turbulence). Fig.5.10 demonstrates that the solution is not very sensitive to the grid on the finer grids. There is a tendency to higher jet trajectories for finer grids, but the strength of the CVP and the wake are similar.

The same problem is computed using the third-order upwind scheme and the optimized scheme with the explicit digital filter. The average solutions are plotted in Fig.5.10c) and d), respectively. The calculations with the WENO and the upwind schemes have higher vortex curves. The maximum upwash is at $y \sim 0.5$ whereas for the optimized scheme it is at $y \sim 0.4$. The strength of the CVP is also weaker in the computation with the optimized scheme. It is likely that the explicit digital filter is responsible for the removal of turbulence. For this reason it is not studied further. One may consider filtering the flow field only every few time steps in the future. The WENO scheme does not seem to have advantages compared to the third-order upwind scheme by Rai and Moin (1991).

Handling of Jet Injection

Here an example for single-phase JICF is given which provides reasons why a WENO scheme is preferable for this application. The transverse jet emerges from the solid wall. The conditions are further described in Paper VI. The scalings of nozzle and channel differ by a factor of 20. Therefore the geometrical shape of the jet nozzle may include scales that are smaller than those supported by the current LES. The nozzle geometry itself is described in a local two-dimensional grid with a cell size 25 times smaller than the LES grid cell size ($h_{geometry}/h_{LES} = 1/25$). The velocity and scalar boundary conditions can then be specified regarding varying nozzle shape. The boundary conditions are simply filtered by applying Eq.2.61 to them. In this case a Gaussian filter kernel with a filter scale equal to a single cell on the LES grid is applied. Thus, the velocity boundary conditions have small-scale changes in gradients. Such small-scale changes pose numerical difficulties. Fig.5.11 a) and b) show the vertical and main (streamwise) velocity profiles along the prolongation of the nozzle axis, respectively. In Fig.5.11 the length of the potential core is estimated as about two to three diameters. The JICF bends away from the line, and the velocity drops sharply between three and four diameters. The solution computed with the third-order upwind scheme has a numerical wiggle: The wall-normal (vertical) velocity becomes negative close to the jet which is not supported by experiments. The WENO scheme handles this jet injection without wiggle.

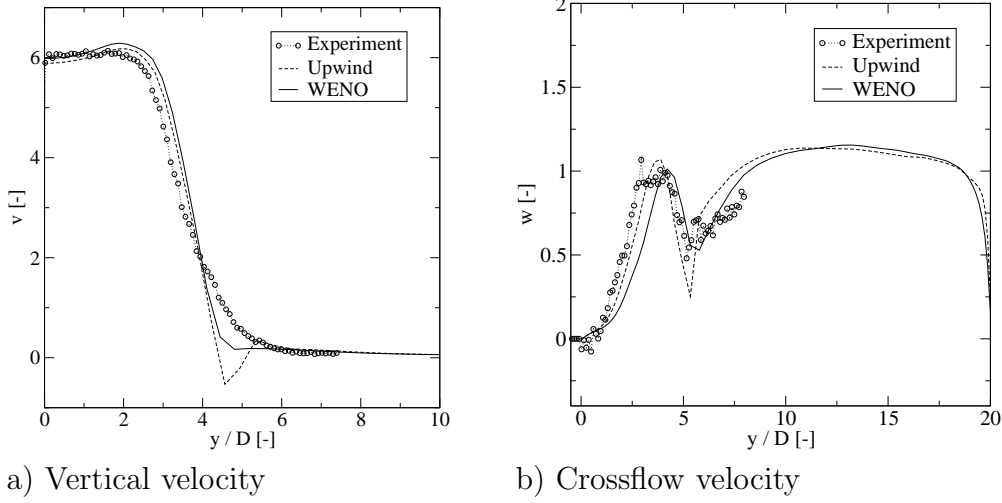


Figure 5.11: Profiles for vertical and streamwise velocities

5.2.5 Boundary Scheme

As the investigated high-order schemes require at least two grid points on each side of the node, a low-order scheme is used for the first cell next to the boundary. Second-order central schemes are used for the convective (5.20) terms as well as for the diffusive (5.21) terms. A first-order upwind scheme (5.22) is used if the Peclet number $Pe = \frac{uh}{\nu} > 1.8$.

$$(u\phi')_j = u_j \frac{\phi_{j+1} - \phi_{j-1}}{2h} - \frac{2}{3!} h^2 \phi''' \quad (5.20)$$

$$\phi_j'' = \frac{\phi_{j+1} - 2\phi_j + \phi_{j-1}}{h^2} - \frac{2}{4!} h^2 \phi^{(IV)} \quad (5.21)$$

$$(u\phi)_j = u_j \frac{\phi_{j+1} - \phi_{j-1}}{2h} + |u_j| \frac{2\phi_j - (\phi_{j-1} + \phi_{j+1})}{2h} \quad (5.22)$$

5.3 Flow Solver

The Navier-Stokes equations are integrated in time explicitly with a third-order accurate Runge-Kutta scheme. The spatial discretizations for the diffusive and convective terms are discussed in previous sections. Pressure corrections are obtained from a Poisson equation which is relaxed with a pointwise Gauss-Seidel iteration scheme.

The convergence is accelerated by using the multigrid method and the defect correction method. In the multigrid method one uses several grid levels

with varying cell size (half for each new grid level). This is advantageous as the rate with which an error decreases depends on the ratio of the wavelength of the error and the grid size, i.e. the scaled wavelength of the error: Errors with a short wavelength drop fast, and errors with long wavelength drop slowly on a given grid. Instead of fully converging the solution on the finest grid alone, the solution is restricted to the coarsest grid. Errors with long wavelength become errors with short wavelength on coarser grids, as not as many grid points are on the same wave. After convergence on the coarse grid the correction of the variables is prolonged to the next level. Such V-cycles are performed with increasingly finer grids until convergence on the finest grid is obtained.

In the defect correction method one computes the derivatives with a scheme of low order and a scheme of high order. The advantage is that it can be avoided to compute the derivatives with the high-order scheme implicitly and instead they are computed explicitly. One solves the equation:

$$L\phi = f \quad (5.23)$$

L is the Navier-Stokes differential operator, ϕ the solution, and f a source term. L_{lo} and L_{ho} are the corresponding low- and high-order finite difference operators, respectively. ϕ^n is the iterated solution at iteration n . One solves first:

$$L_{lo}\phi^{n+1} = f \quad (5.24)$$

and thereafter:

$$L_{lo}\phi^{n+1} = f + L_{lo}\phi^n - L_{ho}\phi^n \quad (5.25)$$

At convergence $L_{lo}\phi^{n+1} - L_{lo}\phi^n$ is smaller than any specified value and one has the solution ϕ^{n+1} which satisfies the equation:

$$L_{ho}\phi = f \quad (5.26)$$

The defect correction method is further discussed in Gullbrand, Bai, and Fuchs (2001).

Chapter 6

Summary of Publications

Paper I

The candidate computed the results and was the main author of the paper.

Mirko Salewski, Laszlo Fuchs. Model Consistency Issues of Lagrangian Particle Tracking Applied to a Spray Jet in Crossflow. Accepted for publication in Int. J. Multiphase Flow

Numerical simulations are performed for multiphase jets in crossflow. The flow solver uses an Eulerian/Lagrangian approach. Turbulence in the gas phase is modeled in the framework of large eddy simulation. The dispersed phase is handled using Lagrangian particle tracking. The model assumptions of solvers for Lagrangian particle tracking are critically assessed for typical flow conditions of spray jets in crossflow. The droplets are assumed to be spherical and isolated. In large regions the results are inconsistent with these model premises. Firstly, average Weber numbers can be so large that the model assumption to regard droplets as spherical is questionable, not only near the nozzle, but also in the far-field. Secondly, the average droplet spacing can be so low that droplets directly interact with each other, again also in the far-field. Thirdly, the average Stokes number in the jet region can be so large that the phase coupling between the dispersed and continuous phase is weak.

Paper II

The candidate computed the results and was the main author of the paper.

Mirko Salewski, Laszlo Fuchs. An Aerodynamic Droplet Interaction Model for Non-Dilute Sprays. Submitted to Int. J. Multiphase Flow

A novel model to account for aerodynamic interaction of monodisperse and polydisperse particles is proposed. The particle drag coefficients are corrected depending on relative positions of the particles. The particle interaction model is necessary to handle non-dilute two-phase flows in regimes in which particle interaction is not negligible, but not strong enough to bring the mixture to an equilibrium. The particle interaction is included within the Lagrangian particle tracking (LPT) framework. The approach is applied to simulate a dense spray jet in crossflow. It is shown that the average drag on the particles decreases by more than 40% in the dense spray region in the near-field of the jet due to the introduction of aerodynamic four-way coupling. The jet of monodisperse particles therefore penetrates farther into the crossflow if four-way coupling is accounted for. The aerodynamic particle interaction reduces turbulence levels. If particles are also allowed to break up, the aerodynamic particle interaction enhances turbulence levels, contrary to the results for monodisperse particles.

Paper III

The candidate computed the results and was the main author of the paper.

Mirko Salewski, Laszlo Fuchs. Dispersion of Circular, Non-Circular, and Swirling Spray Jets in Crossflow. In: Direct and Large Eddy Simulation VI (ERCOFTAC Series), E. Lamballais, R. Friedrich, B.J. Geurts, O. Metais (Eds.), Springer, 2006, ISBN 1-04020-4909-9

Multiphase jets in crossflow are investigated using large eddy simulation. The multiphase flow is handled in an Euler/Lagrange framework with two-way coupling. Atomization, droplet breakup, and droplet collision are modeled. The simulation is validated against experimental results found in the literature. The trajectory of the counter-rotating vortex pair (CVP) is shown to lie below the trajectory of the droplets. This leads to lateral dispersion of the droplets depending on the strength of the CVP. If the momentum flux ratio is large, the trajectories are steep, the CVP is strong, and the main droplet trajectory splits into two branches. The dispersion is compared for various nozzle geometries and swirling flow injection. Especially swirl is shown to have profound effects on the lateral and vertical dispersion of the spray.

Paper IV

The candidate computed the results and was the main author of the paper. The candidate was not involved in the experimental work.

Mirko Salewski, Dragan Stankovic, Laszlo Fuchs. Mixing of Circular and Non-Circular Jets in Crossflow, submitted to Flow, Turbulence, and Combustion

Coherent structures and mixing in the flow field of a jet in crossflow have been studied using computational (Large Eddy Simulation) and experimental (Particle Image Velocimetry and Laser-Induced Fluorescence) techniques. The mean scalar fields and turbulence statistics as determined by both are compared for circular, elliptic, and square nozzles. For the latter configurations, effects of orientation are considered. The computations reveal that the distribution of a passive scalar in a cross-sectional plane can be single- or double-peaked, depending on the nozzle shape and orientation. A proper orthogonal decomposition of the transverse velocity indicates that coherent structures may be responsible for this phenomenon. Nozzles which have a single-peaked distribution have stronger modes in transverse direction. The global mixing performance is superior for these nozzle types. This is the case for the blunt square nozzle and for the elliptic nozzle with high aspect ratio. It is further demonstrated that the flow field contains large regions in which a passive scalar is transported up the mean gradient (counter-gradient transport) which implies failure of the eddy viscosity hypothesis.

Paper V

The candidate computed the results and was the main author of the paper. The candidate was not involved in the experimental work.

Mirko Salewski, Dragan Stankovic, Laszlo Fuchs, Ephraim J. Gutmark. Coherent Structures in Circular and Non-Circular Jets in Crossflow. In: 44th Aerospace Science Meeting Proceedings, AIAA2006-0907, AIAA, 2006, ISBN 1-56347-807-2

Experimental and computational investigations are performed for jets in crossflow (JICF). Large eddy simulations (LES) are validated against the experimental results obtained by PIV. The nozzle is handled as a subgrid structure while an infinitely long channel is assumed in the computation, modeling the long water channel used for the PIV. It is demonstrated that the effect of nozzle shape on the flow can be computed with this approach.

The trajectories and turbulence statistics are compared for circular, square, rotated square with a corner in stream direction, and elliptic nozzles at high and low aspect ratios. The strength and lift-off of the counter-rotating vortices are explained by turbulence levels introduced by these nozzles. The sensitivity of the computed results to physical and numerical parameters is presented. The potential and limits of the present experimental and numerical techniques are discussed and compared.

Paper VI

The candidate computed the results and was the main author of the paper. The candidate was not involved in the experimental work.

Mirko Salewski, Dragan Stankovic, Laszlo Fuchs. A Comparison between a Single- and Multiphase Jet in Crossflow Using LES. J. Eng. Gas Turbines and Power, 129(1), 2007

Large eddy simulations are performed for a single- and a multiphase jet in crossflow (JICF). The multiphase JICF are compared to the single-phase case for the same momentum and mass flow ratios but various injection droplet sizes. Multiphase JICF have stronger CVPs than a corresponding single-phase JICF. Moreover, their trajectories are higher and their induced wakes weaker. The smaller the Stokes number of the droplets, the more the solution approaches the solution for single-phase flow. The computed results show the formation of a counter-rotating vortex pair (CVP) and horseshoe vortices which are convected downstream. LES reveals also the intermittent formation of upright wake vortices from the horseshoe vortices on the ground towards the CVP. The dispersion of polydisperse spray droplets is computed using the stochastic parcel method. Atomization and droplet breakup are modeled by a combination of the breakup model by Reitz and the Taylor analogy breakup model. Evaporation and droplet collision are modeled. The flow solver uses two-way coupling. Averages of the velocity and gaseous fuel mass fraction are computed. The single-phase JICF is validated against experimental data obtained by PIV. Additionally, the PDFs and frequency spectra are presented.

Chapter 7

Summary and Perspectives

Single- and multiphase JICF have been investigated. The contributions of this thesis are as follows:

- A novel model to allow for aerodynamic droplet interaction was developed. The effect of this indirect four-way coupling is significant for monodisperse spray. The average drag coefficient drops by as much as 50 % due to the presence of close-by droplets. This leads to higher trajectories and decreased turbulence levels.
- Several inconsistencies of Lagrangian particle tracking are revealed by plotting the spray variables in terms of Weber number, Stokes number, and the droplet spacing. These maps clearly demonstrate that several model premises of Lagrangian particle tracking are inadequate: The assumed sphericity of the droplet is inconsistent with the droplet distortion suggested by the computed Weber numbers. The assumed isolation of droplets is not consistent with the computed droplet spacing. The latter inconsistency spurred the development of the model for aerodynamic droplet interaction.
- The mixing performance of single-phase JICF is notably dependent on the nozzle geometry. Blunt square nozzles and elliptic low aspect ratio nozzles elevate turbulence levels and induce stronger lateral motion in the wake. This leads to better mixing performance. Additionally, the scalar distribution in a cross-sectional plane is demonstrated to change qualitatively alone due to nozzle shape effects: It can be single- or double-peaked. This claim should be tested by experiment. Additionally, it is shown that a passive scalar is transported up the mean gradient in wide regions.

- It is demonstrated that single- and multiphase JICF have strong similarities: One can find corresponding coherent structures, e.g. the counter-rotating vortices. The lower the Stokes number of the droplets, the more the flow field solution for multiphase flow approaches the solution for single-phase JICF.
- The methods are validated by computing sensitivities of the results to purely numerical parameters (grid, computational parcel size), to several modeling parameters (assumed injection size and velocity distribution, boundary conditions), and to the most important physical parameter, the momentum flux ratio. Comparison with experimental data shows satisfactory agreement.

The following suggestions are made for future work:

- Parameter sensitivity studies regarding the submodel for aerodynamic droplet interaction
 - Lift force effects due to other particles
 - Collision effects
 - Evaporation effects
 - Extend parameter ranges
- Extend spray modeling
 - Droplet deformation effects (Weber number)
 - Combustion
 - Multicomponent fuel

Bibliography

- A.A. Amsden, P.J. O'Rourke, and T.D. Butler. KIVA-II: A Computer Program for Chemically Reactive Flows with Sprays. Technical Report LA-11560-MS, Los Alamos National Laboratory, 1989.
- J. Andreopoulos. On the Structure of Jets in a Crossflow. *J. Fluid Mech.*, 157:163–197, 1985.
- J. Andreopoulos and W. Rodi. Experimental Investigation of Jets in a Crossflow. *J. Fluid Mech.*, 138:93–127, 1984.
- P.W. Atkins and L.L. Jones. *Chemical Principles, 3rd ed.* W.H. Freeman and Company, 2005.
- W. Bachalo, N. Chigier, and R. Reitz. *Spray Technology Short Course Lecture Notes*. N. Chigier, Carnegie Mellon University, 1997.
- D.S. Balsara and C.-W. Shu. Monotonicity Preserving Weighted Essentially Non-Oscillatory Schemes with Increasingly High Order of Accuracy. *J. Comp. Phys.*, 160:405–452, 2000.
- J. Bardina, J.H. Ferziger, and W.C. Reynolds. Improved Subgrid Scale Models for Large Eddy Simulation, AIAA-80-1357. In *13th Fluid and Plasma Dynamics Conference*. AIAA, 1980.
- G.K. Batchelor. *An Introduction to Fluid Dynamics*. Cambridge University Press, 1967.
- J. Becker and C. Hassa. Breakup and Atomization of a Kerosene Jet in Crossflow at Elevated Pressure. *Atomization and Sprays*, 11:49–67, 2002.
- C. Bergström. *Numerical Modeling of Fuel Sprays*. PhD thesis, Lund Institute of Technology, Lund, Sweden, 1999.

- G. Berkooz, P. Holmes, and J.L. Lumley. The Proper Orthogonal Decomposition in the Analysis of Turbulent Flows. *Ann. Rev. Fluid Mech.*, 25: 539–575, 1993.
- J.E. Broadwell and R.E. Breidenthal. Structure and Mixing of a Transverse Jet in Incompressible Flow. *J. Fluid Mech.*, 148:405–412, 1984.
- D. Caraeni, C. Bergström, and L. Fuchs. Modeling of Liquid Fuel Injection, Evaporation and Mixing in a Gas Turbine Burner Using Large Eddy Simulation. *Flow, Turbulence and Combustion*, 65:223–244, 2000.
- L. Cortelezzi and A.R. Karagozian. On the Formation of the Counter-Rotating Vortex Pair in Transverse Jets. *J. Fluid Mech.*, 446:347–373, 2001.
- C. Crowe, M. Sommerfeld, and Y. Tsuji. *Multiphase Flows with Droplets and Particles*. CRC Press, 1998.
- J.K. Dukowicz. A Particle-Fluid Numerical Model for Liquid Sprays. *J. Comp. Phys.*, 35:229–253, 1980.
- S. Elghobashi. On Predicting Particle-Laden Turbulent Flows. *Appl. Sci. Res.*, 52:309–329, 1994.
- R. Fearn and R.P. Weston. Vorticity Associated with a Jet in a Cross Flow. *AIAA J.*, 12(10):1666–1671, 1974.
- J.H. Ferziger and M. Peric. *Computational Methods for Fluid Dynamics*, 3rd ed. Springer, 2002.
- R.P. Feynman, R.B. Leighton, and M. Sands. *The Feynman Lectures on Physics*. Addison-Wesley Publishing Company, 1963.
- T.F. Fric and A. Roshko. Vortical Structure in the Wake of a Transverse Jet. *J. Fluid Mech.*, 279:1–47, 1994.
- L. Fuchs. An Exact SGS-Model for LES. In L. Gavrilakis, L. Machiels, and P.A. Monkewitz, editors, *Advances in Turbulence*, pages 23–26. Kluwer Academic Publishers, 1996.
- R.P. Fuller, P.-K. Wu, K.A. Kirkendall, and A.S. Nejad. Effects of Injection Angle on Atomization of Liquid Jets in Transverse Airflow. *AIAA J.*, 38 (1):64–72, 2000.

- M. Germano, U. Piomelli, P. Moin, and W.H. Cabot. A Dynamic Subgrid-Scale Eddy Viscosity Model. *Phys. Fluids A*, 3:1760–1765, 1991.
- S. Ghosal. An analysis of numerical errors in large-eddy simulations of turbulence. *J. Comp. Phys.*, 125:187–206, 1996.
- S. Ghosh and J.C.R. Hunt. Spray Jets in a Cross-Flow. *J. Fluid Mech.*, 365:109–136, 1998.
- I. Glassman. *Combustion, 3rd ed.* Academic Press, 1996.
- J. Gullbrand, X.-S. Bai, and L. Fuchs. High-Order Cartesian Grid Method for Calculation of Incompressible Turbulent Flows. *Int. J. Numerical Methods in Fluids*, 36:687–709, 2001.
- J. Gullbrand and F.K. Chow. The effect of Numerical Errors and Turbulence Models in Large-Eddy Simulations of a Channel Flow, with and without Explicit Filtering. *J. Fluid Mech.*, 495:323–341, 2003.
- E.J. Gutmark and F.F. Grinstein. Flow Control with Noncircular Jets. *Ann. Rev. Fluid Mech.*, 31:239–272, 1999.
- A. Harten, B. Engquist, S. Osher, and S.R. Chakravarthy. Uniformly High Order Accurate Essentially Non-Oscillatory Schemes, III. *J. Comp. Phys.*, 71:231–303, 1987.
- E.F. Hasselbrink and M.G. Mungal. Transverse Jets and Jet Flames. Part 1. Scaling Laws for Strong Transverse Jets. *J. Fluid Mech.*, 443:1–25, 2001a.
- E.F. Hasselbrink and M.G. Mungal. Transverse Jets and Jet Flames. Part 2. Velocity and OH Field Imaging. *J. Fluid Mech.*, 443:27–68, 2001b.
- B.A. Haven and M. Kurosaka. Kidney and Anti-Kidney Vortices in Crossflow Jets. *J. Fluid Mech.*, 352:27–64, 1997.
- J. Held and L. Fuchs. Large Eddy Simulation of Separated Transonic Flow Around a Wing Section. In *36th Aerospace Sciences Meeting and Exhibit, AIAA-98-0405*. AIAA, 1998.
- P. Holmes, J.L. Lumley, and B. Berkooz. *Turbulence, Coherent Structures, Dynamical Systems and Symmetry*. Cambridge University Press, 1996.
- I.M. Ibrahim and E.J. Gutmark. Dynamics of Single and Twin Circular Jets in Cross Flow, AIAA-2006-1281. In *44th AIAA Aerospace Science Meeting Proceedings*. AIAA, 2006. ISBN 1-56347-807-2.

- I.M. Ibrahim, S. Murugappan, and E.J. Gutmark. Penetration, Mixing and Turbulent Structures of Circular and Non-Circular Jets in Cross Flow, AIAA-2005-0300. In *43th AIAA Aerospace Science Meeting Proceedings*. AIAA, 2005. ISBN 1-56347-757-2.
- IEA. Key World Energy Statistics. Technical report, International Energy Agency, 2004.
- G.-S. Jiang and C.-W. Shu. Efficient Implementation of Weighted ENO Schemes. *J. Comp. Phys.*, 126:202–228, 1996.
- Y. Kamotani and I. Greber. Experiments on Confined Jets in Cross Flow. Technical Report CR-2392, NASA, 1974.
- T. Kawamura and K. Kuwahara. Computations of High Reynolds Number Flow Around a Circular Cylinder with Surface Roughness, AIAA-84-0340. In *AIAA 22nd Aerospace Sciences Meeting*. AIAA, 1984.
- R.M. Kelso, C. Delo, and A.J. Smits. Unsteady Wake Structures in Transverse Jets. In *Computational and Experimental Assessment of Jets in Cross Flow*. AGARD, 1993. ISBN CP-534.
- R.M. Kelso, T.T. Lim, and A.E. Perry. An Experimental Study of Round Jets in Cross-Flow. *J. Fluid Mech.*, 306:111–144, 1996.
- R.M. Kelso and A.J. Smits. Horseshoe Vortex Systems Resulting from the Interaction between a Laminar Boundary Layer and a Transverse Jet. *Phys. Fluids*, 7(1):153–158, 1995.
- A.G. Kravchenko and P. Moin. On the Effect of Numerical Errors in Large Eddy Simulations of Turbulent Flows. *J. Comp. Phys.*, 131:310–322, 1997.
- K.K.-Y. Kuo. *Principles of Combustion*. John Wiley & Sons, 1986.
- L.D. Landau and E.M. Lifshitz. *Fluid Mechanics, 2nd ed.* Elsevier Ltd., 1987.
- A.H. Lefebvre. The Role of Fuel-Preparation in Low-Emission Combustion. *J. Eng. for Gas Turbines and Power*, 117:617–654, 1995.
- S.K. Lele. Compact Finite Difference Schemes with Spectral-like Resolution. *J. Comp. Phys.*, 103:16–42, 1992.
- M.Y. Leong, V.G. McDonnell, and G.S. Samuelsen. Effect of Ambient Pressure on an Airblast Spray Injected into a Crossflow. *J. Propulsion and Power*, 17(5):1076–1084, 2001.

- S.P. Lin and R.D. Reitz. Drop and Spray Formation from a Liquid Jet. *Ann. Rev. Fluid Mech.*, 30:85–105, 1998.
- D.S. Liscinsky, B. True, and J.D. Holdeman. Crossflow Mixing of Noncircular Jets. *J. Propulsion and Power*, 12(2):225–230, 1996.
- X.D. Liu, S. Osher, and T. Chan. Weighted Essentially Non-Oscillatory Schemes. *J. Comp. Phys.*, 115:200–212, 1994.
- R.K. Madabhushi. A Model for Numerical Simulation of Breakup of a Liquid Jet in Crossflow. *Atomization and Sprays*, 13:413–424, 2003.
- R.J. Margason. Fifty Years of Jet in Cross Flow Research. In *Computational and Experimental Assessment of Jets in Cross Flow*. AGARD, 1993. ISBN CP-534.
- M.R. Maxey and J.J. Riley. Equation of Motion for a Small Rigid Sphere in Nonuniform Flow. *Phys. Fluids*, 26(4):883–889, 1983.
- S. Muppidi and K. Mahesh. Study of Trajectories of Jets in Crossflow Using Direct Numerical Simulations. *J. Fluid Mech.*, 530:81–100, 2005.
- S. Nagarajan, S.K. Lele, and J.H. Ferziger. A Robust High-Order Compact Method for Large Eddy Simulation. *J. Comp. Phys.*, 191:392–419, 2003.
- T.T. Nguyen and A.R. Karagozian. Liquid Fuel Jet in Subsonic Crossflow. *J. Propulsion and Power*, 8(1):21–29, 1992.
- M. Olsson and L. Fuchs. Large Eddy Simulation of the Proximal Region of a Spatially Developing Circular Jet. *Phys. Fluids*, 8(8):2125–2137, 1996.
- M. Olsson and L. Fuchs. Large eddy simulation of a forced semiconfined circular impinging jet. *Phys. Fluids*, 10(2):476–486, 1998.
- P.J. O'Rourke and A.A. Amsden. The TAB Method for Numerical Calculation of Spray Breakup. *SAE Technical Paper 872089*, 1987.
- R.L. Panton. *Incompressible Flow, 3rd ed.* John Wiley & Sons, Ltd., 2005.
- S.B. Pope. *Turbulent Flows*. Cambridge University Press, 2000.
- S.B. Pope. Ten Questions Concerning the Large-Eddy Simulation of Turbulent Flows. *New J. Phys.*, 6(35):1–24, 2004.
- K.R. Popper. *Logik der Forschung*. Julius Springer Verlag, 1934.

- M. Rachner, J. Becker, C. Hassa, and T. Doerr. Modelling of the Atomization of a Plain Liquid Fuel Jet in Crossflow at Gas Turbine Conditions. *Aerospace Science and Technology*, 6:495–506, 2002.
- M.M. Rai and P. Moin. Direct Simulations of Turbulent Flow Using Finite-Difference Schemes. *J. Comp. Phys.*, 96(1):15–53, 1991.
- R.D. Reitz and R. Diwakar. Effect of Drop Breakup on Fuel Sprays. *SAE Technical Paper 860469*, 1986.
- R.D. Reitz and R. Diwakar. Structure of High-Pressure Fuel Sprays. *SAE Technical Paper 870598*, 1987.
- P. Sagaut. *Large Eddy Simulation for Incompressible Flows*. Springer-Verlag, 1998. ISBN 3-540-67890-.
- M. Salewski and L. Fuchs. An Aerodynamic Droplet Interaction Model for Dense Sprays. *submitted to Int. J. Multiphase Flow*, 2006a.
- M. Salewski and L. Fuchs. Dispersion of Circular, Non-circular, and Swirling Spray Jets in Crossflow. In *Direct and Large-Eddy Simulation VI (ERCOFTAC Series)*, Lamballais, E., Friedrich, R., Geurts, B.J., Metais, O. (Eds.). Springer, 2006b. ISBN 1-04020-4909-9.
- M. Salewski and L. Fuchs. Model Consistency Issues of Lagrangian Particle Tracking Applied to a Spray Jet in Crossflow. *accepted for publication in Int. J. Multiphase Flow*, 2006c.
- M. Salewski, D. Stankovic, and L. Fuchs. Mixing in Circular and Non-Circular Jets in Crossflow. *submitted to Flow, Turbulence, and Combustion*, 2006a.
- M. Salewski, D. Stankovic, and L. Fuchs. A Comparison of A Single and Multiphase Jets in a Crossflow Using LES. *J. Eng. Gas Turbines and Power*, 129(1), 2007.
- M. Salewski, D. Stankovic, L. Fuchs, and E.J. Gutmark. Coherent Structures in Circular and Non-Circular Jets in Crossflow, AIAA-2006-0907. In *44th AIAA Aerospace Science Meeting Proceedings*. AIAA, 2006b. ISBN 1-56347-807-2.
- J.A. Schetz and A. Padhye. Penetration and Breakup of Liquids in Subsonic Airstreams. *AIAA J.*, 15(10):1385–1390, 1977.

- J.U. Schlüter and Schönfeld. LES of Jets in Cross Flow and its Application to a Gas Turbine Burner. *Flow, Turbulence and Combustion*, 65:177–203, 2000.
- C.-W. Shu. High Order Finite Difference and Finite Volume WENO Schemes and Discontinuous Galerkin Methods in CFD. Technical Report 2001-11, ICASE, 2001.
- C.-W. Shu and S. Osher. Efficient Implementation of Essentially Non-Oscillatory Shock-Capturing Schemes. *J. Comp. Phys.*, 77:439–471, 1988.
- W.A. Sirignano. *Fluid Dynamics and Transport of Droplets and Sprays*. Cambridge University Press, 1999.
- W.A. Sirignano and C. Mehring. Review of Theory of Distortion and Disintegration of Liquid Streams. *Progr. Energy and Combustion Science*, 26:609–655, 2000.
- L. Sirovich. Turbulence and the Dynamics of Coherent Structures Part I: Coherent Structures. *Quart. Appl. Math.*, XLV(3):561–571, 1987.
- J. Smagorinsky. General Circulation Experiments with the Primitive Equations. *Mon. Weather Rev.*, 91(3):99–152, 1963.
- S.H. Smith and M.G. Mungal. Mixing, Structure and Scaling of the Jet in Crossflow. *J. Fluid Mech.*, 357:83–122, 1998.
- M. Sommerfeld. Validation of a Stochastic Lagrangian Modelling Approach for Inter-Particle Collisions in Homogeneous Isotropic Turbulence. *Int. J. Multiphase Flow*, 27:1829–1858, 2001.
- L.K. Su and M.G. Mungal. Simultaneous Measurements of Scalar and Velocity Field Evolution in Turbulent Crossflowing Jets. *J. Fluid Mech.*, 513:1–45, 2004.
- R.I. Sykes, W.S. Lewellen, and S.F. Parker. On the Vorticity Dynamics of a Turbulent Jet in a Crossflow. *J. Fluid Mech.*, 168:393–413, 1986.
- F.X. Tanner. Development and Validation of a Cascade Atomization and Drop Breakup Model for High-Velocity Dense Sprays. *Atomization and Sprays*, 14:211–242, 2004.
- H. Tennekes and J.L. Lumley. *A First Course in Turbulence*. The MIT press, 1972.

- D.J. Torres, P.J. O'Rourke, and A.A. Amsden. A Discrete Multicomponent Fuel Model. *Atomization and Sprays*, 13:131–172, 2003a.
- D.J. Torres, P.J. O'Rourke, and A.A. Amsden. Efficient Multicomponent Fuel Algorithm. *Combust. Theory Modelling*, 7:67–86, 2003b.
- N. Toy, E. Savory, S. McCusker, and P.J. Disimile. The Interaction Region Associated with Twin Jets and a Normal Crossflow. In *Computational and Experimental Assessment of Jets in Cross Flow*. AGARD, 1993. ISBN CP-534.
- Q. Wang and K.D. Squires. Large Eddy Simulation of Particle Deposition in a Vertical Turbulent Channel Flow. *Int. J. Multiphase Flow*, 22(4): 667–683, 1996.
- D.C. Wilcox. *Turbulence Modeling for CFD*. DCW Industries, Inc., 1993. ISBN 0-9636051-0-0.
- P.-K. Wu, K.A. Kirkendall, R.P. Fuller, and A.S. Nejad. Breakup Processes of Liquid Jets in Subsonic Crossflows. *J. Propulsion and Power*, 13(1): 64–73, 1997.
- P.-K. Wu, K.A. Kirkendall, R.P. Fuller, and A.S. Nejad. Spray Structures of Liquid Jets Atomized in Subsonic Crossflows. *J. Propulsion and Power*, 14(2):173–182, 1998.
- J.-Y. Yang, S.-C. Yang, Y.-N. Chen, and C.-A. Hsu. Implicit Weighted ENO Schemes for the Three-Dimensional Incompressible Navier-Stokes Equations. *J. Comp. Phys.*, 146:464–487, 1998.
- F. Yeh and U. Lei. On the Motion of Small Particles in a Homogeneous Isotropic Flow. *Phys. Fluids*, 3(11):2571–2586, 1981.
- L.L. Yuan and R.L. Street. Trajectory and Entrainment of a Round Jet in Crossflow. *Phys. Fluids*, 10(9):2323–2335, 1998.
- L.L. Yuan, R.L. Street, and J.H. Ferziger. Large-Eddy Simulation of a Round jet in Crossflow. *J. Fluid Mech.*, 379:71–104, 1999.